TURBULENT WAKES IN A STRATIFIED FLUID. PART I: MODEL DEVELOPMENT, VERIFICATION, AND SENSITIVITY TO INITIAL CONDITIONS

M. Stephen Lewellen, et al

Aeronautical Research Associates of Princeton, Incorporated

Prepared for:

Office of Naval Research
Defense Advanced Research Projects Agency

August 1974

Sponsored by
Defense Advanced Research Projects Agency
DARPA Order No. 1910

A.R.A.P. REPORT NO 226

TURBULENT WAKES IN A STRATIFIED FLUID
PART I: MODEL DEVELOPMENT, VERIFICATION, AND SENSITIVITY TO INITIAL CONDITIONS

by

W. S. Lewellen, M. Teske and Coleman duP. Donaldson

Program Code No.	438
Dates of Contract	15 May 1972 - 30 June 1974
Amount of Contract	$176,000.00
Principal Investigators	Coleman duP. Donaldson W. S. Lewellen
Scientific Officer	Director, Fluid Dynamics Programs Mathematics and Information Sciences Division Office of Naval Research

This work was supported by the Defense Advanced Research Projects Agency of the Department of Defense and was monitored by the Office of Naval Research under Contract N00014-72-C-0413

Aeronautical Research Associates of Princeton, Inc.
50 Washington Road, Princeton, New Jersey 08540
609-452-2950

August 1974

SUMMARY

A computational model has been developed for the turbulent wake left by a body moving through a stably stratified medium. Details of the wake growth, collapse and generation of internal waves were examined by the application of a second-order closure approach to turbulent flow developed at A.R.A.P. over the past few years. Predictions of the model have been verified by comparison with a wide variety of wake flows including wakes with no momentum, wakes with axial momentum, wakes with angular momentum, and for wakes in both stratified and unstratified fluids.

The influence of ambient density gradient, initial density perturbation, axial momentum, propeller-induced swirl, and vertical lift forces are all investigated. A number of model runs demonstrate that the primary variable affecting the strength of the generated internal waves is the initial Richardson number, with the first local maximum of the vertical height of the wake scaling inversely with the 1/8th power of the initial Richardson number. The decay rate of the turbulence intensity as a function of distance normalized with respect to the body diameter appears less sensitive to the Froude number than it is to momentum.

Part II of this report reviews the numerical procedures involved in the actual computational scheme, and includes a complete listing of the WAKE program, plus a summary of its operation.

TABLE OF CONTENTS

NOMENCLATURE

a,A,b,c	model constants
C_D	drag coefficient of generating body
c_P	porosity coefficient in eq. (2.35)
D	diameter of generating body
f	QE isotropic correction factor
F	Nonzero forcing function of the Poisson eq. (2.12) for π
Fr	wake Froude number = $U/r_i N$
g	gravitational acceleration
N	Brunt-Väisälä frequency = $[-(g/\rho_o)\,\partial\rho_o/\partial z]^{\frac{1}{2}}$
p	pressure
Pr	Prandtl number = k/ν
q	square root of twice the turbulent kinetic energy normalized by U
r	wake radius
r_i	initial wake radius
r^*	radius at which q^2 has dropped to one-fourth its maximum value
$r_{\frac{1}{2}}$	radius at which u has dropped to one-half its maximum value
Re	Reynolds number = Ur_i/ν
Ri	Richardson number of turbulence = $r_i^2 N^2 q_{max}^2$
s_P	distance at which the porous liner first affects solution
s	model constant

s_1, s_2, s_3, s_4	constants of the scale eq. (2.21)
t	time
u	velocity departure in free stream direction normalized by U
u_i, u_j, u_k	Cartesian velocity components
U	free stream uniform velocity
v	horizontal velocity normalized by U
v_c	model constant
w	vertical velocity normalized by U
w_D	streaming velocity defect at the centerline
x_1, x_j, x_k	Cartesian coordinates
x	cocrdinate in free stream direction
y, z	coordinate in horizontal, vertical direction normalized by initial wake radius
δ_{ij}	Dirac delta function
κ	coefficient of laminar diffusion for density perturbation
λ	microscale of turbulent dissipation = $\Lambda/(a + bq\Lambda/\nu)^{\frac{1}{2}}$
Λ	macroscale of turbulent model
Λ_y, Λ_z	macroscale in the y, z directions
ν	kinematic viscosity
π	perturbation pressure = $[p + \int g\rho_o dz]/\rho_o U^2$
$\rho, \tilde{\rho}$	density, normalized density
$\hat{\rho}$	normalized perturbation density = $(\rho-\rho_o)/(r_1 \partial\rho_o/\partial z)$
ρ_o	ambient fluid density

ψ	stream function $= \int v\,dz = -\int w\,dy$
superscripts	
$\overline{\quad}$	denotes time average
'	denotes fluctuation about the mean value
subscript	
max	denotes maximum value
i,o	denotes initial conditions
$\frac{D(\ )}{Dt}$	convective derivative for steady flows $= U\frac{\partial(\ )}{\partial x} + u\frac{\partial(\ )}{\partial x} + v\frac{\partial(\ )}{\partial y} + w\frac{\partial(\ )}{\partial z}$

1. INTRODUCTION

The passage of a body through a density stratified medium creates a fluid dynamical problem of great complexity. The body motion generates a turbulent wake which is capable of transforming turbulent kinetic energy to potential energy by interacting with its surrounding density environment. The potential energy is in turn eventually transformed into internal gravity waves which may radiate away from the immediate surroundings. The numerical simulation of this wake collapse is of special concern in this final report.

Other investigators have studied the collapsing wake from experiments (ref. 1-3) and simple theoretical models (refs. 4-11). The approach at A.R.A.P. has been to work with the full equations of motion for an incompressible Boussinesq fluid and apply the technique of invariant second-order-closure (ref. 12) to the dynamic turbulence equations. This approach simulates the turbulent wake by three mean velocities, a perturbation density, perturbation pressure, and ten turbulence correlations.

Since the full scope of the problem is admittedly immense, we have chosen to move slowly into the full solution for the fifteen unknowns. Our first work involved verification of the invariant technique for turbulent flow in a density stratified medium by applying it to the constant shear stress sublayer in the atmosphere (ref. 13). This work was followed by a numerical simulation of the axisymmetric flow of a jet, the momentumless wake of Naudascher, and the wake of Chevray containing significant mean momentum in the streaming direction (ref. 14). We then began the development of a three-dimensional steady flow computer program that would enable us to simulate nonaxisymmetric flows. First results from that program in application to flow regimes restricted to the presence of either a perturbation in

streaming velocity or the cross-plane velocities (but not both) were reported soon afterward (ref. 15). This report details the final restructuring of the computer program to handle all three momentum equations simultaneously, and discusses the application of the full equation set to laboratory data and initial condition variability. In Section 2 we review the governing equations, analyze the treatment of a dynamic scale equation, and discuss the numerical techniques employed in the solution of the derived equations. In Section 3 we make comparisons of laboratory observations for both stratified and unstratified wakes with A.R.A.P. numerical simulations. In Section 4 we study the sensitivity of various flow parameters to changes in initial conditions.

2. FORMULATION OF THE MODEL

2.a Governing Equations

For an incompressible Boussinesq fluid in the presence of turbulence, all flow parameters may be written as the sum of mean and fluctuating parts. The time-averaged equations of motion become

$$\frac{\partial u_i}{\partial x_i} = 0 \tag{2.1}$$

$$\frac{Du_i}{Dt} = -\frac{1}{\rho_o}\frac{\partial p}{\partial x_i} - \frac{\partial \overline{u_i' u_j'}}{\partial x_j} + \frac{\partial}{\partial x_j}\left(\nu \frac{\partial u_i}{\partial x_j}\right) - \frac{g_i \rho}{\rho_o} \tag{2.2}$$

When the background ambient density gradient is constant*, the diffusion equation for the perturbation density $\rho^* = \rho - \rho_o$ becomes

$$\frac{D\rho^*}{Dt} = -\frac{\partial \overline{u_j' \rho'}}{\partial x_j} + \frac{\partial}{\partial x_j}\left(\kappa \frac{\partial \rho^*}{\partial x_j}\right) - u_i \frac{\partial \rho_o}{\partial x_i} \tag{2.3}$$

Subtracting the mean motions, using eqs. (2.1)-(2.3), from the full differential equations, we may then derive exact equations for the Reynolds stress correlation $\overline{u_i' u_j'}$ and the correlations involving the density fluctuation ρ'. These become

$$\frac{D\overline{u_i' u_j'}}{Dt} = -\overline{u_i' u_k'}\frac{\partial u_j}{\partial x_k} - \overline{u_j' u_k'}\frac{\partial u_i}{\partial x_k} - \frac{g_i}{\rho_o}\overline{u_j' \rho'} - \frac{g_j \overline{u_i' \rho'}}{\rho_o} - \frac{\partial}{\partial x_k}\left(\overline{u_i' u_j' u_k'}\right)$$

$$- \frac{1}{\rho_o}\left(\frac{\partial \overline{p' u_j'}}{\partial x_i} + \frac{\partial \overline{p' u_i'}}{\partial x_j}\right) + \overline{\frac{p'}{\rho_o}\left(\frac{\partial u_i'}{\partial x_j} + \frac{\partial u_j'}{\partial x_i}\right)} + \nu \frac{\partial^2 \overline{u_i' u_j'}}{\partial x_k^2}$$

$$- 2\nu \overline{\frac{\partial u_i'}{\partial x_k}\frac{\partial u_j'}{\partial x_k}} \tag{2.4}$$

*To use Eq. (2.3) for a variable ambient density gradient it would be necessary to assume that $\partial/\partial x_i \ll \partial \rho_o/\partial x_i$ were negligible.

$$\frac{D\overline{u_i'\rho'}}{Dt} = -\overline{u_i'u_j'}\frac{\partial\rho}{\partial x_j} - \overline{u_j'\rho'}\frac{\partial u_i}{\partial x_j} - \frac{g_i}{\rho_o}\overline{\rho'^2} - \frac{\partial}{\partial x_j}(\overline{u_i'u_j'\rho'}) - \frac{1}{\rho_o}\frac{\partial}{\partial x_i}(\overline{p'\rho'})$$
$$+ \overline{\frac{p'}{\rho_o}\frac{\partial\rho'}{\partial x_i}} - \nu\overline{\rho'\frac{\partial^2 u_i'}{\partial x_j^2}} - \kappa\overline{u_i'\frac{\partial^2\rho'}{\partial x_j^2}} \qquad (2.5)$$

$$\frac{D\overline{\rho'^2}}{Dt} = -2\overline{u_j'\rho'}\frac{\partial\rho}{\partial x_j} - \frac{\partial}{\partial x_j}\overline{u_j'\rho'^2} - 2\kappa\overline{\frac{\partial\rho'}{\partial x_k}\frac{\partial\rho'}{\partial x_k}} + \kappa\frac{\partial^2\overline{\rho'^2}}{\partial x_j^2} \qquad (2.6)$$

The closure of eqs. (2.1)-(2.5) is obtained by deriving (or assuming) relationships between the unknown third-order correlations and the second-order correlations and mean flow gradients. The procedure involved and the models currently used are discussed in greater detail in refs. 12 through 15. At this juncture it is sufficient to present the modeled equations and the mean flow equations in normalized form. Hereafter, lengths are normalized by the initial wake radius r_i, velocities by the free stream velocity U in the marching direction x; and perturbation density by $-r_i\partial\rho_o/\partial z$. In this way we arrive at three nondimensional parameters: Reynolds number, $Re = Ur_i/\nu$; Froude number, $Fr = [(-gr_i^2\,\partial\rho_o/\partial z)/\rho_o U^2]^{-1/2}$; and Prandtl number, $Pr = \kappa/\nu$. The pressure occurring in eq. (2.2) is replaced by a normalized perturbation pressure $\pi = [p + \int g\rho_o dz]/\rho_o U^2$. By assuming that velocities in the wake are close to the free stream velocity; and neglecting terms of order $(w_D/U)^2$, the continuity equation reduces to the two-dimensional, cross-plane continuity equation. This may be used in combination with the divergence of the cross-plane momentum equations to generate a Poisson equation for the perturbation pressure. In eq. (2.4) we may set $i = j$ and perform the summation to obtain the turbulent energy $q^2 = \overline{u'u'} + \overline{v'v'} + \overline{w'w'}$. The principal equations then become, with $\nabla^2 = \partial^2/\partial y^2 + \partial^2/\partial z^2$:

$$\frac{Dq^2}{Dt} = -\frac{2}{Fr^2}\overline{w'\rho'} - \frac{2q^3}{Re\lambda^2} + \frac{\partial}{\partial y}\left[\left(\nu_c q\Lambda + \frac{1}{Re}\right)\frac{\partial q^2}{\partial y}\right]$$

$$+ \frac{\partial}{\partial z}\left[\left(\nu_c q\Lambda + \frac{1}{Re}\right)\frac{\partial q^2}{\partial z}\right] - 2\,\overline{u_i'u_k'}\,\frac{\partial u_i}{\partial x_k} \qquad (2.7)$$

$$\frac{D\hat{\rho}}{Dt} = \frac{Pr}{Re}\nabla^2\hat{\rho} - \frac{\partial\overline{v'\rho'}}{\partial y} - \frac{\partial\overline{w'\rho'}}{\partial z} + w \qquad (2.8)$$

$$\frac{Du}{Dt} = \frac{1}{Re}\nabla^2 u - \frac{\partial\overline{u'v'}}{\partial y} - \frac{\partial\overline{u'w'}}{\partial z} \qquad (2.9)$$

$$\frac{Dv}{Dt} = -\frac{\partial\pi}{\partial y} + \frac{1}{Re}\nabla^2 v - \frac{\partial\overline{v'v'}}{\partial y} - \frac{\partial\overline{v'w'}}{\partial z} \qquad (2.10)$$

$$\frac{Dw}{Dt} = -\frac{\partial\pi}{\partial z} + \frac{1}{Re}\nabla^2 w - \frac{\partial\overline{v'w'}}{\partial y} - \frac{\partial\overline{w'w'}}{\partial z} - \frac{1}{Fr^2}\hat{\rho} \qquad (2.11)$$

$$\nabla^2\pi = F = -\frac{1}{Fr^2}\frac{\partial\hat{\rho}}{\partial z} - \frac{\partial^2\overline{v'v'}}{\partial y^2} - 2\,\frac{\partial^2\overline{v'w'}}{\partial y\,\partial z} - \frac{\partial^2\overline{w'w'}}{\partial z^2}$$

$$+ 2\,\frac{\partial v}{\partial y}\frac{\partial w}{\partial z} - 2\,\frac{\partial v}{\partial z}\frac{\partial w}{\partial y} \qquad (2.12)$$

The modeled form of the complementary Reynolds stress equations become

$$\frac{D\overline{u_i'u_j'}}{Dt} = -\overline{u_i'u_k'}\,\frac{\partial u_j}{\partial x_k} - \overline{u_j'u_k'}\,\frac{\partial u_i}{\partial x_k} - \frac{\delta_{3i}}{Fr^2}\overline{u_j'\rho'} - \frac{\delta_{3j}}{Fr^2}\overline{u_i'\rho'}$$

$$+ \frac{\partial}{\partial x_k}\left[\left(\nu_c q\Lambda + \frac{1}{Re}\right)\frac{\partial\overline{u_i'u_j'}}{\partial x_k}\right] - \frac{q}{\Lambda}\left(\overline{u_i'u_j'} - \frac{\delta_{ij}}{3}q^2\right)$$

$$- \frac{2\overline{u_i'u_j'}}{Re\lambda^2} \qquad (2.13)$$

$$\frac{D\overline{u_i'\rho'}}{Dt} = -\overline{u_i'u_j'}\frac{\partial\tilde{\rho}}{\partial x_j} - \overline{u_j'\rho'}\frac{\partial u_i}{\partial x_j} - \frac{\delta_{3i}}{Fr^2}\overline{\rho'^2} + \frac{\partial}{\partial x_j}\left[(v_c q\Lambda + \frac{Pr}{Re})\frac{\partial\overline{u_i'\rho'}}{\partial x_j}\right]$$

$$- \frac{Aq}{\Lambda}\overline{u_i'\rho'} - \frac{2\overline{u_i'\rho'}}{Re\lambda^2} \qquad (2.14)$$

$$\frac{D\overline{\rho'^2}}{Dt} = -2\overline{u_j'\rho'}\frac{\partial\tilde{\rho}}{\partial x_j} + \frac{\partial}{\partial x_j}\left[(v_c q\Lambda + \frac{Pr}{Re})\frac{\partial\overline{\rho'^2}}{\partial x_j}\right] - \frac{2s\overline{\rho'^2}}{Re\lambda^2} \qquad (2.15)$$

The microscale λ in eqs. (2.7), (2.13), (2.14) and (2.15) is related to the macroscale Λ through the expression

$$\lambda^2 = \Lambda^2/(a + bq\Lambda/v)$$

The turbulence parameters a, A, b, s, and v_c as determined in refs. 13 and 14 have values of 2.5, 0.75, 0.125, 1.8 and 0.3 respectively. Before discussing the approximations needed to solve eqs. (2.7)-(2.15) numerically on A.R.A.P.'s computer system, we first turn to a discussion of the determination of the scale length Λ.

2.b Treatment of the Turbulent Macroscale

In all the modeling work that A.R.A.P. had done up to 1974, we assumed that the behavior of the macroscale Λ depended only upon the gross features of the particular problem being addressed. As the flow regime shifted (say, from axisymmetric flow to flat plate boundary layer flow), the rules governing the determination of Λ changed, but a consistent pattern of requiring that Λ be proportional to the spread of the mean velocity or turbulent distribution q^2 was maintained. For the axisymmetric flow configurations, a good estimate for Λ was obtained by setting

$$\Lambda = cr^* \qquad (2.16)$$

where r^* defines the distance from the center $r = 0$ of the flow to the radius where q^2 has dropped to a quarter of its maximum value. The constant c has a value of 0.2 (ref. 14). Thus Λ is set equal to the constant value given by eq. (2.16) across the entire flow width.

Our analysis of the Monin-Obukhov sublayer (ref. 13) indicates that in a stratified fluid, the local scale - while being governed overall by eq. (2.16) - is also restricted in its maximum value by the critical Richardson number Ri^* of the flow, so that

$$\Lambda \leq \left(\frac{Ri^* \, q^2}{-\frac{g}{\rho_o} \frac{\partial \rho}{\partial z}} \right)^{1/2}, \quad \frac{\partial \rho}{\partial z} < 0 \qquad (2.17)$$

where q^2 and ρ are found locally. Equation (2.17) then limits the value of Λ in a region of stable stratification; the current value of $Ri^* = 0.25$.

For two-dimensional cross-plane motion in the y and z directions within a stratified turbulent wake, it seems logical to examine the q^2 decay in both directions and apply eq. (2.16) to determine Λ_y and Λ_z. Since the wake collapses in an elliptic-like behavior, we have chosen to write the Λ appearing in the equation for λ and the isotropy terms in the turbulence equations as

$$\Lambda = \frac{2\Lambda_y^2 \Lambda_z}{\Lambda_y^2 + \Lambda_z^2} \qquad (2.18)$$

where Λ_z is first obtained from the q^2 decay, then restricted if necessary by eq. (2.17).

Even though the gross scale Λ has given us reasonable agreement with experiments (witness refs. 12-15), there still remains the desire to investigate the dynamic behavior of the scale based on

the solution of its own differential equation*.

Expressions for a dynamic scale equation have been formulated by several observers starting from the two-point velocity correlations (refs. 12, 16 and 17). Others have begun with the vorticity fluctuations or the dissipation function (refs. 18 and 19). As Bradshaw (ref. 20) and Mellor and Herring (ref. 21) point out, the principal terms in the resulting Λ equations are essentially the same for all of these formulations, namely

$$\frac{D\Lambda}{Dt} = - s_1 \frac{\Lambda}{q^2} \overline{u_i u_j} \frac{\partial u_i}{\partial x_j} - s_2 \nu \frac{\Lambda}{\lambda^2} + \text{DIFFUSION TERMS} \qquad (2.19)$$

where the constant s_1 multiplies the production term and s_2 multiplies the dissipation. The principal difference in expressions lies in the construction of the turbulent diffusion terms. After a great deal of numerical investigation, we feel that an adequate dynamic scale equation should contain at least two diffusion terms

$$\text{DIFFUSION TERMS} = \nu_c \frac{\partial}{\partial x_i} \left(q \Lambda \frac{\partial \Lambda}{\partial x_i} \right) - s_4 \frac{1}{q} \left(\frac{\partial q \Lambda}{\partial x_i} \right)^2 \qquad (2.20)$$

where the first term comes from our traditional definition of turbulent diffusion, found in eq. (2.7) and following equations, and s_4 multiplies a term which permits the diffusion of Λ to depend on the derivatives of q. More complicated expressions may be picked for the diffusion, but only at the expense of introducing more constants to be determined. For stratified flows, a term proportional to $(g_1/\rho_o) \overline{u_1' \rho'}$ should also be added to complete the current selection for the scale equation. Assembled, these terms give the following equation for the normalized dynamic scale Λ

---

*The analysis of a dynamic scale equation was funded jointly at A.R.A.P. by N00014-72-C-0413 and the Environmental Protection Agency under EPA 68-02-1310.

$$\frac{D\Lambda}{Dt} = v_c \frac{\partial}{\partial x_i}\left(q\Lambda \frac{\partial \Lambda}{\partial x_i}\right) - s_1 \frac{\Lambda}{q^2} \overline{u_i' u_j'} \frac{\partial u_i}{\partial x_j} - s_2 \nu \frac{\Lambda}{\lambda^2}$$

$$- s_3 \frac{\Lambda}{q^2} \cdot \delta_{3i} \frac{\overline{u_i' \rho'}}{Fr^2} - s_4 \frac{1}{q}\left(\frac{\partial q\Lambda}{\partial x_i}\right)^2 \qquad (2.21)$$

To obtain a consistant scale equation applicable to many different flow definitions, several different well-defined experiments must be matched concurrently if the resulting coefficients are to have any invariant validity.

The coefficient s_2 may be estimated from the decay of homogeneous grid turbulence. If homogeneous turbulence is assumed to decay as

$$q^2 \sim x^{-n} \qquad (2.22)$$

in the limit of $Re \to \infty$, then the q^2 equation, eq. (2.7), gives

$$\Lambda = \frac{bq^3}{-\frac{1}{2} U \frac{dq^2}{dx}} \qquad (2.23)$$

so that eq. (2.21) gives

$$s_2 = -\frac{U}{bq}\frac{d\Lambda}{dx} = \frac{n-2}{n} \qquad (2.24)$$

A recent review of grid turbulence experiments by Gad-el-Hak and Corrsin (ref. 22) shows values of n predominately between 1.0 and 1.3 with many values lying near 1.25. This value of n gives a value of $s_2 = -0.6$.

Relationships between the other three scale constants may be found by investigating flows near a boundary (ref. 13). In steady, neutral flow near a wall we know that

$$\Lambda = \alpha z \qquad (2.25)$$

where z is the distance normal from the wall and α is a proportionality constant currently set at 0.65. In this constant shear-stress layer, eq. (2.21) coupled with the energy equation yields the relationship

$$s_4 = v_c + \frac{b}{\alpha^2}(s_1 - s_2) \qquad (2.26)$$

In the case of a stably stratified layer, where the Richardson number is equal to its critical value and both Λ and q approach constant values, analysis demonstrates that for eq. (2.21) to be consistent with eq. (2.17) requires that

$$s_3 = s_1 + \frac{bq^3}{\Lambda}(s_1 - s_2) \qquad (2.27)$$

Equations (2.26) and (2.27) give us two relationships between s_1, s_2, s_3 and s_4. Numerical computer fit with axisymmetric jets and wakes (with or without momentum), plus a flat plate boundary layer, and a neutral planetary boundary layer, have been used to provide estimates of the one remaining constant and give a compatible middle ground across which the dynamic scale equation can reasonably govern. Our best fit to date gives $s_1 = -0.35$, $s_3 = 0.8$ and $s_4 = 0.375$.

Before we detail the comparison of the dynamic scale with several experimental flows, it is necessary to examine the application of appropriate boundary conditions to eq. (2.21). Although in most flow problems the boundary conditions for the mean variables such as q^2 or u_1 are known, the proper or accurate boundary condition on Λ may be indeterminate. In our numerical investigation of eq. (2.21), the edge condition on Λ was taken as proportional to the size of the gross scale found by the straightforward techniques discussed earlier. Thus, for example, we expect the largest eddies to spread to the edge of the axisymmetric flows, and therefore require that the edge value on Λ be twice

the gross scale found by eq. (2.16). A similar application is made to the other flows we have considered, with different factors multiplying the gross scale.

Our comparison of model predictions for axisymmetric flows made in ref. 14 may now be recalculated using eq. (2.21) rather than the gross constraint eq. (2.16). For the free jet calculation the initial condition on Λ is unimportant since only the final self-similar results are compared with observations. That comparison is made in figs. 2.1 and 2.2 with the results of ref. 14 and the observations of Wygnanski and Fiedler (ref. 23). Figure 2.3 compares the self-similar radial distributions of Λ with the longitudinal integral scale measurements of Wygnanski and Fiedler. The distributions are seen to be quite similar.

For the wake observations of Chevray (ref. 24) and Naudascher (ref. 25) we assume that Λ is determined initially by eq. (2.16). The decay of some of the important wake parameters are shown in figs. 2.4 through 2.7. Use of the dynamic scale equation does not materially affect the results. The radial distributions obtained some distance downstream of the initial station are given in fig. 2.8. The dashed line reflects the approximation used previously. Relatively little difference is observed between the two calculations.

A comparison of the effect of the dynamic scale equation in the flat plate boundary layer with the experimental data compiled by Coles (ref. 26) is shown in figs. 2.9 and 2.10. Also shown on this figure are the results from the gross scale assumption of eq. (2.16). The flow profiles possess very little difference.

We may also compare our model predictions for entrainment rates with the experiment of Kato and Phillips (ref. 27). They measured the entrainment of water in an annular tank with a shearing stress applied at the water's surface by a rectangular mesh

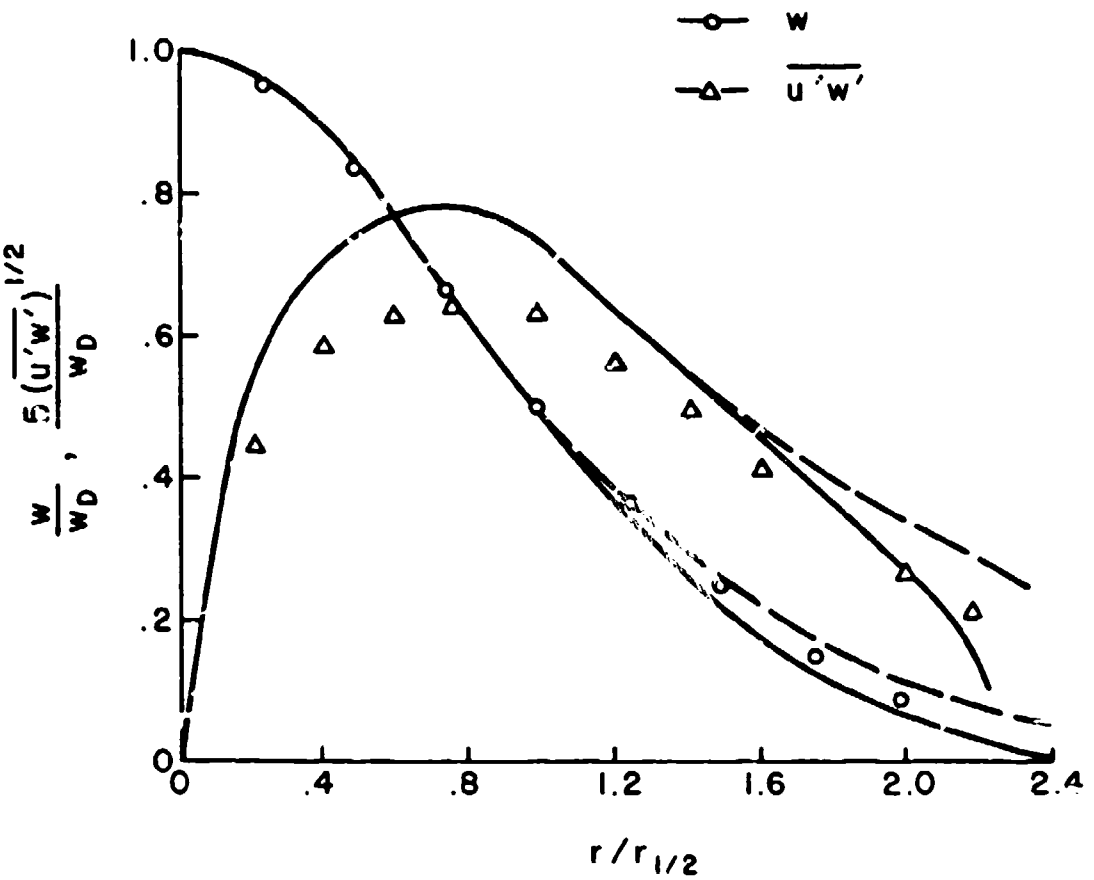

Figure 2.1: Comparison of self-similar jet velocity defect and shear stress data of Wygnanski and Fiedler (ref. 23) with model predictions for scale as determined by eq. (2.16) (—) or by eq. (2.21) (– –).

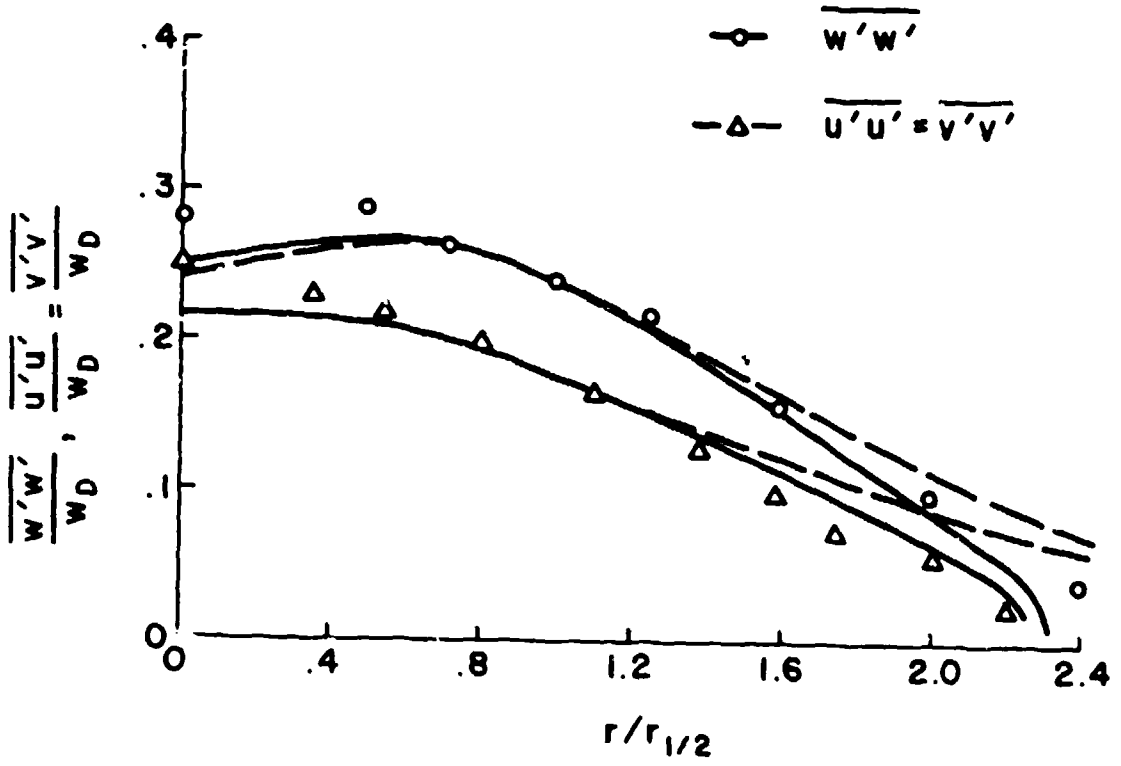

Figure 2.2: Comparison of turbulent energy components for the conditions of fig. (2.1).

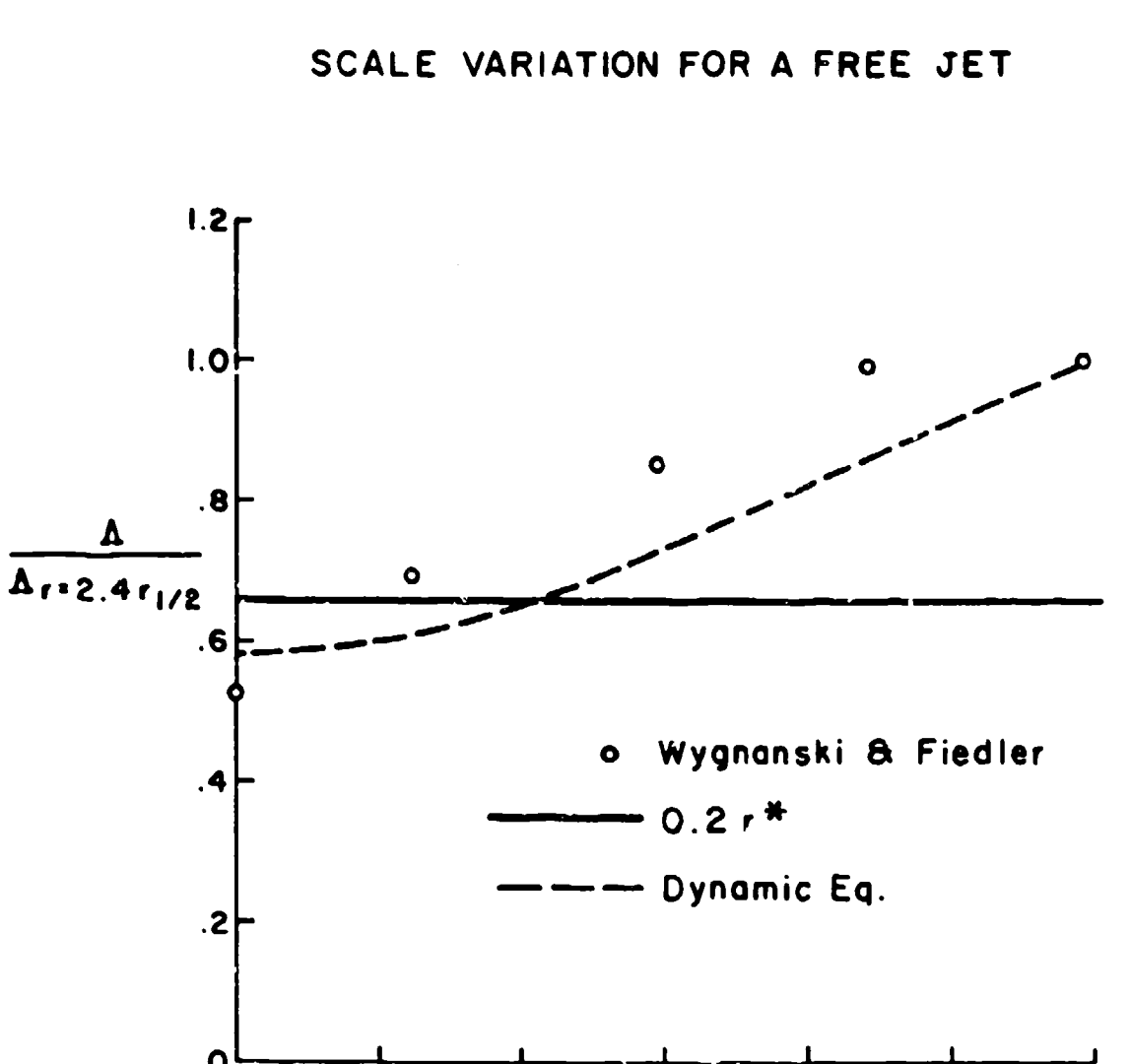

Figure 2.3: Comparison of dynamic scale variation with radius for the self-similar jet. Model prediction per eq. (2.16) (—) and eq. (2.21)(– –): Wygnanski and Fiedler (ref. 23) longitudinal integral scale variation, o .

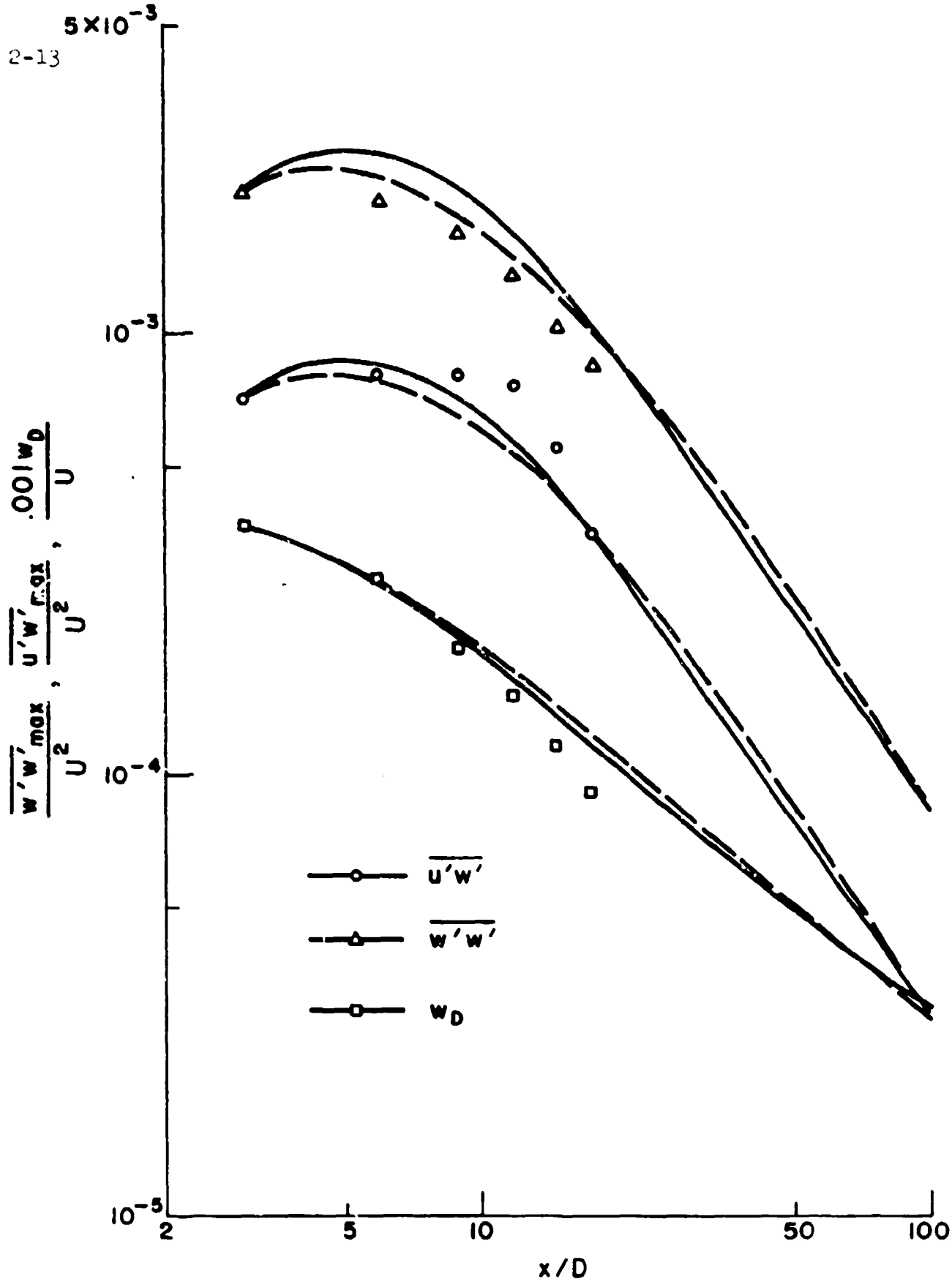

Figure 2.4: Comparison of the downstream decay of velocity defect, shear, and turbulent energy with scale from eq. (2.16) (—) and from eq. (2.21) (– –). Initial conditions and comparison data points as given by Chevray (ref. 24).

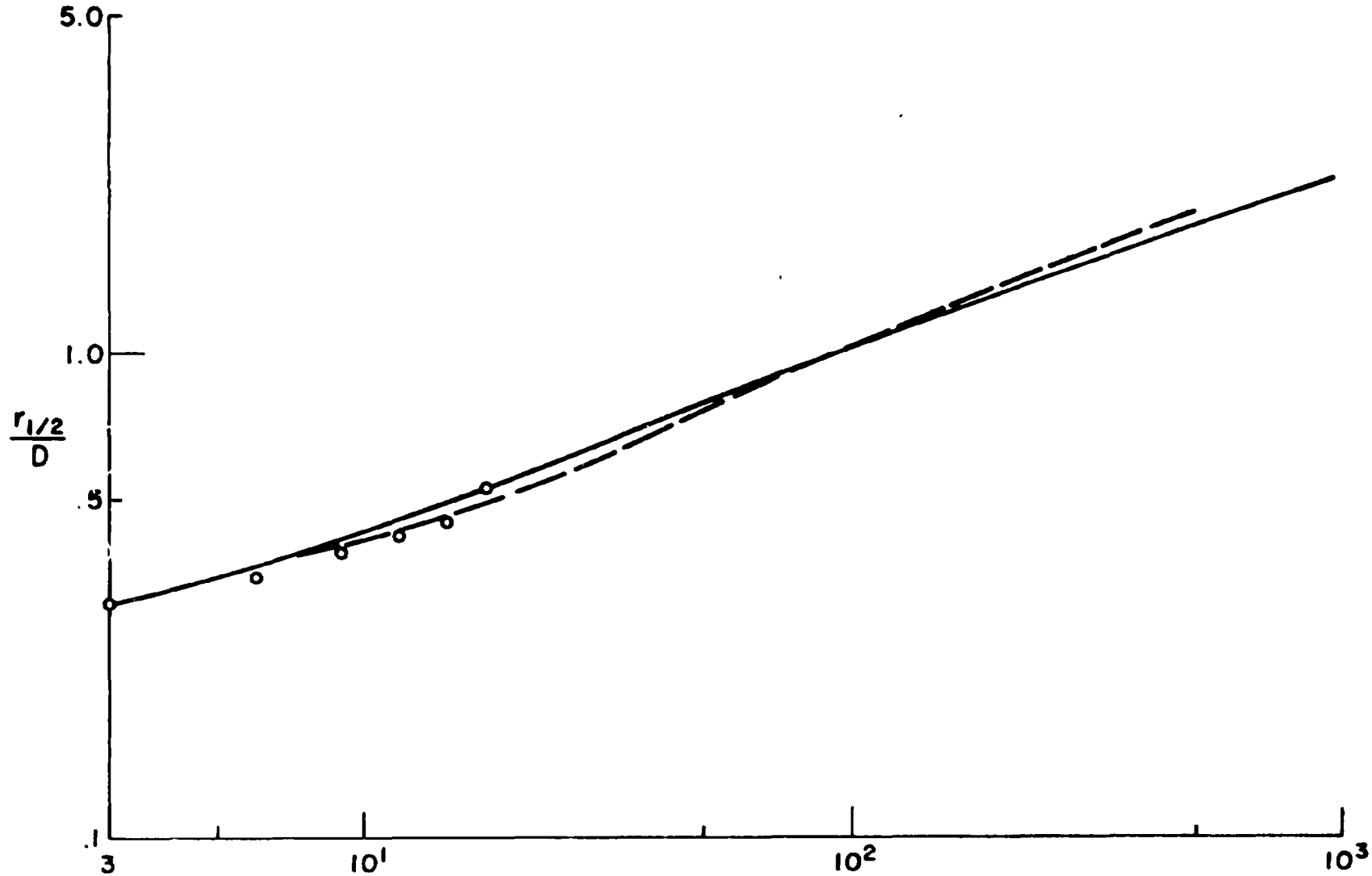

Figure 2.5: Comparison of the growth of wake radius for the conditions of fig. (2.4).

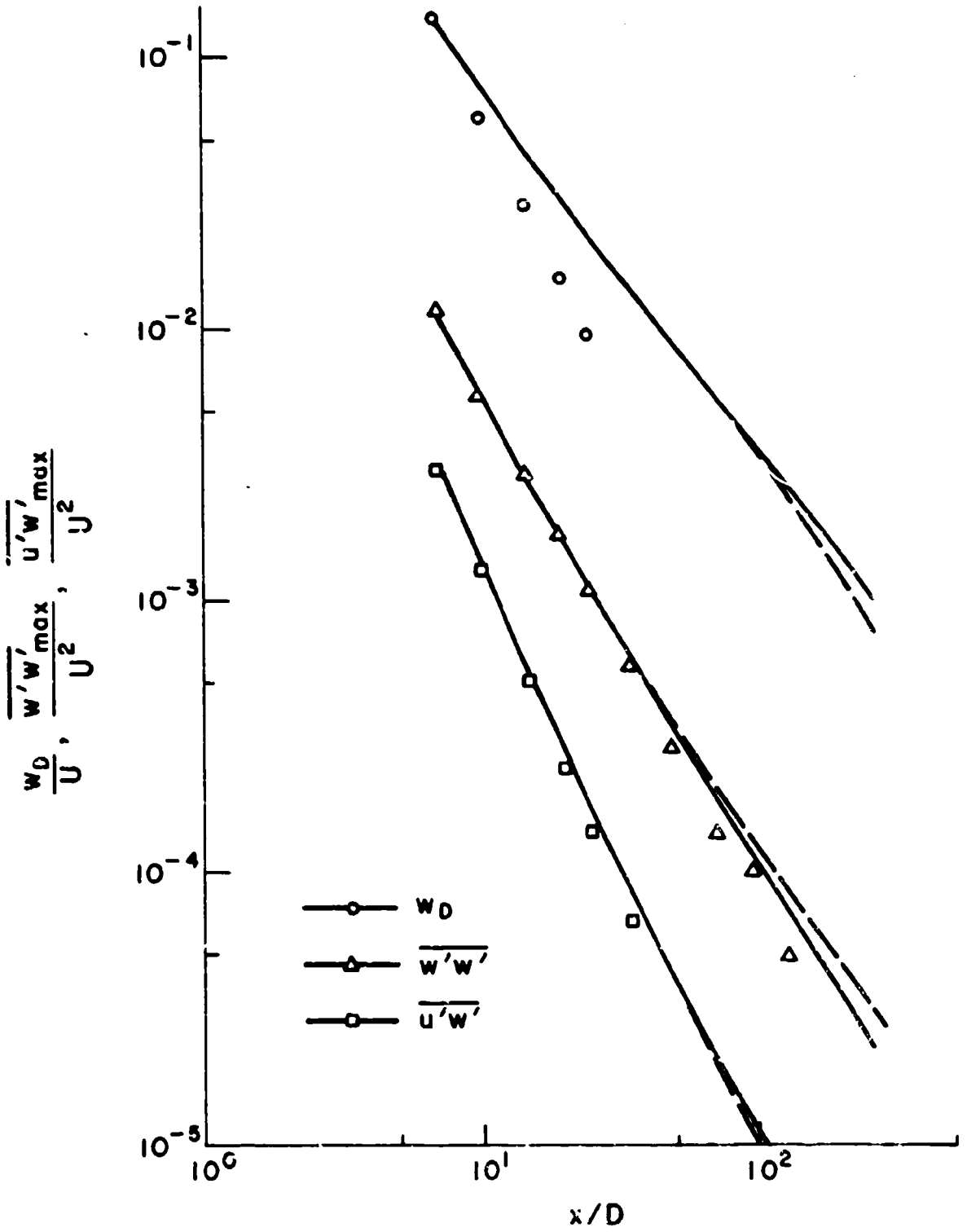

Figure 2.6: Comparison of downstream decay of velocity defect, shear, and turbulent energy with scale from eq. (2.16)(—) and from eq. (2.21)(– –). Initial conditions and comparison data points as given by Naudascher (ref. 25).

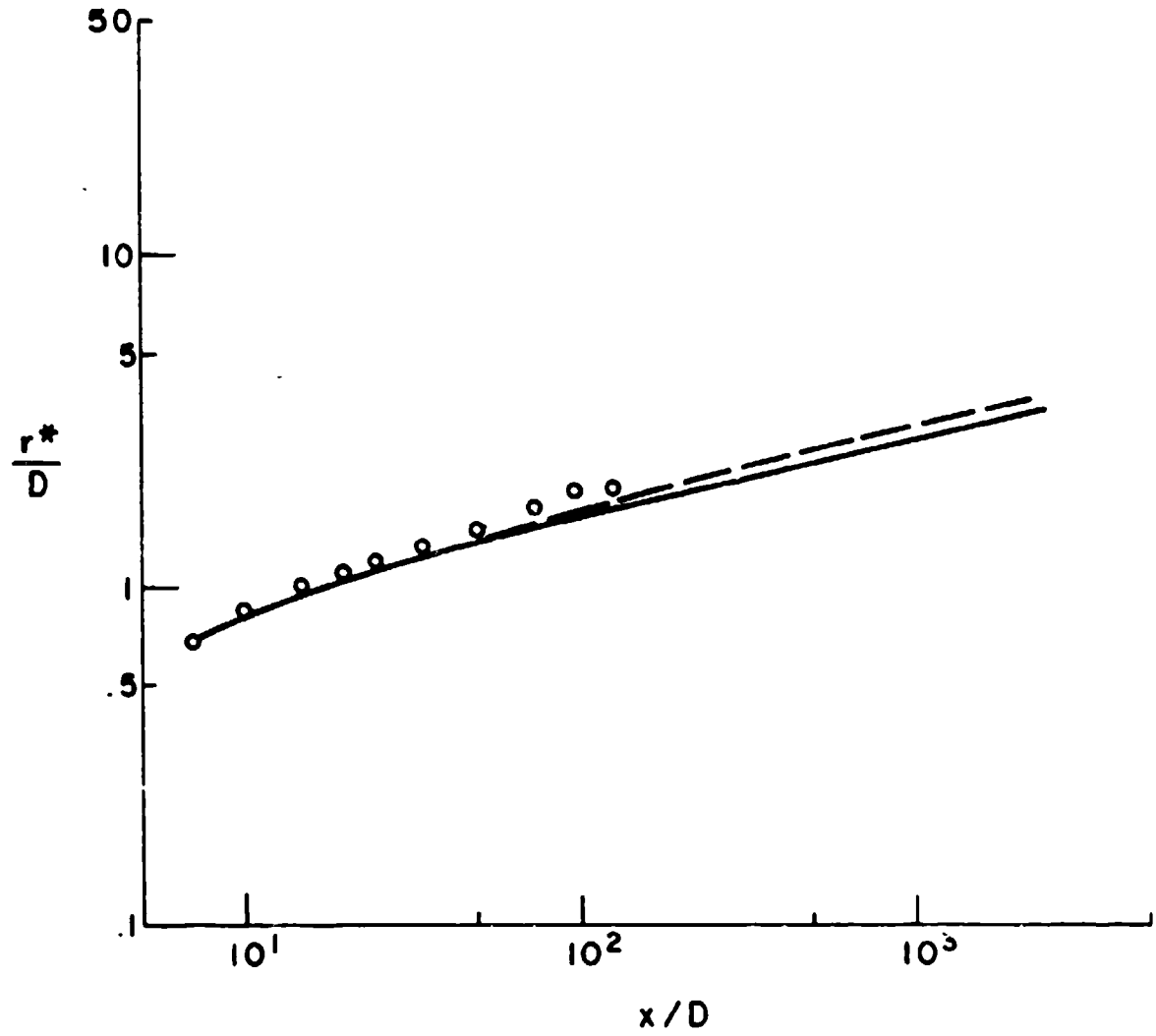

Figure 2.7: Comparison of the growth of turbulent wake radius for the conditions of fig. (2.6).

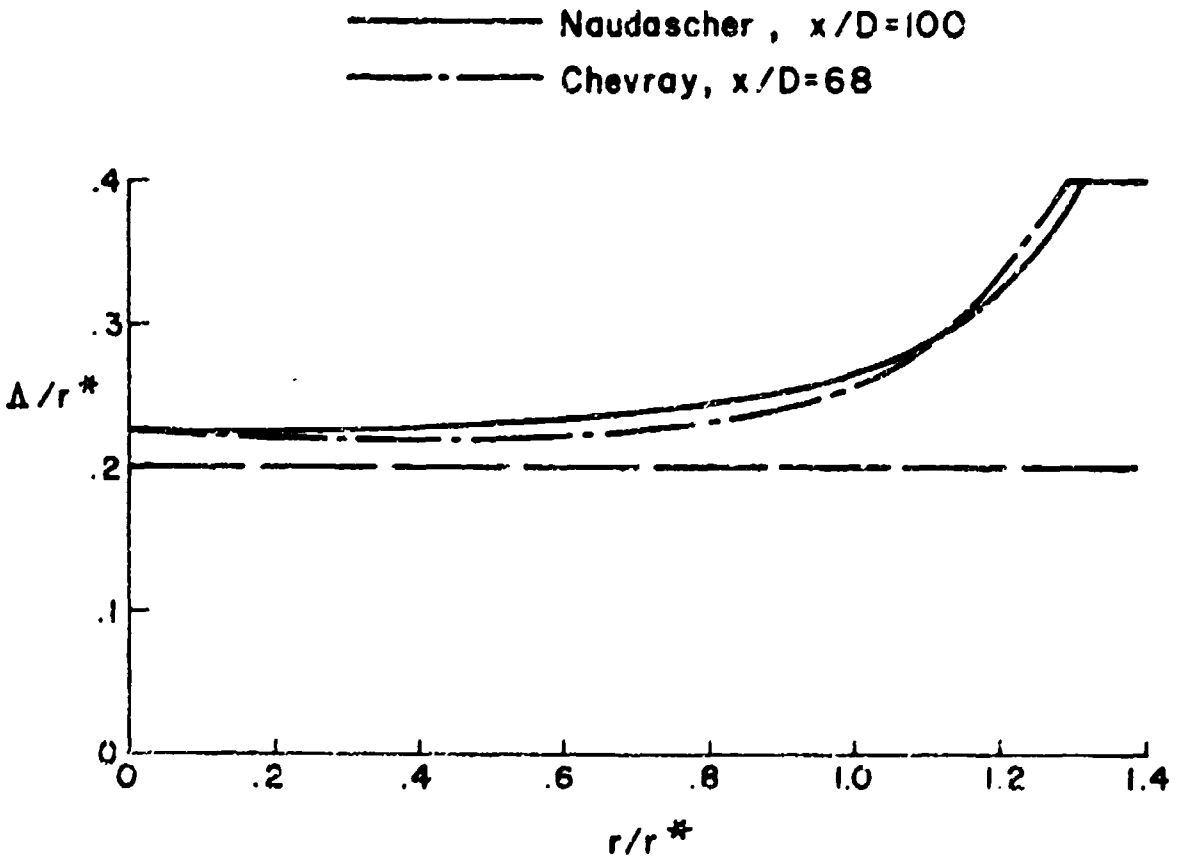

Figure 2.8: Comparison of scale behavior across the turbulent wake as given by eq. (2.16) (— —) and by eq. (2.21) (—, — — —) for the conditions of Naudascher (ref. 25) and Chevray (ref. 24).

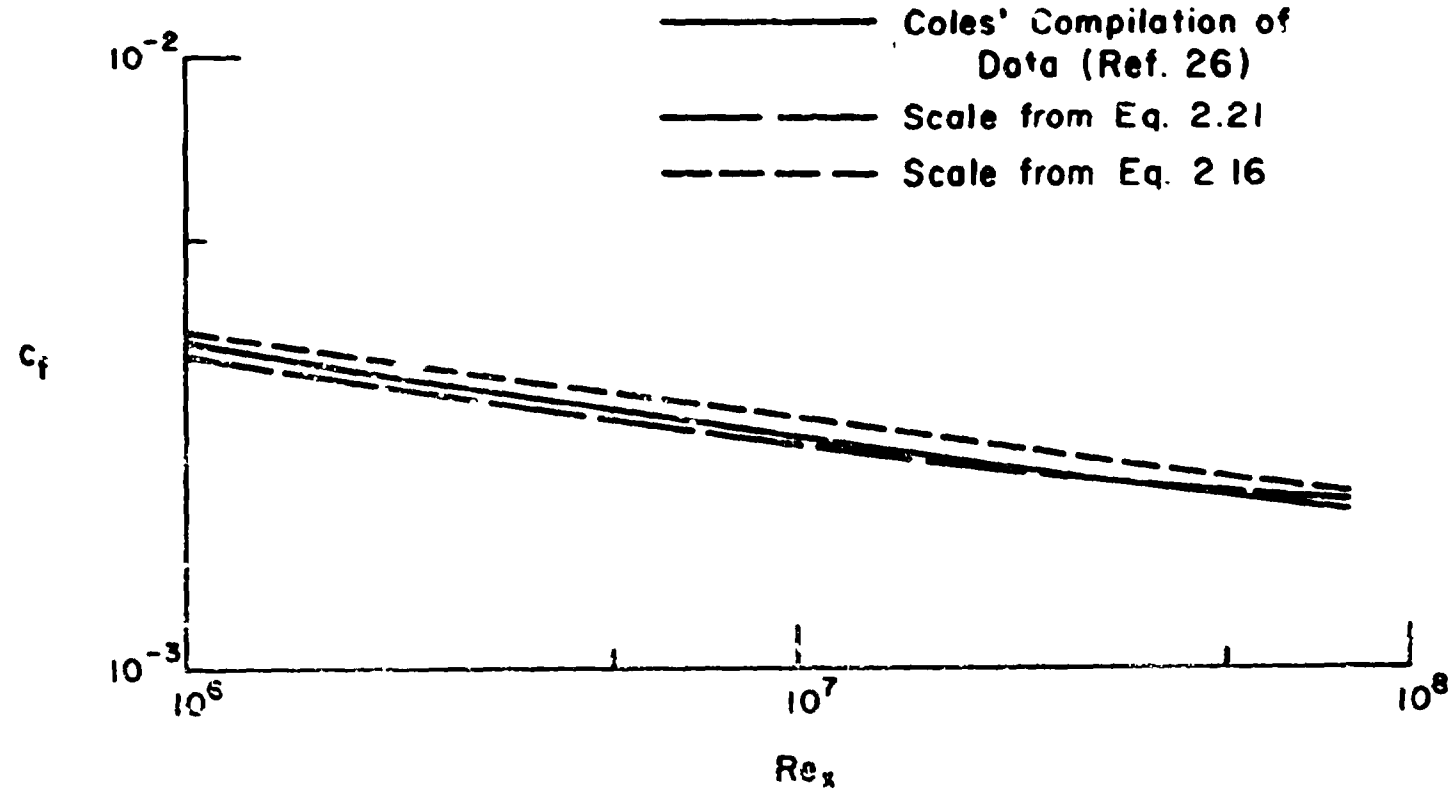

Figure 2.9: Comparison of scale behavior in predicting the friction coefficient C_f on a flat plate boundary layer, versus the running Reynolds number Re_x based on x distance downstream.

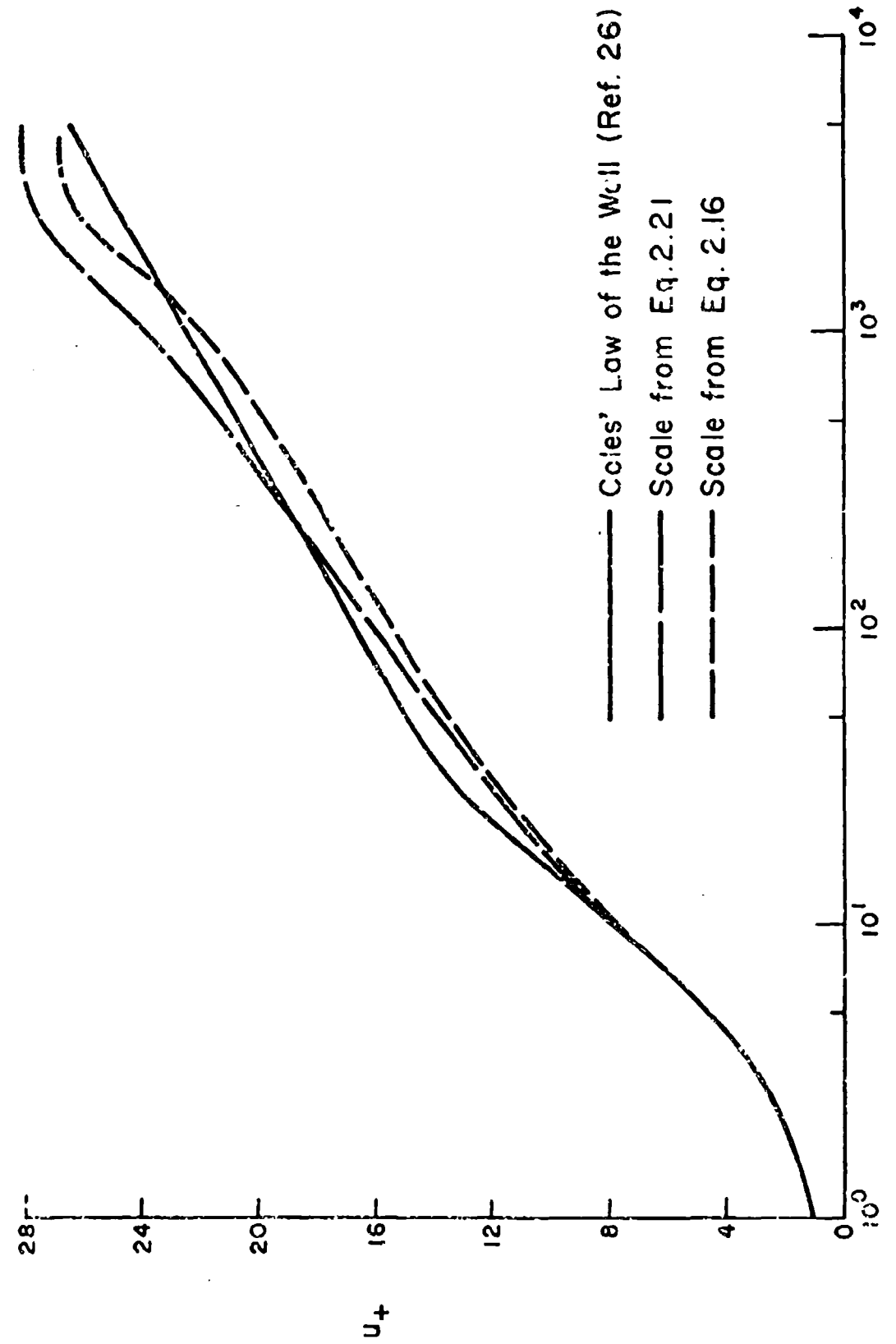

Figure 2.10: Comparison of scale behavior in predicting the law of the wall at $Re_x = 5 \times 10^6$.

flyscreen. The rate of spreading of the entrained fluid into the linear density field of the salt water could be measured visually by the injected dye position. Their experimental results of entrainment rate vs. flow Richardson number are given in fig. 2.11. Our comparisons using eq. (2.16) and eq. (2.21) are given by the solid and dashed curves, respectively. Although the dynamic scale rounds the apparently straight-line prediction of the gross scale model, it does not materially change the behavior of the entrainment with flow Richardson number. Neither model predicts quite as steep a decrease of entrainment with Richardson number as the data would indicate, but we judge either prediction to be satisfactory.

In summary then, it appears as though eq. (2.21), constrained by boundary conditions tied to the gross spread of the turbulence, provides a reasonable estimate for Λ. However, the behavior of Λ does not depart strongly from that by the gross scale features. Most of the calculations made in this report were made with Λ tied to the gross features of the q^2 profile and the Richardson cutoff. The dynamic scale was used in the investigation of the sensitivity of the wake to the initial scale presented in Section 4. The implementation of the dynamic scale equation in a previously unexamined flow configuration must be done carefully.

2.3 Computational Approximations

Equations (2.7) - (2.15) present a formidable solution task. To keep the problem within a manageable range for our in-house computer facility, we have made a number of assumptions to simplify the numerical analysis while hopefully retaining the physics of the wake collapse.

The first is the Quasi-Equilibrium (QE) approximation (discussed more fully in ref. 15) used in our stratified wake runs. Here we assume that the convective and diffusive character of all turbulence properties are represented by the dynamic behavior of the turbulent kinetic energy, eq. (2.7). Thus, for purposes of determining the relationships between the second-order correlations, we discard the total derivatives on the left sides of eqs. (2.13) - (2.15), and the diffusive terms on the right sides. For the large Reynolds number flows that we consider, λ may be carried to the limit of

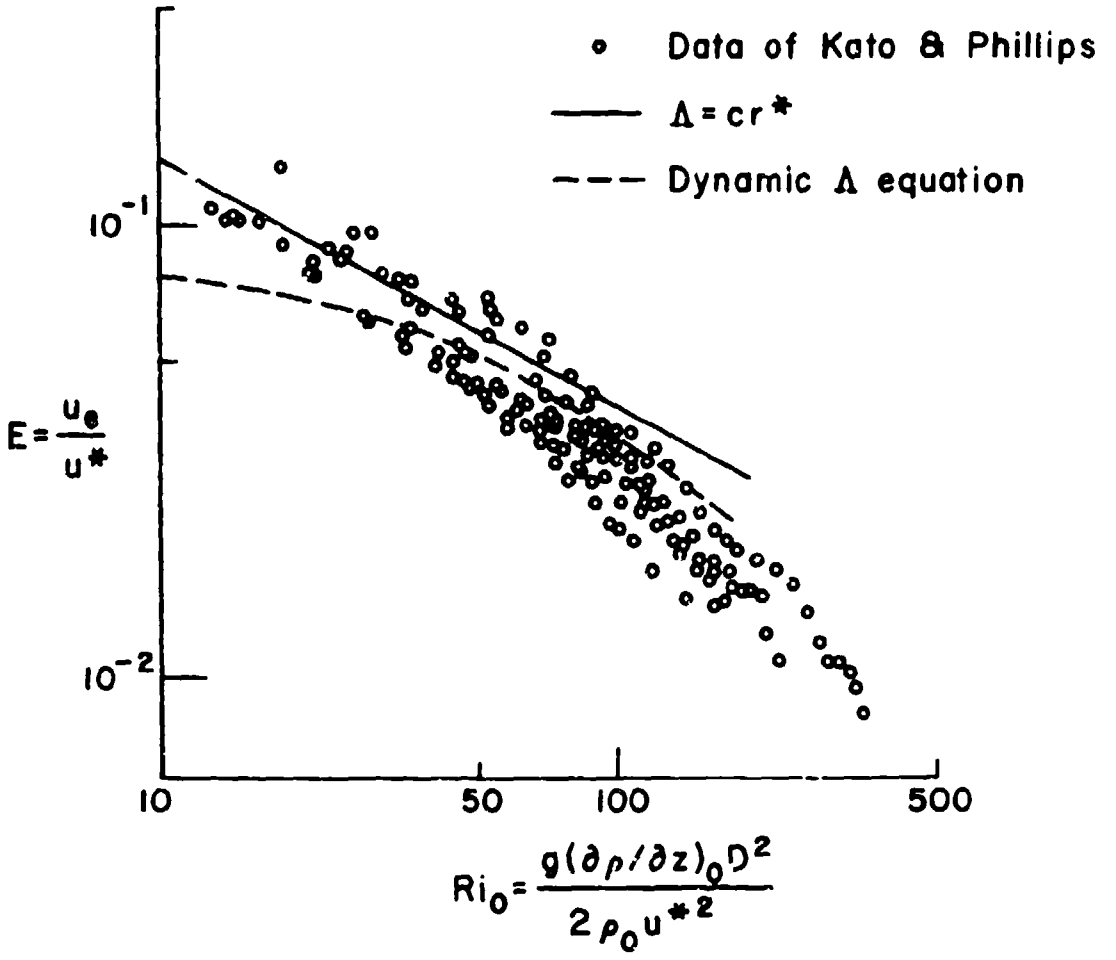

Figure 2.11: Comparison of prediction of entrainment rate E vs. shear layer Richardson number Ri_o for scale as given by eq. (2.16) (—) and by eq. (2.21) (– –). Data as given in ref. 27.

Re → ∞ to write

$$\frac{\nu}{\lambda^2} = \frac{bq}{\Lambda} \tag{2.28}$$

In order to carry a separate equation for q^2 as well as the algebraic relationships for $\overline{u'u'}$, $\overline{v'v'}$ and $\overline{w'w'}$, we include an isotropic correction factor $f(x,y,z)$ in the energy component equations so that q^2 will always result from summing $\overline{u_i'u_i'}$. The final form of this algebraic set of ten equations becomes

$$0 = -\overline{u_i'u_k'}\frac{\partial u_j}{\partial x_k} - \overline{u_j'u_k'}\frac{\partial u_i}{\partial x_k} - \frac{\delta_{3i}}{Fr^2}\overline{u_j'\rho'} - \frac{\delta_{3j}}{Fr^2}\overline{u_i'\rho'}$$

$$- \frac{q}{\Lambda}\left(\overline{u_i'u_j'} - \frac{\delta_{ij}}{3}q^2\right) - 2(b-f)\frac{q^3}{3\Lambda}\delta_{ij} \tag{2.29}$$

$$0 = -\overline{u_i'u_j'}\frac{\partial \tilde{\rho}}{\partial x_j} - \overline{u_j'\rho'}\frac{\partial u_i}{\partial x_j} - \frac{\delta_{3i}}{Fr^2}\overline{\rho'^2} - \frac{Aq}{\Lambda}\overline{u_i'\rho'} \tag{2.30}$$

$$0 = -\overline{u_j'\rho'}\frac{\partial \tilde{\rho}}{\partial x_j} - \frac{sbq}{\Lambda}\overline{\rho'^2} \tag{2.31}$$

It can be seen from eqs. (2.29) - (2.31) that the turbulent fluctuations depend only upon mean flow derivatives and the local q^2 value. It would seem reasonable to upgrade the solution scheme by retaining the full dynamic equation for $\overline{\rho'^2}$ as suggested by Mellor and Yamada's (ref. 28) expansion about isotropic turbulence. This has not been done, however. Solution comparisons with eqs. (2.29) - (2.31) in operation, as opposed to the use of the full equations, were presented for the axisymmetric Naudascher case in ref. 15. The agreement in the dynamic response is good, with a maximum difference of 10% occurring in the mean velocity departure when it has decayed an order of magnitude from the initial conditions. The dramatic reduction in the number of differential equations requiring full numerical solution appears to give ample justification for this slight loss in accuracy.

The algebraic solution of eqs. (2.29) - (2.31) for the correlations as a function of q, Λ, Fr, and the mean flow derivatives is not a trivial problem, however. To further

facilitate our obtaining a solution, we retain only the principal derivatives of u and $\hat{\rho}$ in y and z. This assumption requires that v and w derivatives be $\ll q/\Lambda$. However, in order not to lose the major influence of v and w derivatives on the $\overline{v'w'}$ correlation, the contributions of $\partial v/\partial z$ and $\partial w/\partial y$ for isotropic turbulence are added to that obtained by the above procedure. The expressions for the correlations as used in our QE approximation are given in Part II.

As noted in ref. 15 we have also experimented with modifying the diffusion terms in eq. (2.7) to allow turbulent diffusion to be more anisotropic. This is done by replacing $v_c q \Lambda$ by $3v_c(\overline{v'v'}/q)\Lambda_y$ for diffusion in the y direction and $3v_c(\overline{w'w'}/q)\Lambda_z$ in the z direction, with Λ_y, Λ_z computed as given in Section 2.b. The slight difference in entrainment this yields for the stratified experiment of Kato and Phillips (ref. 27) is shown in fig. 2.12. The stratified wake runs reported in Section 4 were made using the anisotropic form.

Equations (2.7) - (2.19) and the scale eq. (2.21) are solved by the ADI method of Peaceman, Rachford and Douglas(refs 29 and 30). A more complete discussion of our application of this technique is given in Part II of this final report. In summary, the equations are written in finite difference form and solved on an unequally spaced y - z mesh, with the solution marching downstream in x. A Phase I calculation involves only q^2, $\hat{\rho}$ and u (no collapsing cross-velocities). Phase II, reported on in ref. 15, solves for q^2, $\hat{\rho}$, v, w and π; while Phase III encompasses the complete solution to all equations. The equations are linearized about their previous x step in such a way that each equation is solved implicitly without coupling to the other equations.

The solution is relatively slow (on the order of 6 minutes of Digital Scientific Corporation META-4 computer time per step) because of the need in the cross-plane for solution of the

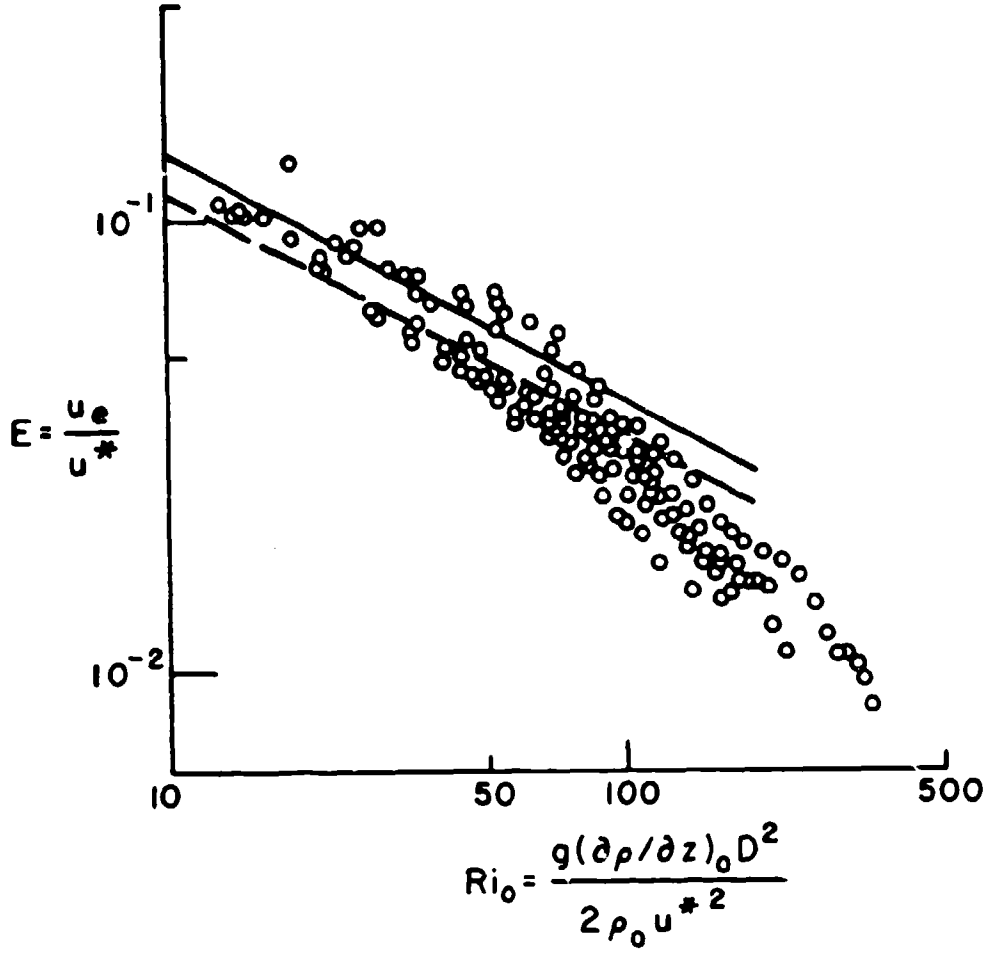

Figure 2.12: Comparison of entrainment rate prediction for isotropic (—) and anisotropic (– –) diffusion. Data (o) from Kato and Phillips (ref. 27).

pressure perturbation π . To solve the Poisson equation $\nabla^2\pi = F$ at every step in the flow, we add two additional terms to eq. (2.12). We first realize that our numerical scheme cannot in itself maintain a divergence-free cross-plane flow; numerical roundoff error prevents the exact solution of eq. (2.1) for v and w . To aid in maintaining accuracy, since a divergent velocity will stimulate an instability, we employ the standard procedure (ref. 29) of adding a term of the form $\partial/\partial x\ (\nabla \cdot \bar{v})$ to the right side of eq. (2.12). At every step we correct for zero divergence at the next step. In order to solve Poisson's equation in the elliptic-like region of a submarine wake, we add a time-like term to the left side of eq. (2.12) to arrive at a diffusion-like parabolic equation for π of the form

$$\frac{\partial \pi}{\partial t} = \nabla^2\pi - F + \frac{\partial}{\partial x}\left(\frac{\partial v}{\partial y} + \frac{\partial w}{\partial z}\right) \tag{2.32}$$

The pressure perturbation is obtained by iteration toward the next step a Δx distance away, using the present pressure profile as a first guess. We have modified the "ideal" time stepping for a rectangular flow region (ref. 30) to take steps as

$$\Delta t(i) = y_s z_s / P_N(i) \tag{2.33}$$

where y_s and z_s are the spreads of the mesh solution in the y and z directions, and $P_N(i)$ is an array of constants

$$P_N(i) = (10.0,\ 30.0,\ 60.0,\ 100.0,\ 150.0) \tag{2.34}$$

Certain minimum error and cutoff criteria may terminate the pressure solution prior to its completing the optimized five iterations (ref. 31). Step sizes are limited by the possibility

that the flow changes too rapidly for the pressure to maintain a divergence-free environment. Loss of numerical accuracy and solution believability follow rapidly. Many checks, both numerical and visual, accompany the run of a collapsing wake beyond one Brunt-Väisälä period.

The principal product of a collapsing wake is radiated internal gravity waves. Near the edges of our mesh, we may generally impose zero boundary conditions on q^2 and u. To require that $\hat{p}$, π, v and w also equal zero here requires that we construct an artificial liner to contain and absorb any waves reaching it. For this purpose we add a decay term $-kv$ to the right size of eq. (2.10) and $-kw$ to the right side of eq. (2.11), where

$$k = \begin{cases} 0 & r < s_p \\ \frac{1}{2}\left[\exp(+T) + \exp(-T)\right] - 1 & \\ T = c_p(r^2 - s_p^2) & r > s_p \end{cases} \qquad (2.35)$$

A figure illustrating the successful use of this liner is contained in ref. 15. The liner cannot lie so close as to dictate the solution, nor can it be so far away that the mesh loses a proper definition of the turbulent wake dynamics. As long as the liner is placed more than 10λ away from the center of the wake, the position of the liner alters the flow solution by no more than 5% of local maximum values (ref. 15).

Taken together, the numerical simplifications do not materially detract from the ability of the wake program to perform to expectation. In the next Section we will catalogue some of the further comparisons with experimental data of our axisymmetric programs and the wake program itself. The Section following that will discuss the sensitivity studies we have carried out with our operational computer programs.

3. COMPARISON OF MODEL PREDICTIONS WITH LABORATORY DATA

3.a Unstratified Flows

Having addressed ourselves to the derivation of the equations of motion governing a developing wake in a stratified fluid, we now turn to further verification of our model predictions with data obtained in the laboratory. We have previously (in refs. 13 and 14) dealt with our model predictions in the atmospheric surface layer and the axisymmetric flow configurations of a free jet and wakes with varying momentum. We will first investigate some further comparisons with unstratified flow experiments, and then turn to the stratified towing tank experiments of Flow Research, Inc.

Recent wind tunnel work by Schetz and Jakubowski at VPI (ref. 32) reexamined the Naudascher experiments with a nonswirling injection model and a swirl-induced propeller model. The data given to us was recorded at their first station behind the body, at $x/D = 2$. In the nonswirling case, the data exhibited some irregularity and required interpolation near $r = 0$ to yield an adequate set of initial conditions with which to begin an axisymmetric numerical calculation as shown in fig. 3.1. Comparisons between the data and our wake predictions are presented in figs. 3.2 - 3.4 for the centerline velocity excess and the maximum values of the shearing stress and longitudinal turbulent correlation. No changes have been made in the model constants or solution technique from that presented previously.

The centerline velocity gives a good representation to the data. It should be noted that the initial data station at $x/D = 2$ is not plotted in fig. 3.2 because $w_D < 0$ there. The shear stress in fig. 3.3 matches the data points quite well. Figure 3.4 plots the comparison of our prediction of $\overline{w'w'}_{max}$ with the data taken in the experiment. Here we are at variance with the experiment. Our theoretical prediction comes relatively quickly to a decay rate similar to Naudascher's experimental result. We have no explanation for why the turbulence should decay so much slower in this momentumless experiment.

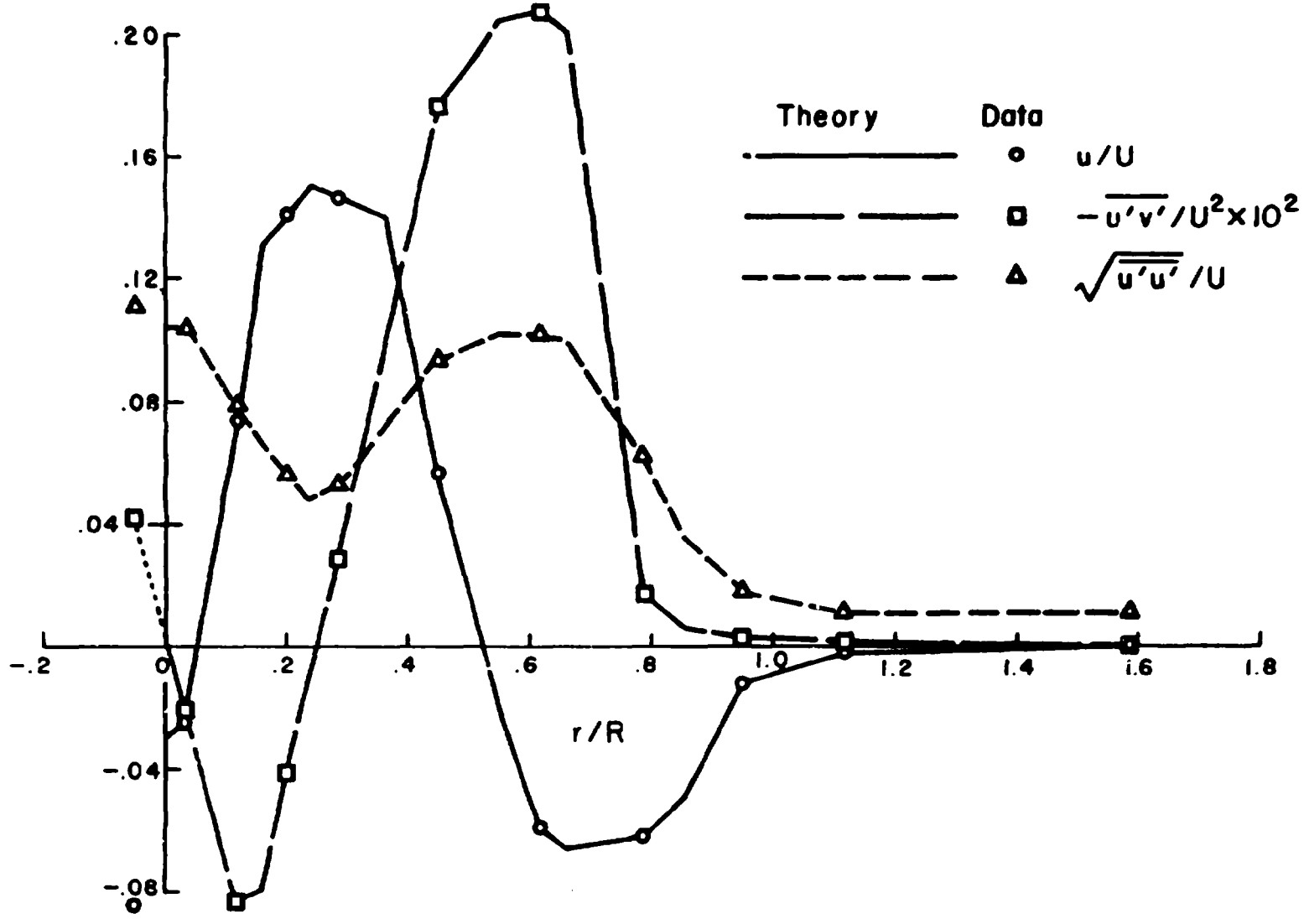

Figure 3.1: The initial computer profiles for velocity defect, shear, and turbulent energy for the nonswirling data of Schetz and Jakubowski (ref. 32).

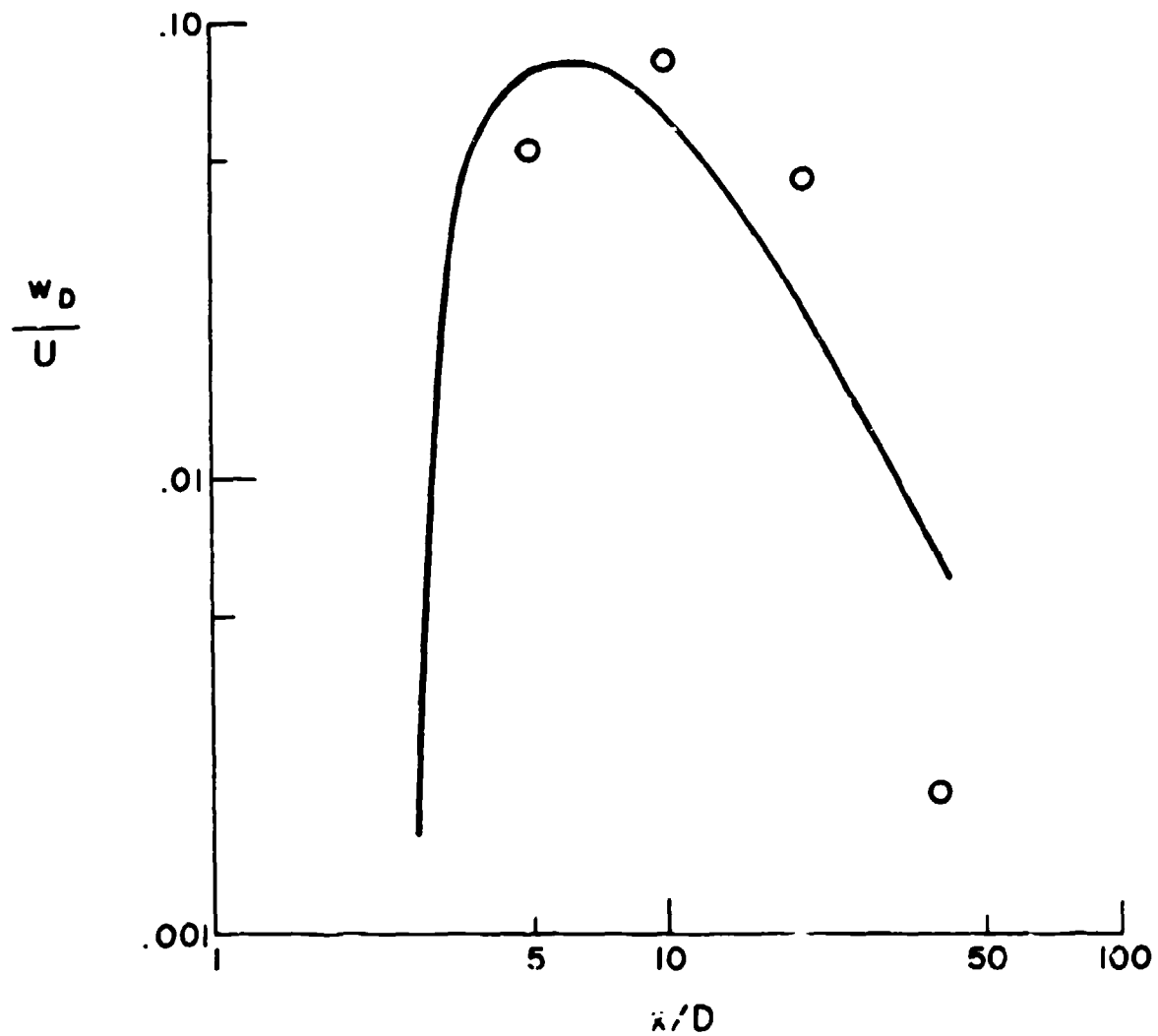

Figure 3.2: Comparison of the prediction of the decay of the velocity defect for the initial conditions given in fig. 3.1 with the observations (o) of Schetz and Jakubowski (ref. 32).

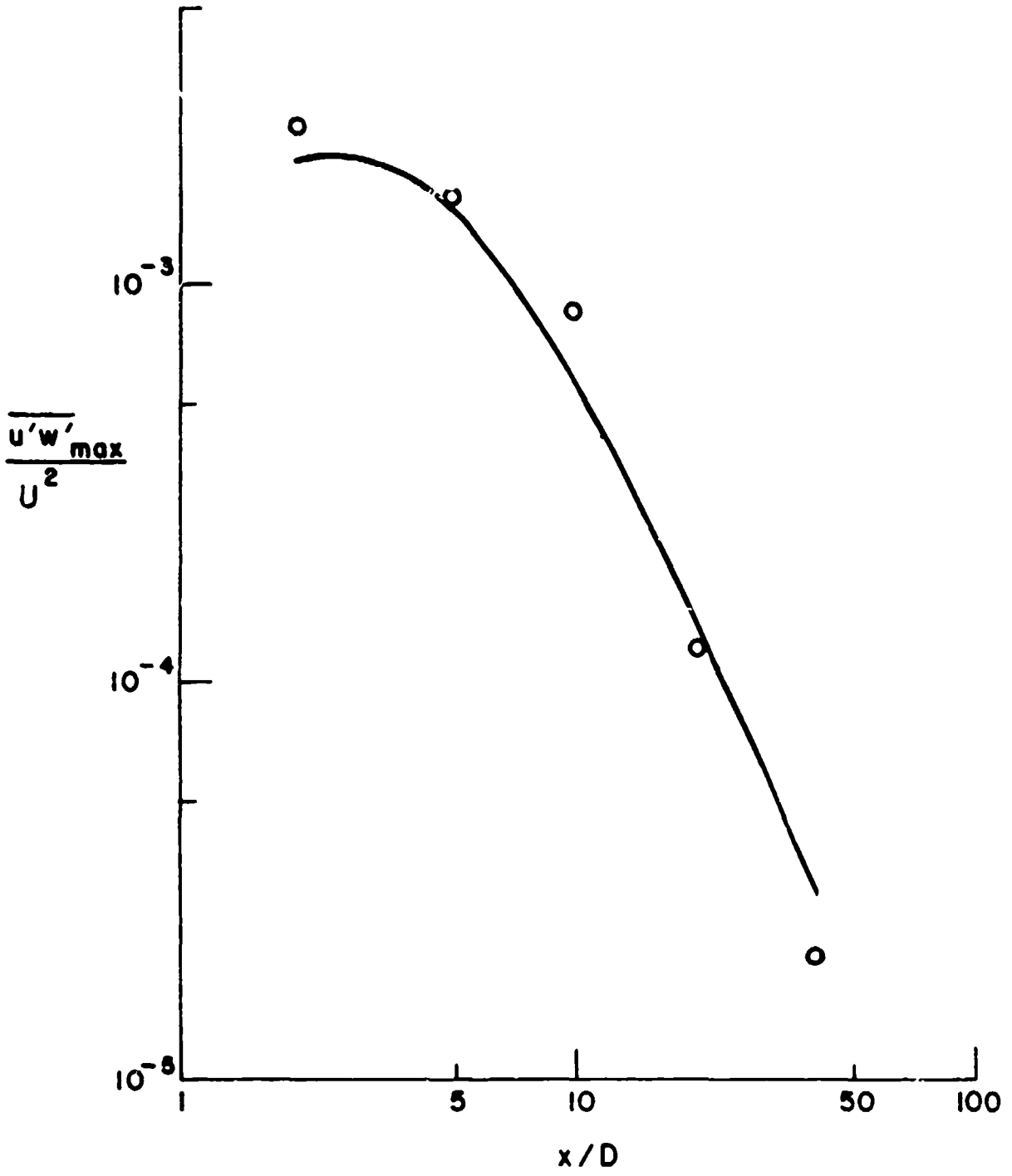

Figure 3.3: Comparison of the prediction of the decay of shear stress for the initial conditions given in fig. 3.1 with the observations (o) of Schetz and Jakubowski (ref. 32).

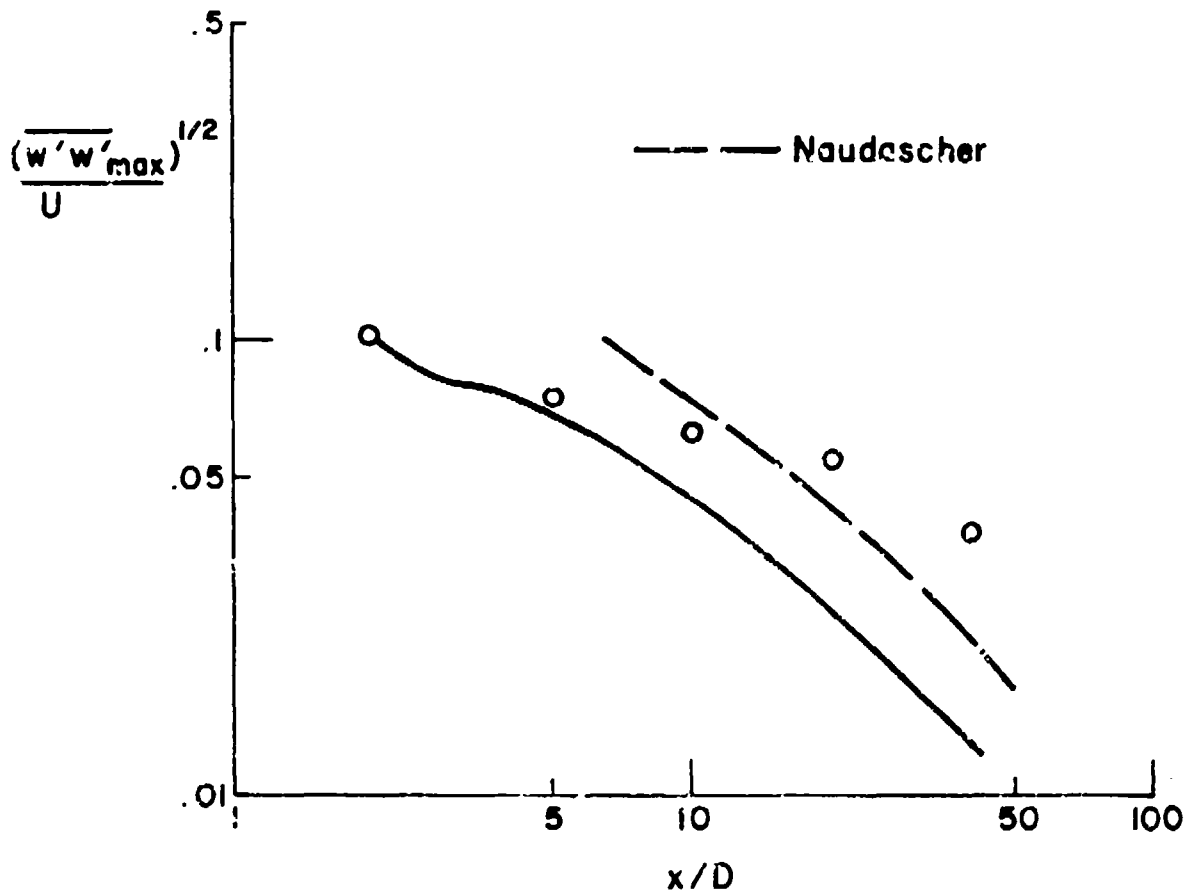

Figure 3.4: Comparison of the prediction of the decay of turbulent energy for the initial conditions given in fig. 3.1 with the observations of Schetz and Jakubowski (ref. 32). Also shown is the decay characteristic from the data of Naudascher (ref. 25).

Schetz and Jakubowski also studied a swirling case, and our comparisons with their results are shown in fig. 3.5 - 3.8. To obtain our predictions, we have used the A.R.A.P. 3-D vortex program for axisymmetric flow developed by R. D. Sullivan for ARL (ref. 33). Our fit to the conditions at $x/D = 2$ are given in fig. 3.5. A dynamic scale equation is not used here, but the gross scale features are prescribed as in the axisymmetric, non-swirling flows. Beginning with the limited data from Schetz (rather than both $\overline{u'v'}$ and $\overline{u'w'}$ only the principal shear stress was reported) we predict the solutions for centerline w_D, $\overline{u'w'}_{max}$ and $\overline{w'w'}_{max}$ as shown by solid lines in figs. 3.6 - 3.8. In fig. 3.6 we see that w_D follows the data fairly well. The comparisons with $\overline{u'w'}_{max}$ and $\overline{w'w'}_{max}$ are not as favorable. The shear stress is predicted to decay faster than that observed while the axial velocity fluctuation decays slower than observed. At least the asymptotic rates of decay of the axial velocity fluctuations are the same.

Overall, the comparisons with Schetz's data are somewhat disappointing. We expect the model to be more accurate than these comparisons indicate. Whether these discrepancies indicate some defect in the model, such as the treatment of the scale Λ (particularly in the swirling case) or some inconsistency in our interpretation of the data, cannot be determined until we have the opportunity to examine a more complete reporting of the experimental observations.

While at TRW, Gran (ref. 34) performed a reexamination of Naudascher's experiments on momentumless wakes, but with the presence of swirl. Our comparisons with these results are presented in figs. 3.9 - 3.12. In fig. 3.9 we do quite well in our estimate of centerline velocity excess; we are just below the error bars near $x/D = 10$. Figure 3.10 compares our prediction of the maximum axial turbulent intensity; we asymptote properly but lie slightly above Gran's data. Our prediction of

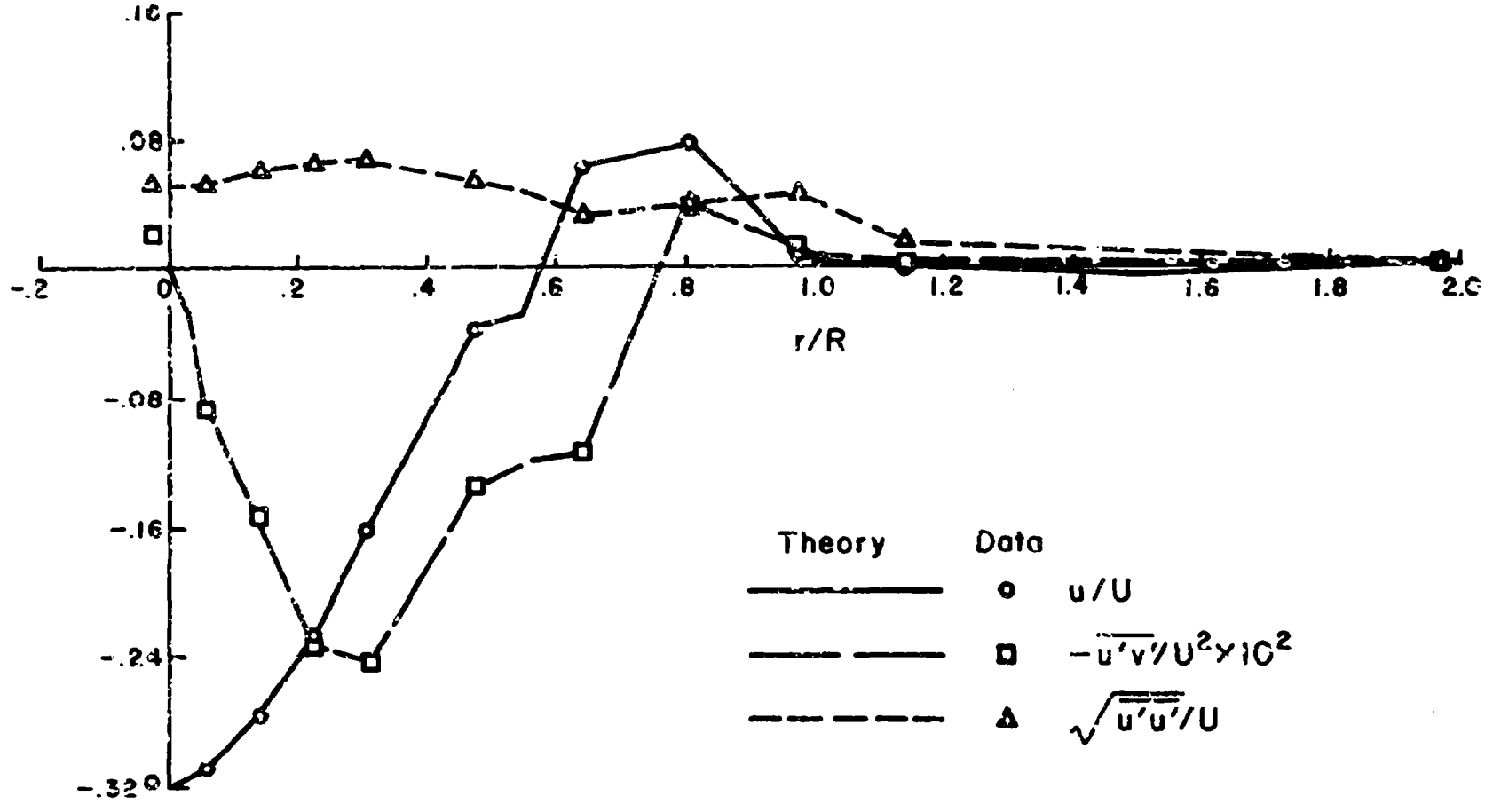

Figure 3.5: The initial computer profiles for velocity defect, shear, and turbulent energy for the swirling data of Schetz and Jakubowski (ref 32).

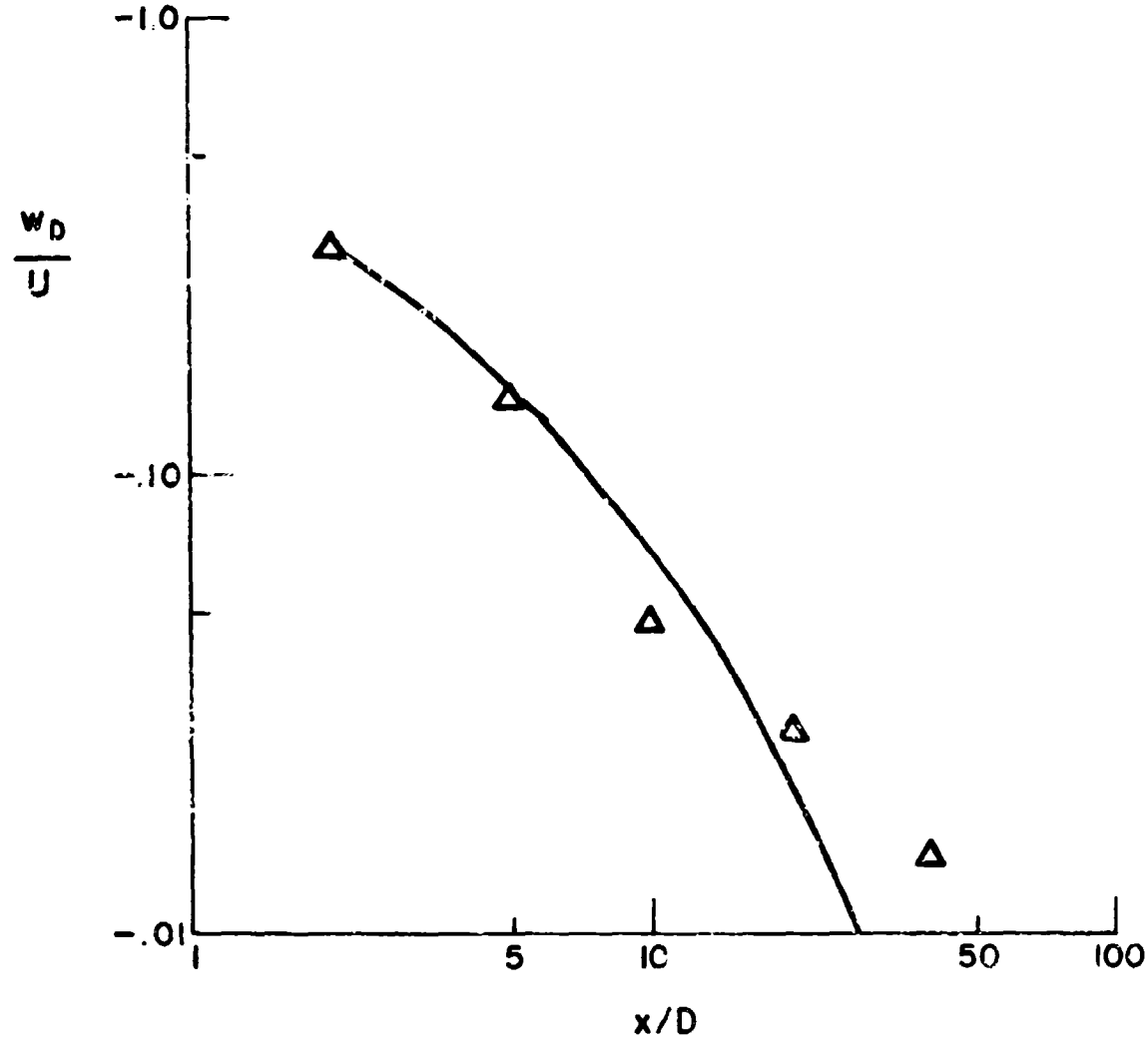

Figure 3.6: Comparison of the prediction of the decay of velocity defect for the initial conditions given in fig. (3.5) with the observations of Schetz and Jakubowski (ref. 32).

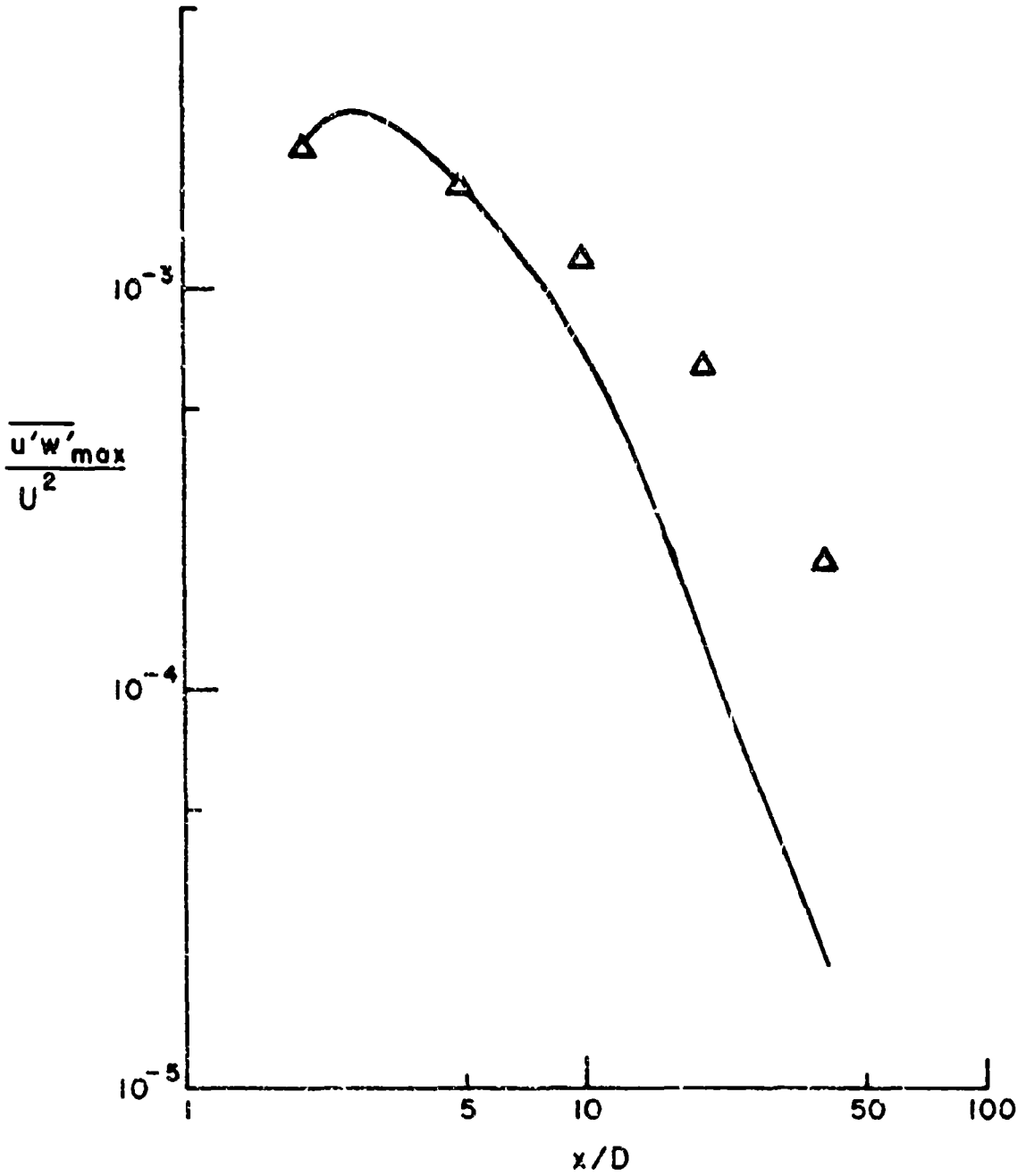

Figure 3.7: Comparison of the prediction of the decay of shear stress for the initial conditions given in fig. (3.5) with the observations of Schetz and Jakubowski (ref. 32).

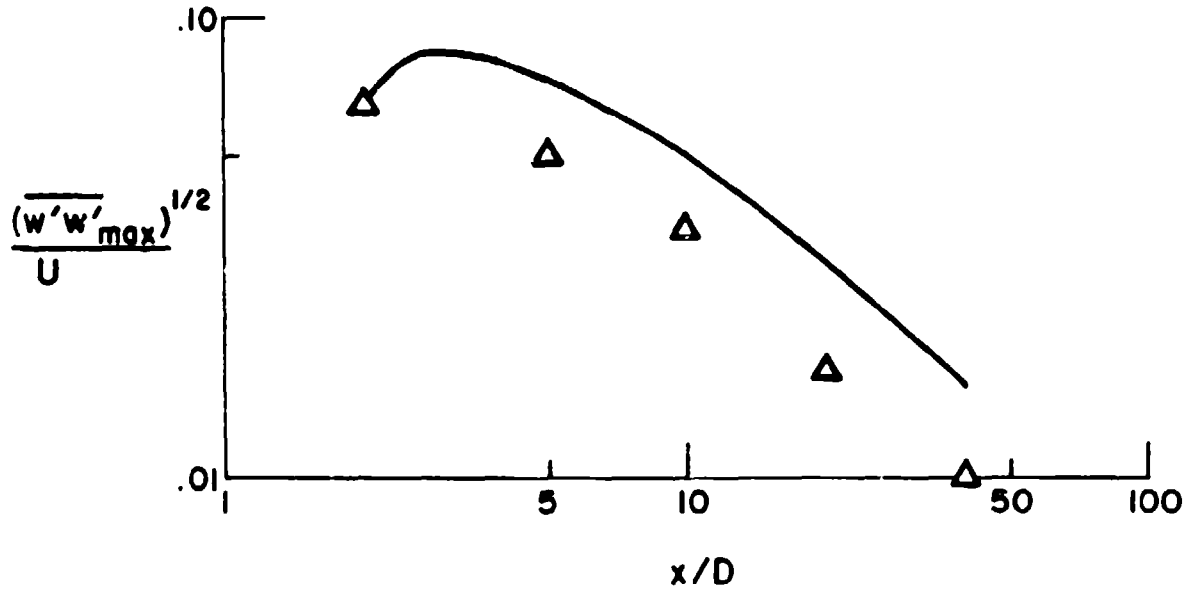

Figure 3.8: Comparison of the prediction of the decay of turbulent energy for the initial conditions given in fig. 3.5 with the observations of Schetz and Jakubowski (ref. 32).

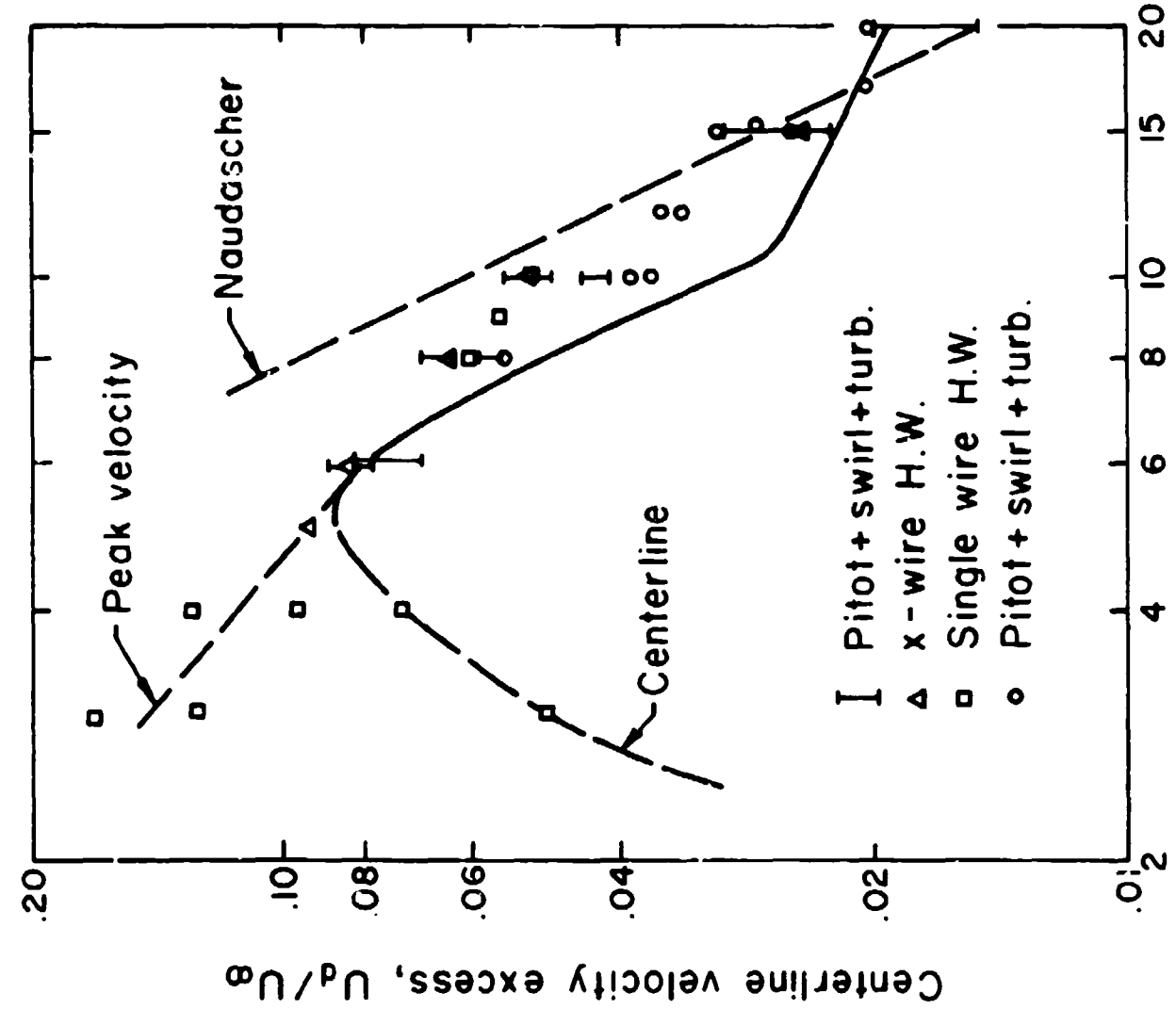

Figure 3.9: Comparison of the prediction of the decay of centerline velocity excess with the data of Gran (ref. 34) and Naudascher (ref. 25).

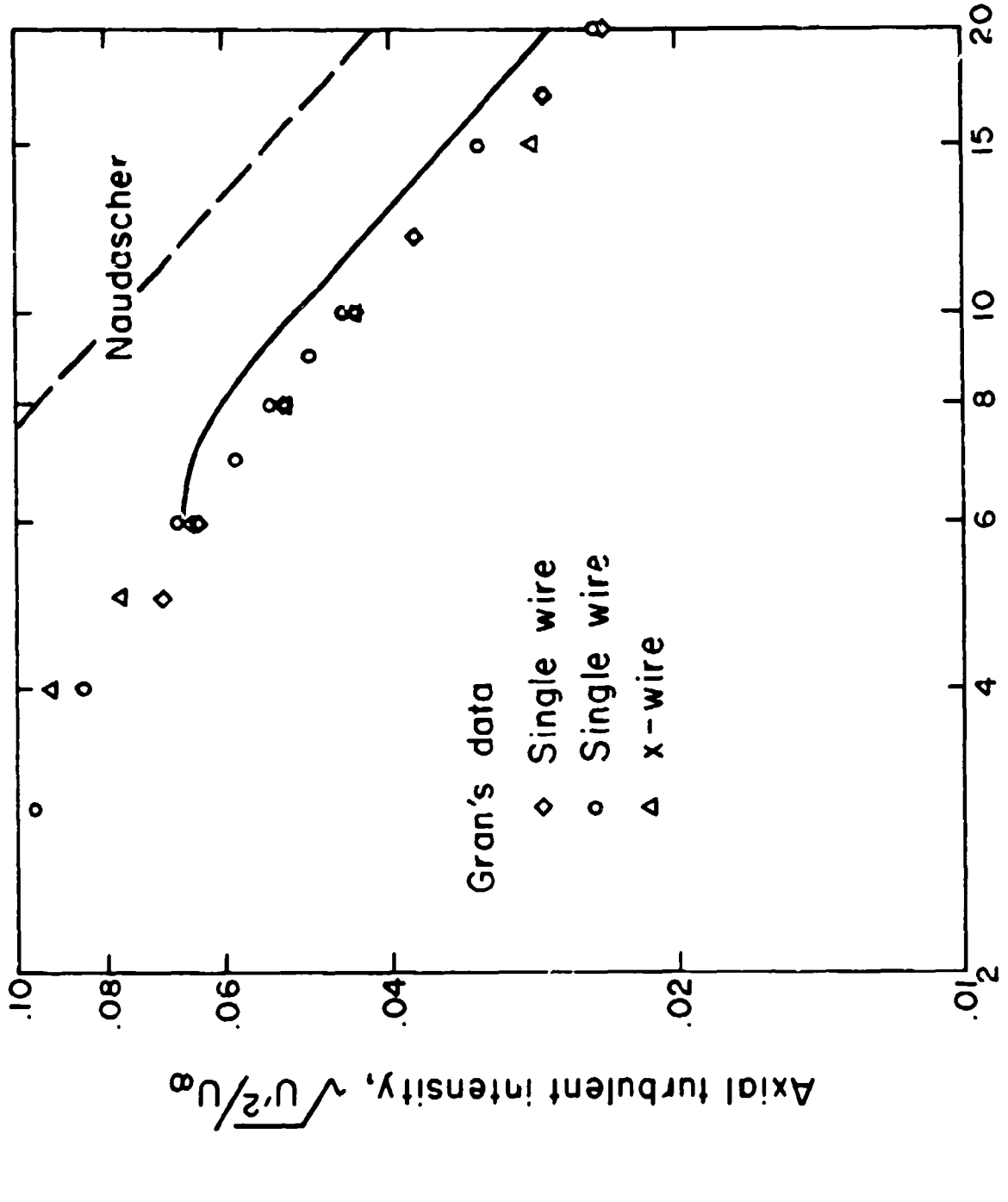

Figure 3.10: Comparison of the prediction of the decay of axial turbulent intensity with the data of Gran (ref. 34) and Naudascher (ref. 25).

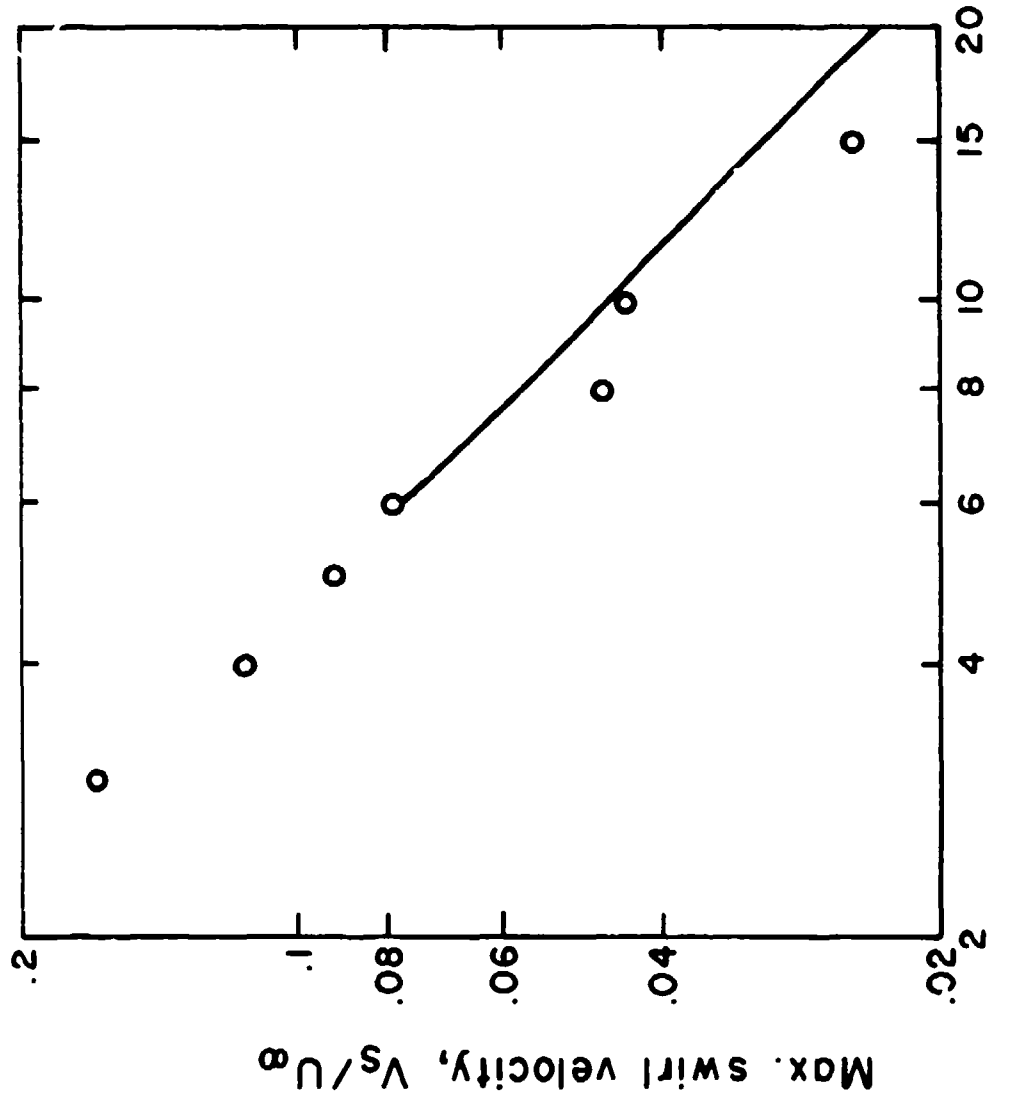

Figure 3.11: Comparison of the prediction of the decay of the swirling velocity with the data of Gran (ref. 34).

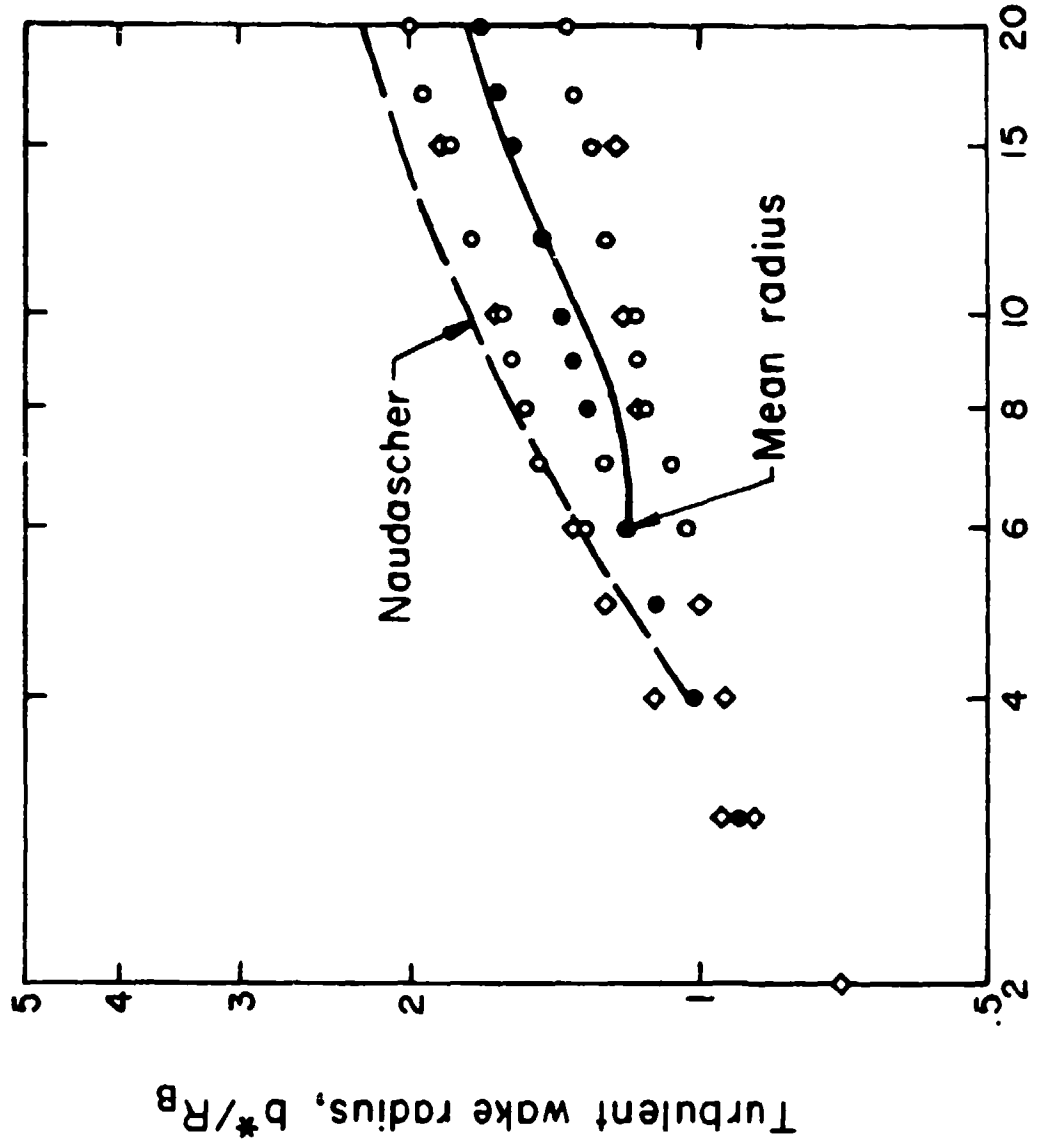

Figure 3.12: Comparison of the prediction of the turbulent wake radius decay with the data of Gran (ref. 34) and Naudascher (ref. 25).

the maximum swirling velocity in fig. 3.11 is quite good; our prediction for the wake radius - in fig. 3.12 - lands well inside the data points. Taken together, this comparison with swirl is much better than our comparison with the swirl data of Schetz.

Recent data from Flow Research, Inc. (ref. 35) dealing with the Fr = 10.2 stratified wake experimental run, also included an examination of the unstratified experiments of Chevray. Our model predictions for this case are given in figs. 3.13 - 3.16. Our comparisons with maximum velocity defect w_D, maximum vertical and horizontal turbulent intensity, and the mean radius r^* are all good. We conclude from these very favorable comparisons in unstratified flows that our turbulence model and gross scale equation are giving us a good picture of the actual physics taking place within these flow configurations. This assurance permits us to investigate problems for which simple comparisons are not possible; certainly much of our stratified flow research falls into this category.

3.b Stratified Flows

Quite favorable comparisons between model predictions and Wu's strong collapse data for a fully mixed wake (ref. 3) and with Hartman and Lewis' linear analysis of a collapsing wake (ref. 5) have been made previously (ref. 15). We include here comparisons with some of Flow Research, Inc.'s data. This has been done in two ways; by making one particular run corresponding to initial wake conditions supplied to us, and by comparing our vertical scale behavior with the behavior of several FRI flow visualization experiments (ref. 36). Since adequate data to compare model predictions with experimental data for the one particular run has not been supplied to us, the initial conditions and the model predictions are presented in the Appendix.

A comparison between model predictions of vertical scale behavior and the behavior of many FRI flow visualization experiments is shown in fig. 3.17. The solid lines are an accumulation

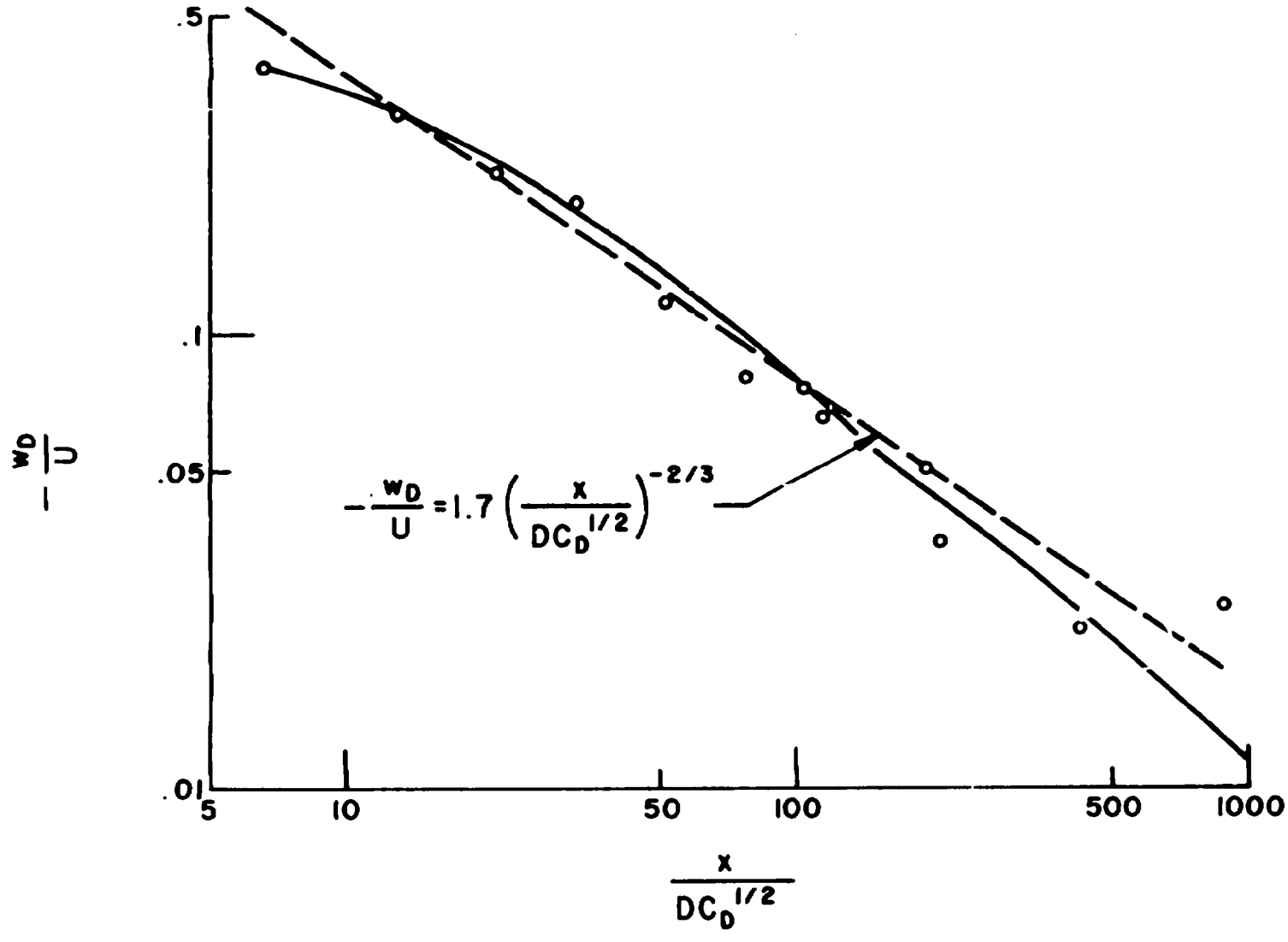

Figure 3.13: Comparison of the prediction of the decay of velocity defect with the drag-body experiments of FRI (ref. 35).

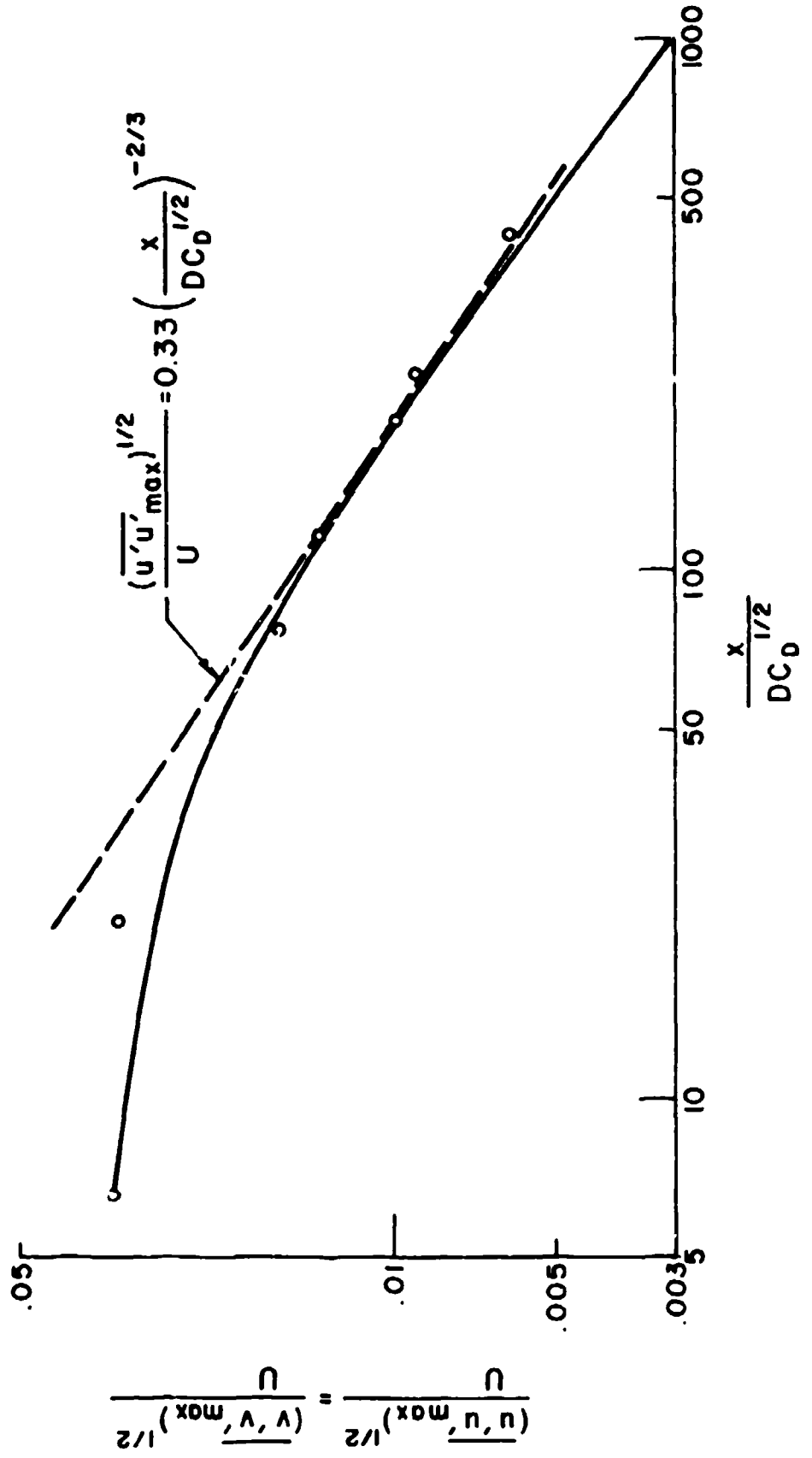

Figure 3.14: Comparison of the prediction of the cross-plane turbulent energy components with the FRI data (ref. 35).

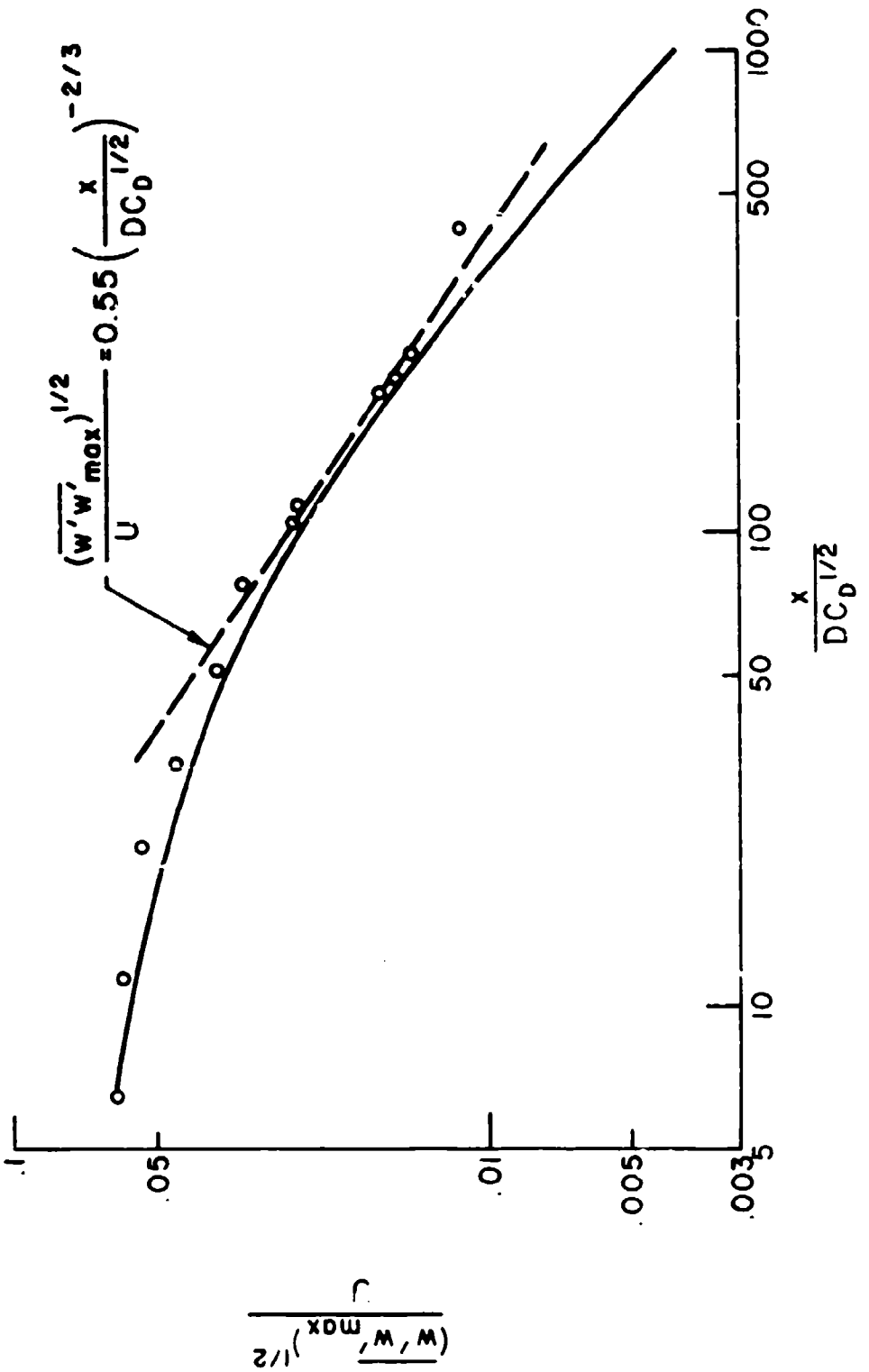

Figure 3.15: Comparison of the prediction of the streaming turbulent energy component with the FRI data (ref. 35).

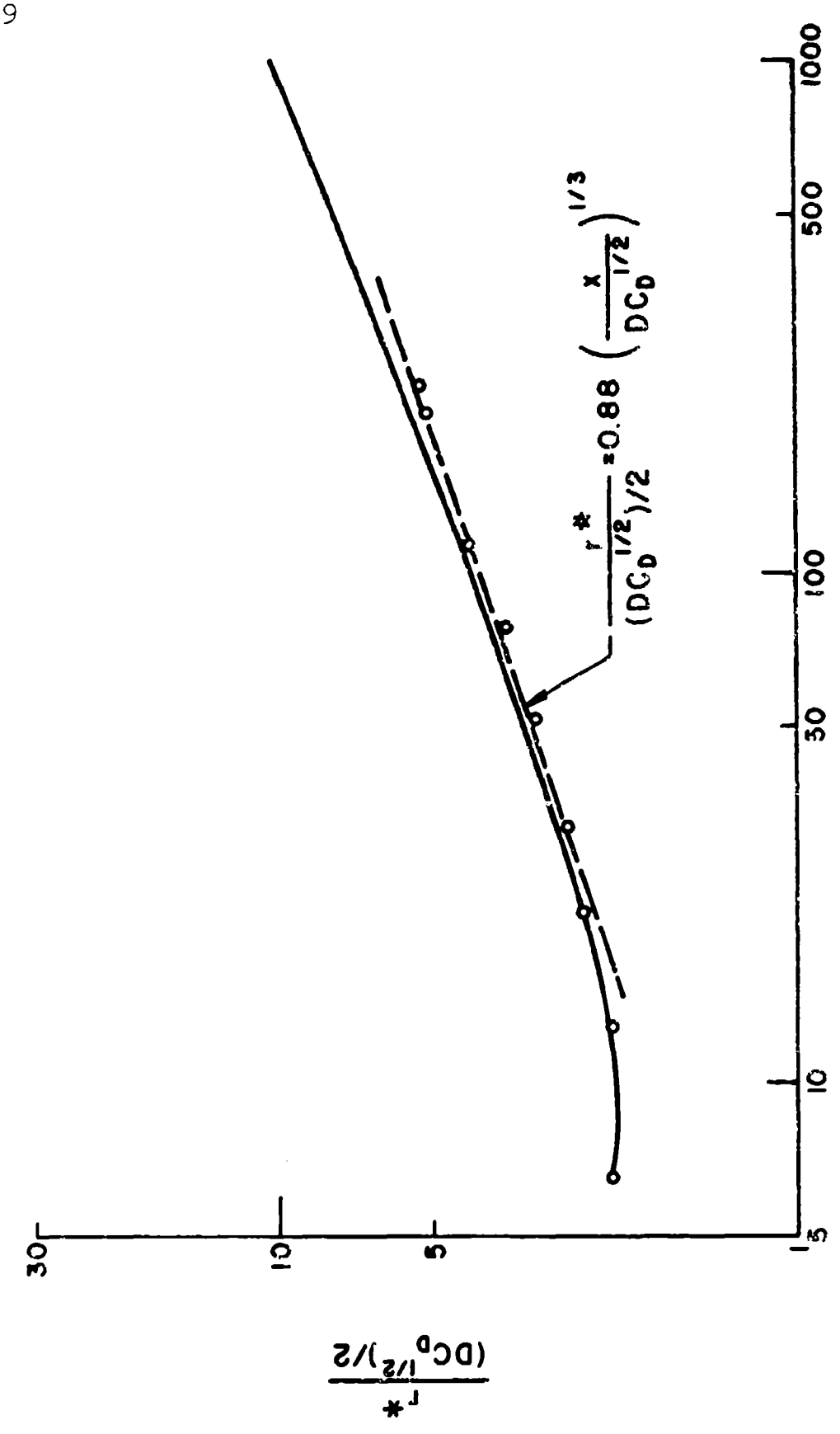

Figure 3.16: Comparison of the prediction of the turbulent wake radius growth with the FRI data (ref. 35).

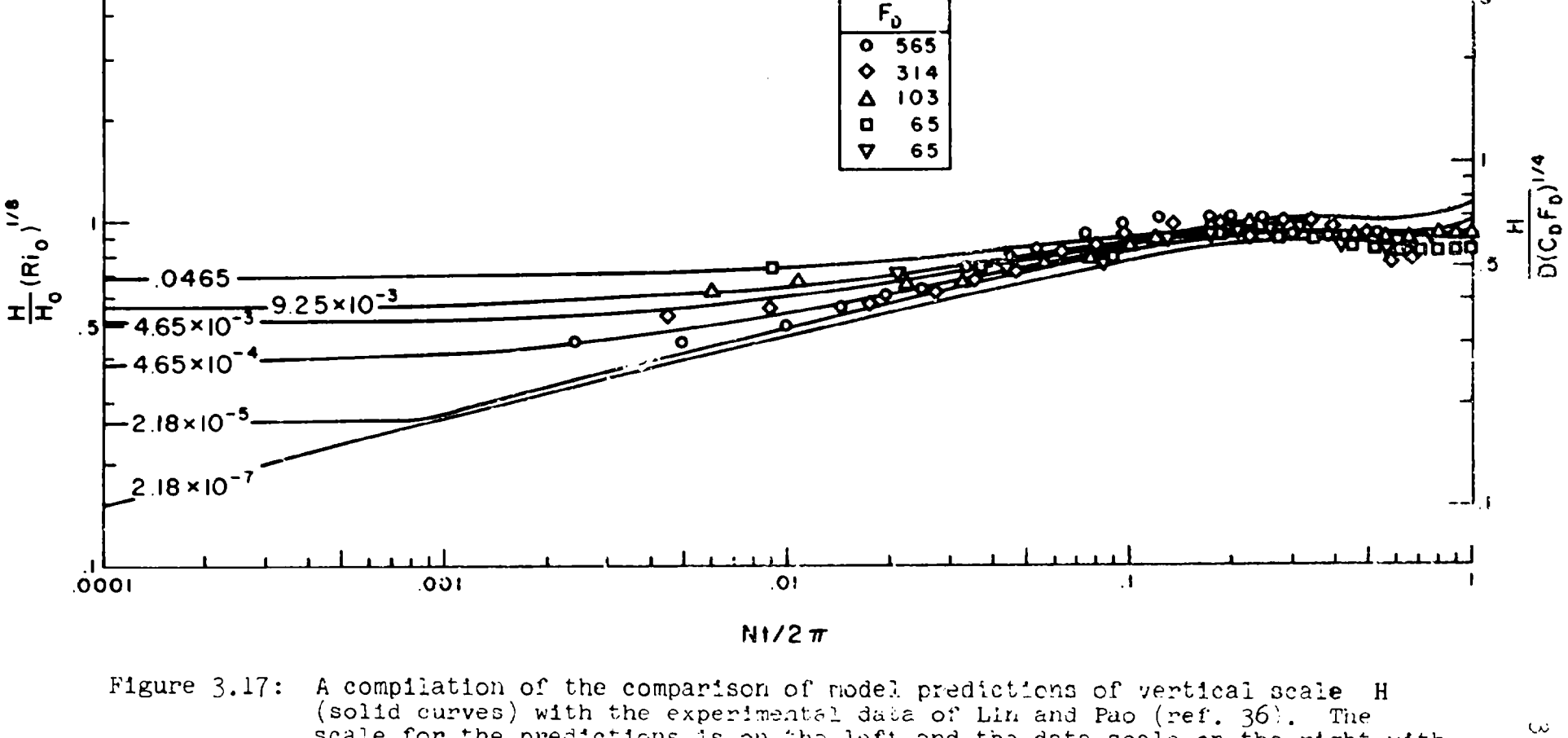

Figure 3.17: A compilation of the comparison of model predictions of vertical scale H (solid curves) with the experimental data of Lin and Pao (ref. 36). The scale for the predictions is on the left and the data scale on the right with the scales matched at the first local maximum of H.

of several A.R.A.P. computer runs, with the data coming from five FRI experimental runs. The scale for the data points is on the right while that for the model predictions is on the left. Since we do not know the exact proportionality between the height as defined by the edge of the turbulence and the height as defined by the dye visualization, nor the proportionality constant between C_D and initial q^2_{max}, an arbitrary adjustment between the two scales has been made to allow the first local maximum in H to coincide for both curves. The qualitative agreement between the predictions and the observations is apparent. The lower Ri_o (or higher Fr) is, the longer the wake follows approximately the $t^{1/4}$ growth law before reaching its local maximum at approximately the same normalized time. This curve will be studied more in the next Section of this report.

Overall, our agreement with stratified and unstratified laboratory flows gives confidence to our solution predictions in flows for which verification will be difficult. We now turn to many of these types of flows, as we study the sensitivity of the wake dynamics to changes in the wake initial conditions.

4. SENSITIVITY OF WAKE DEVELOPMENT TO INITIAL CONDITIONS

One of the principal purposes of the present report is a recording of the sensitivity of wake collapse due to changes in either the initial wake conditions or the ambient fluid. We will investigate changes in the initial turbulence level and macroscale, variations in the initial density profile, changes in axial, vertical and angular momentum, and variations in the ambient density gradient.

4.a Sensitivity to Initial Richardson Number

As seen in eqs. (2.7) to (2.15) there are only three dimensionless parameters in the governing equations, Fr, Re and Pr, and the last two of these disappear as long as $q\Lambda/\nu >> a/b = 20$ according to our turbulent model. The primary variable is then Fr. It is enlightening to consider eqs. (2.7) to (2.15) with q_o used to normalize velocities rather than U. The dimensionless parameter Fr^{-2} is then replaced by the Richardson number Ri_o. Further, if the streamwise direction x is normalized by U/N then q_o/U also disappears from the steady wake equations, i.e., $U\partial/\partial x$ transforms to $(Ri_o)^{1/2}\,\partial/\partial\hat{x}$. It is thus clear that the two parameters q_o/U and Fr may be conveniently combined into the single parameter Ri_o. An initial indication of the sensitivity of wake development to Ri_o was presented in ref. 15. Herein we will add four wake runs at Ri_o values of $Ri_o = 2.18 \times 10^{-7}$, 2.18×10^{-5}, 0.00925 and 0.872. We will discuss their behavior and present contours of important flow quantities at half B.V. intervals.

It should first be stated that almost all runs presented here began six body diameters behind the body with $q^2_{max} = 0.0108$ and $u_{max} = 0.08$. These conditions are approximately those observed in the experiment by Gran (ref. 34). Unless otherwise stated the turbulence and velocity profiles correspond to the Naudascher profiles. The initial density profile is either zero everywhere (generally when v and w are nonzero) or equal to the contrived density profile

$$\hat{\rho}_{L.E.} = \begin{cases} z & ; \ r \leq 1 \\ z \exp[-2(r^2-1)] & ; \ r > 1 \end{cases} \quad (4.1)$$

where $r = r^* = 1$ is the position at which q^2 reaches one-fourth of its maximum value. This "linear-exponential" profile corresponds to a well-mixed initial wake (since the background $\partial\rho_o/\partial z = -1$ under our normalization, for $r < 1$, the perturbation density balances the background).

Figure 4.1 gives the time history of $\hat{\rho}_{max}$ and q_{max} for $Ri_o = 2.18 \times 10^{-7}$. The v and w maximums are below scale. With Ri_o this small, the flow must run to rather large x/D before collapsing. Consequently, v and w never reach large values, q_{max} decays as the $-3/4$ power across the B.V. scale, and $\hat{\rho}_{max}$ increases in response to the wake spreading, then decreases near 0.3 B.V. and begins to oscillate. Because "collapse" takes so long in physical distance downstream, we were able to use a Phase I (q^2, $\hat{\rho}$, u) calculation to 0.01 B.V. before including the two cross-plane velocities v and w, or the necessary iteration for the perturbation pressure π. Figures 4.2 to 4.4 present the contour pictures of q^2, $\hat{\rho}$ and ψ for this wake at 0.5, 1.0, and 1.5 B.V. after generation. The q^2 contours exhibit the spreading of the turbulent wake in the y direction, and its corresponding shrinking in the z direction, to produce an elliptic-like turbulent wake region. The density profiles reflect the mixing of the heavier and lighter fluids leading to collapse, over-collapse, and oscillation about a neutral condition. The streamline patterns for ψ in fig. 4.4 shows the typical streamline generation for a collapsing wake: the definite presence of one vortex at 0.5 B.V.; two vortices at 1 B.V.; and three vortices at 1.5 B.V. In the fringe areas the collapsing wake is generating the next vortex to enter the body of flow. Note that most of the internal wave dynamics is outside the main body of turbulence, yet the scales Λ_y and Λ_z associated with the turbulence are adequate to define the gross scales for the entire collapse region.

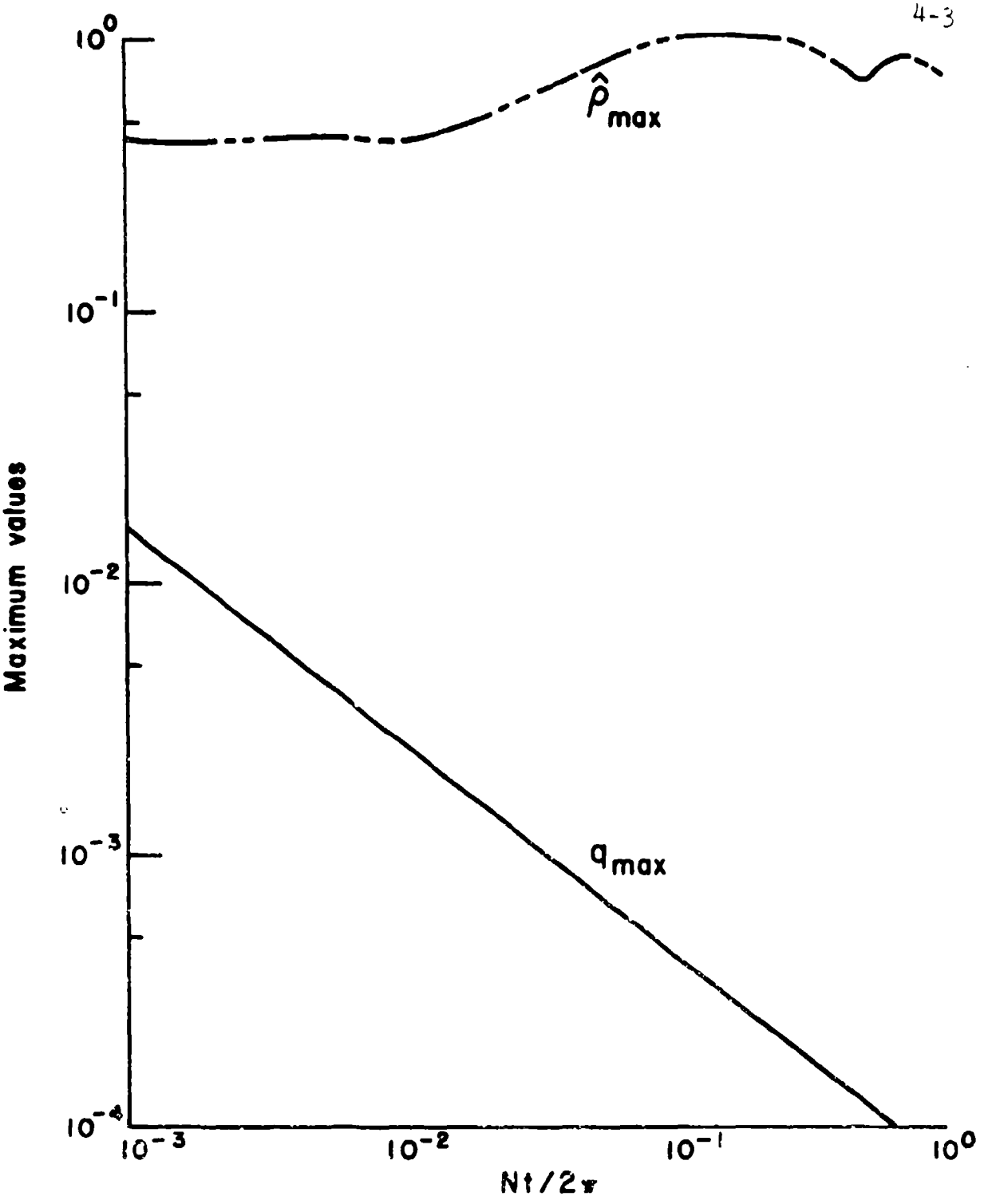

Figure 4.1: The decay of maximum values of q and $\hat{\rho}$ with normalized time (one B.V. occurs at $Nt = 2\pi$) for $Ri_o = 2.18 \times 10^{-7}$, $q^2_{max} = 0.0108$, $\hat{\rho}_{max} = 1$, $u_{max} = 0.080$ (Phase I only) and $v = w = 0$. Time is measured from the point of wake initialization.

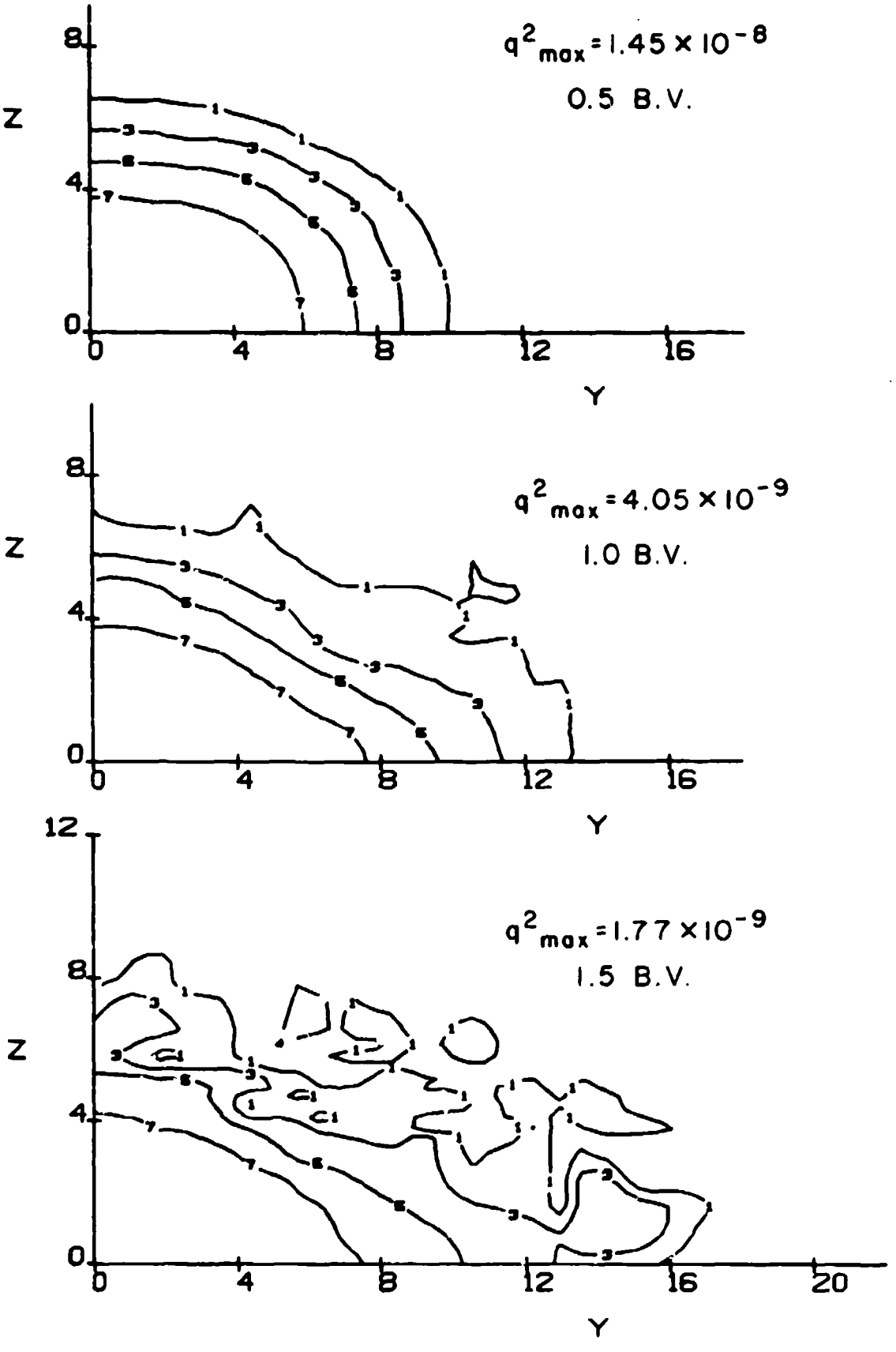

Figure 4.2: Contours of constant q^2 for the conditions of fig. 4.1 . Here B.V. is measured from the point of generation, x/D = 6. The contours are coded so that 1 is +10% of max. value; 2 is -10%; 3 is +30%; 4 is -30%; 5 is +50%; 6 is -50%, 7 is +70%; 8 is -70% of max. value.

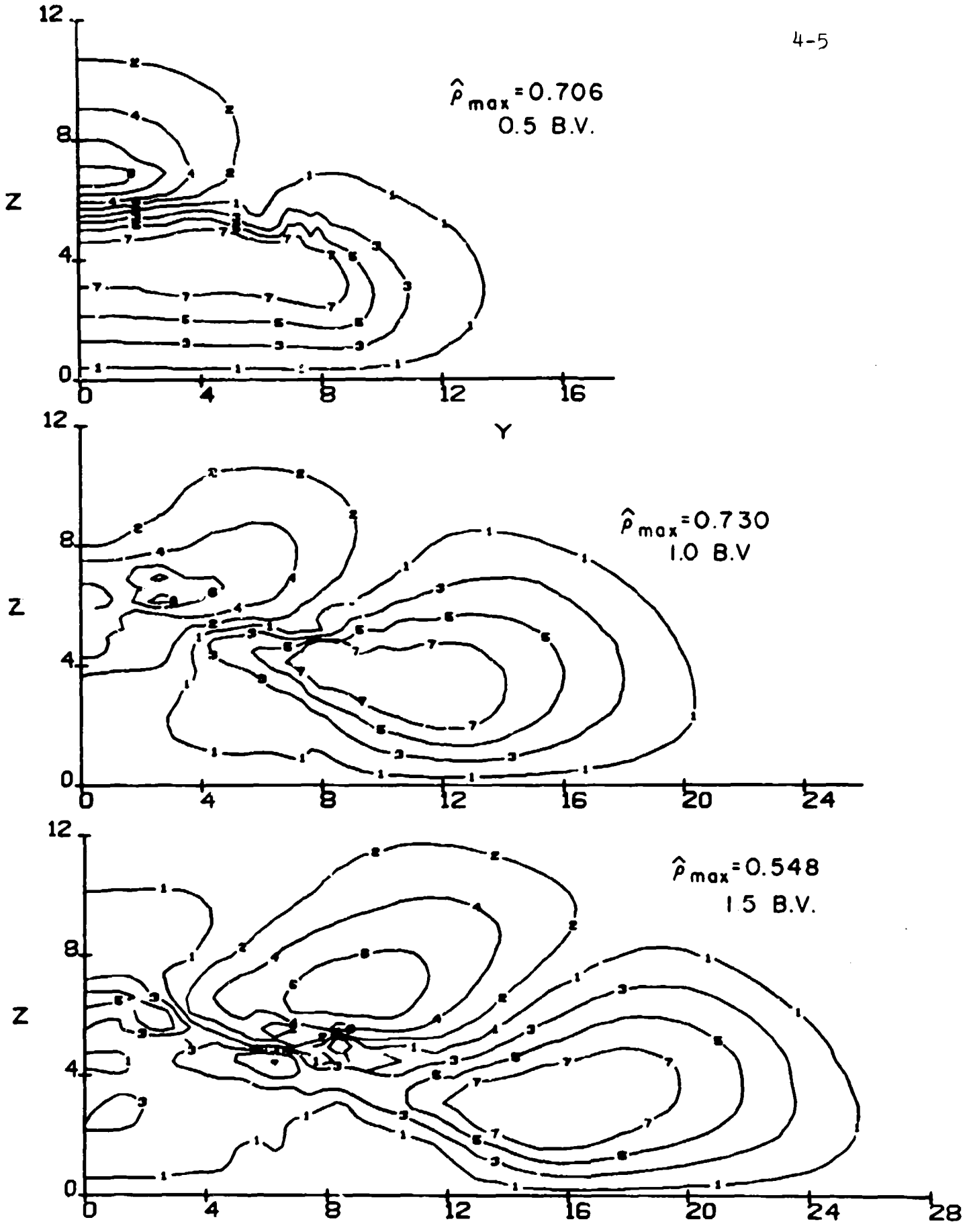

Figure 4.3: Contours of constant $\hat{\rho}$ for the conditions in fig. 4.1 (see fig. 4.2 for contour code).

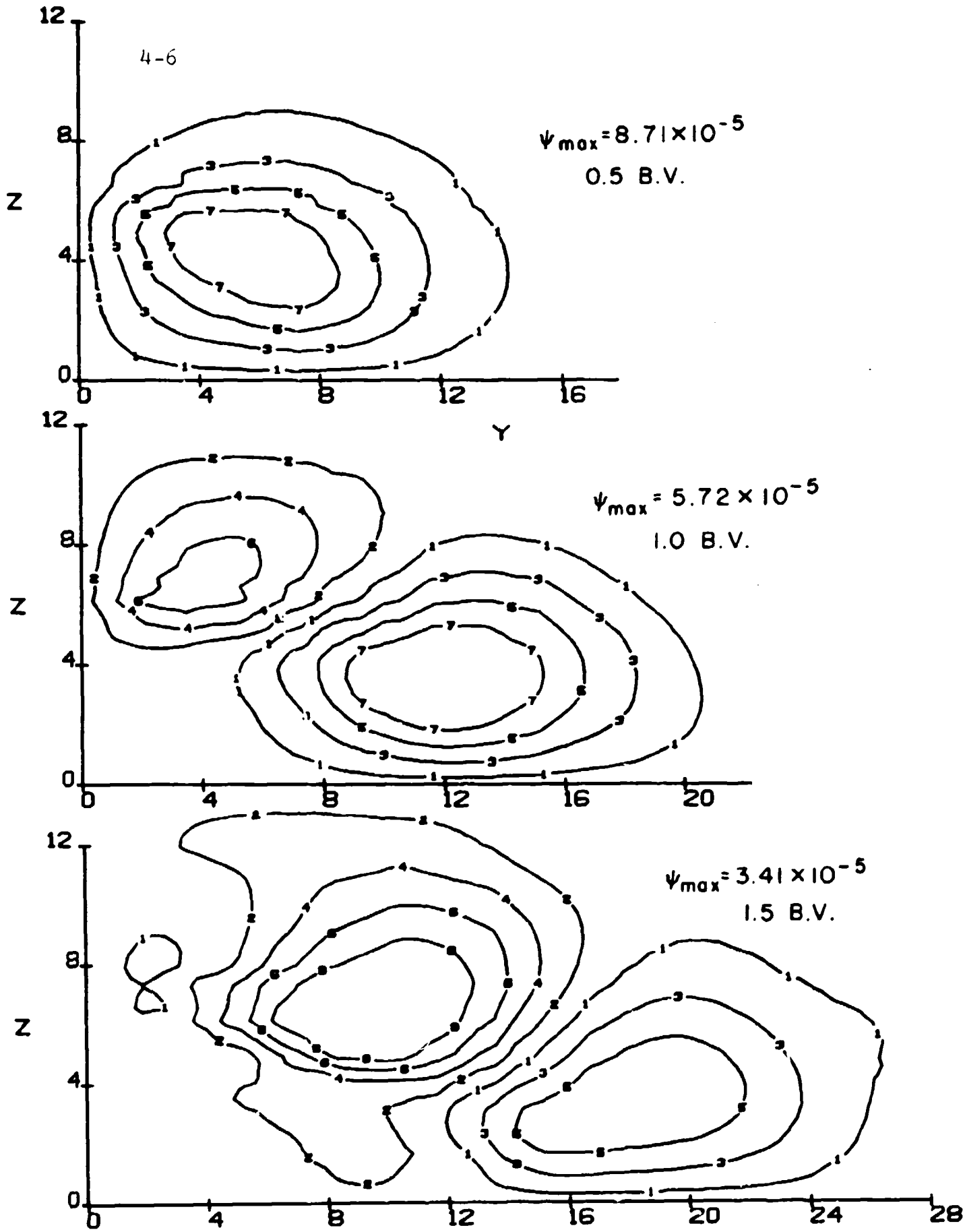

Figure 4.4: Contours of constant ψ for the conditions in fig. 4.1 (see fig. 4.2 for contour code).

If we now increase Ri_o to $Ri_o = 2.18 \times 10^{-5}$, we obtain the wake characteristics shown in figs. 4.5 - 4.8. Note for fig. 4.5 that q_{max} again decays with little regard for internal waves; $\hat{\tau}_{max}$ does some readjusting before building, and then falling near 0.5 B.V.; and v_{max} and w_{max} are present in our scale only after $\approx$ 0.2 B.V. The vertical velocity drops more rapidly than v_{max} as additional wave modes are generated by the collapsing wake. The contours for q^2, $\hat{\tau}$ and ζ all exhibit the same general shapes as for the smaller Richardson number flow in figs. 4.2 - 4.4.

If we now consider an intermediate value of $Ri_o = 0.00925$, we obtain the characteristics shown in figs. 4.9 - 4.13. For comparison purposes later on, we have started the Phase III calculation with u velocity and with $\hat{\tau} = 0$ everywhere. The time history plot in fig. 4.9 again reflects the general behavior found in a wake collapse. The cross-velocities v and w are generally noise until near 0.05 B.V.

If we now jump to the other end of the scale and compute the dynamics for a fast ($Ri_o = 0.872$) collapse, we find the results plotted in figs. 4.14 and 4.15. From the maximum values in fig. 4.14, we see that q_{max} slowly turns to begin its power-law decay (present through the collapses at the three smaller Ri_o values) while $\hat{\tau}_{max}$ is effectively stable and tails off to begin oscillating near 0.5 B.V. Because collapse is so imminent, we used a Phase II calculation throughout. The maximums of v and w appear to grow as the first power until the collapse begins. A cross-over in maximum value occurs, with w_{max} undergoing collapse effects in line with $\hat{\tau}_{max}$ while v_{max} barely feels the effect. The contour plots present much the same picture as for the previous three Ri_o runs. We only show here the plots at 1 B.V. in fig. 4.15.

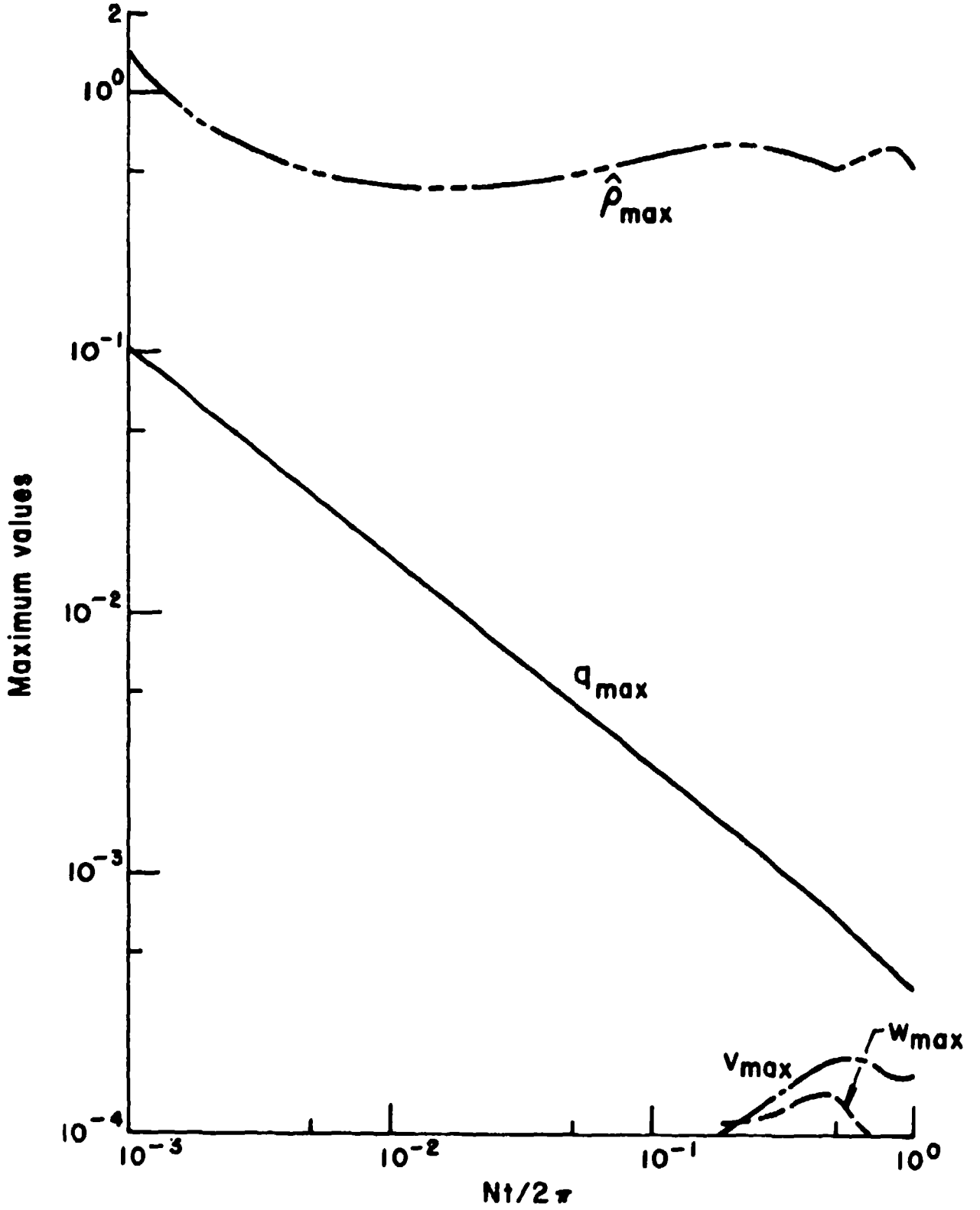

Figure 4.5: The decay of maximum values of q, $\hat{\rho}$, v and w with normalized time for $Ri_o = 2.18 \times 10^{-5}$ and $q^2_{max} = 0.0108$, $\hat{\rho}_{max} = 1$, $u_{max} = 0.080$ (Phase I only), and $v = w = 0$.

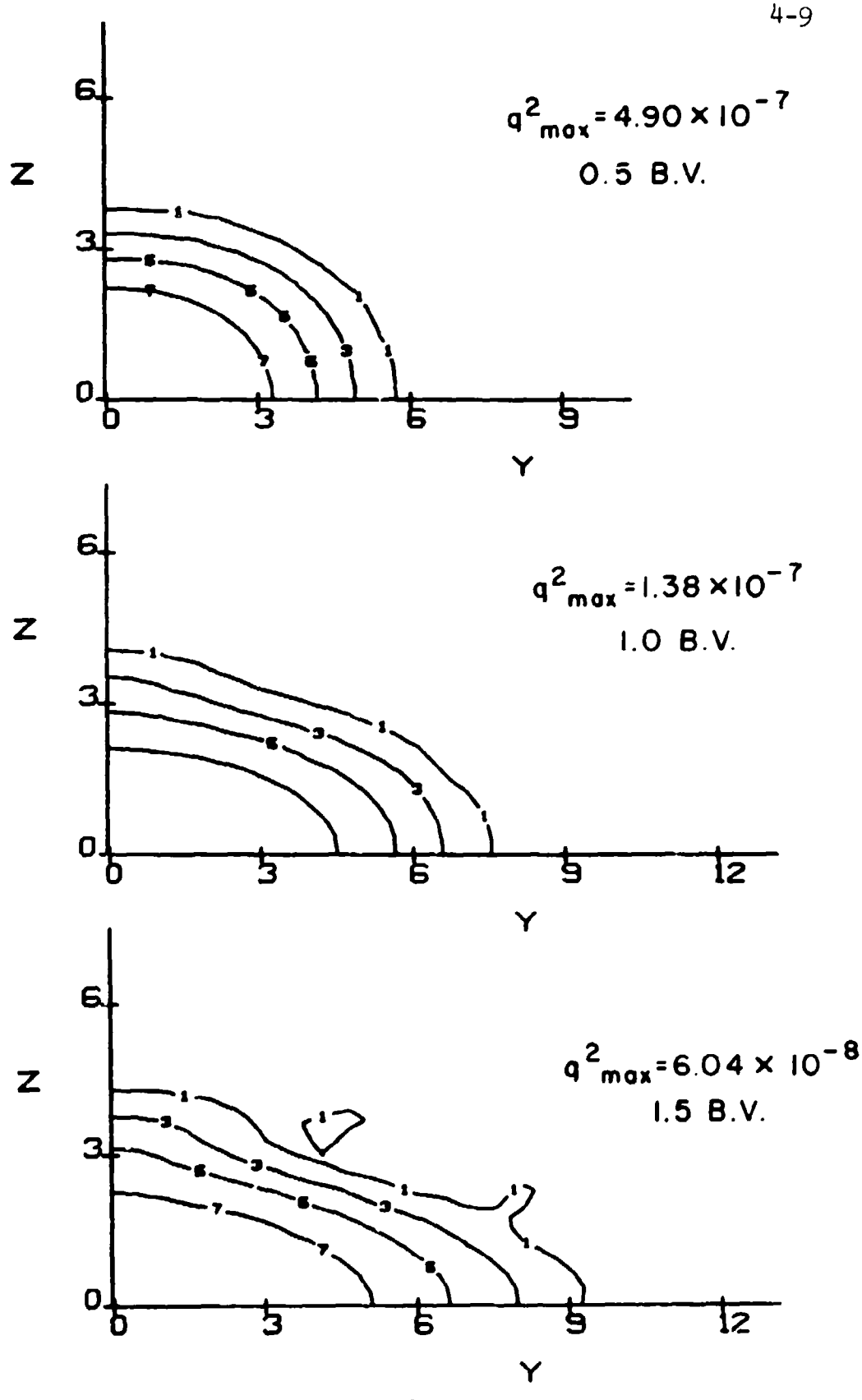

Figure 4.6: Contours of constant q^2 for the conditions of fig. 4.5 (see fig. 4.2 for contour code).

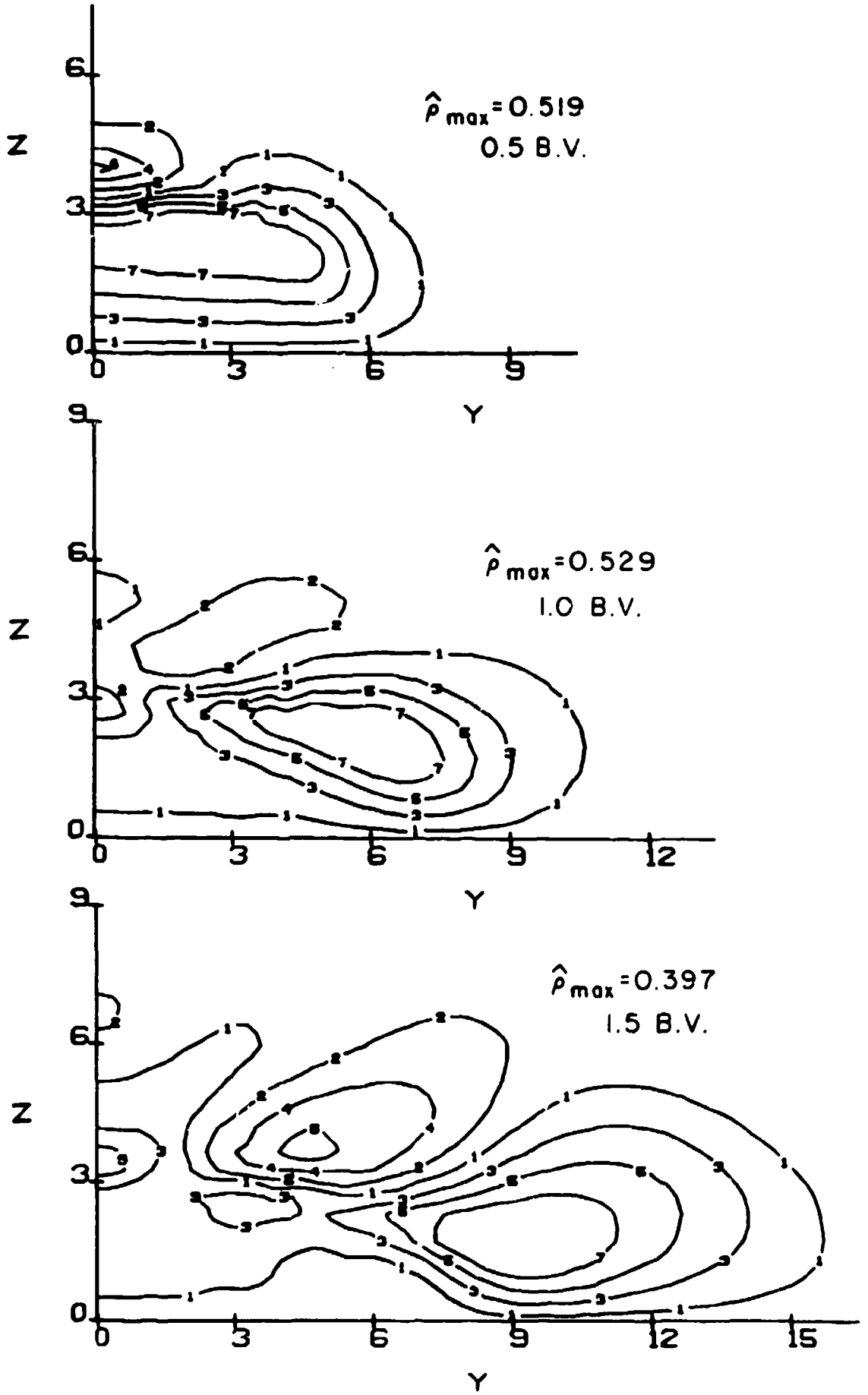

Figure 4.7: Contours of constant $\hat{\rho}$ for the conditions of fig. 4.5 (see fig. 4.2 for contour code).

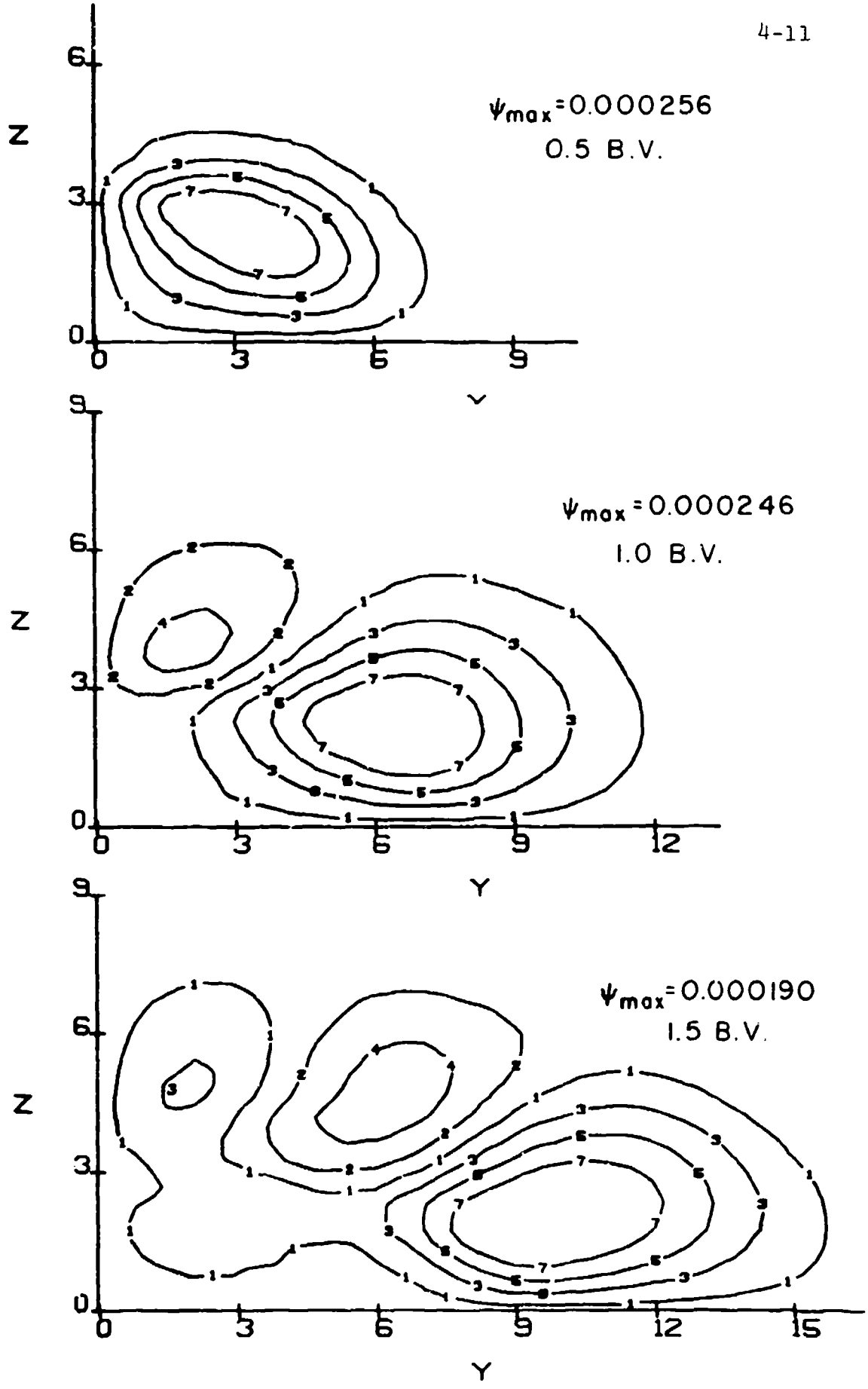

Figure 4.8: Contours of constant ψ for the conditions of fig. 4.5. (see fig. 4.2 for contour code).

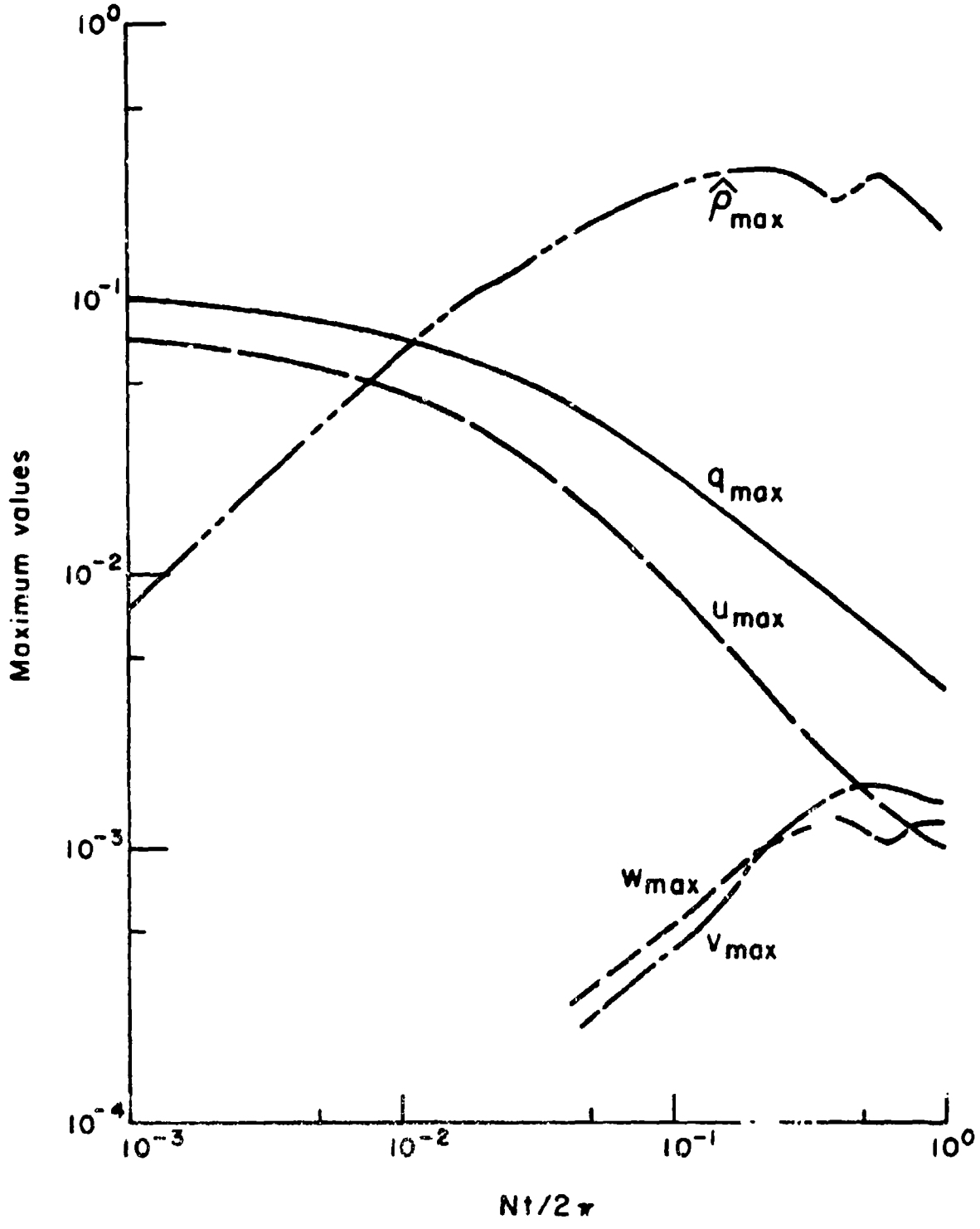

Figure 4.9: The decay of maximum values of q, $\hat{\rho}$, u, v and w with normalized time for $Ri_\rho = 0.00925$ and $q^2_{max} = 0.0108$, $\hat{\rho} = 0$, $u_{max} = 0.080$ and $v = w = 0$.

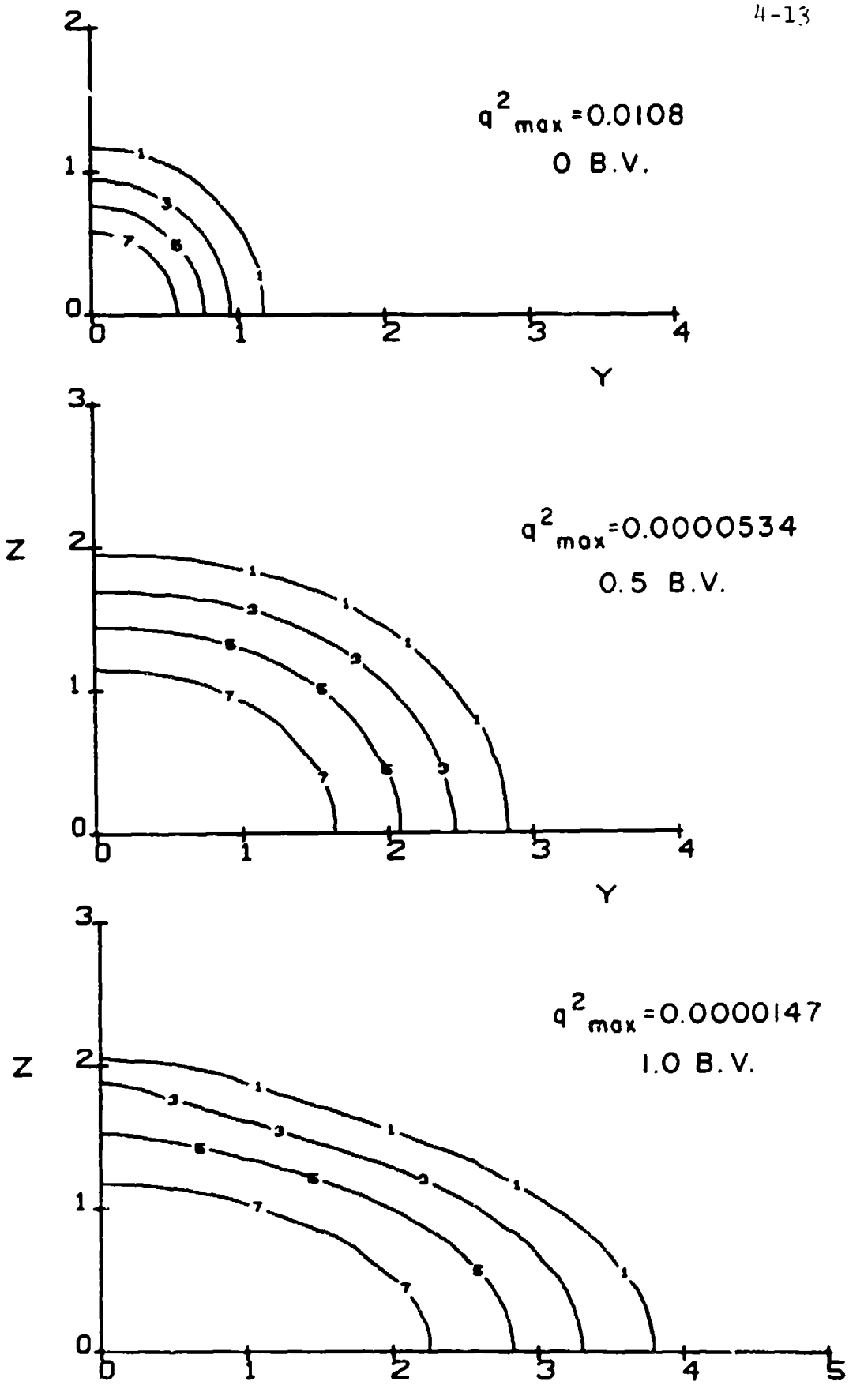

Figure 4.10: Contours of constant q^2 for the conditions of fig. 4.9 (see fig. 4.2 for contour code).

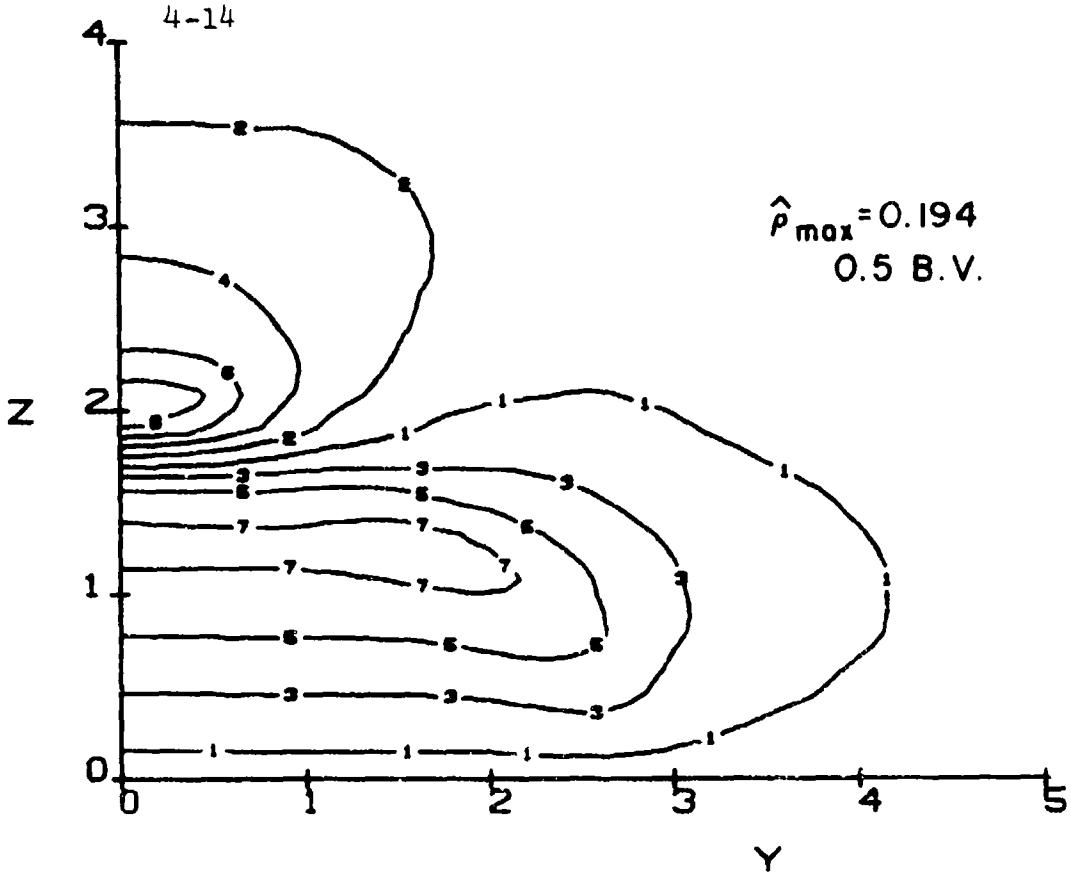

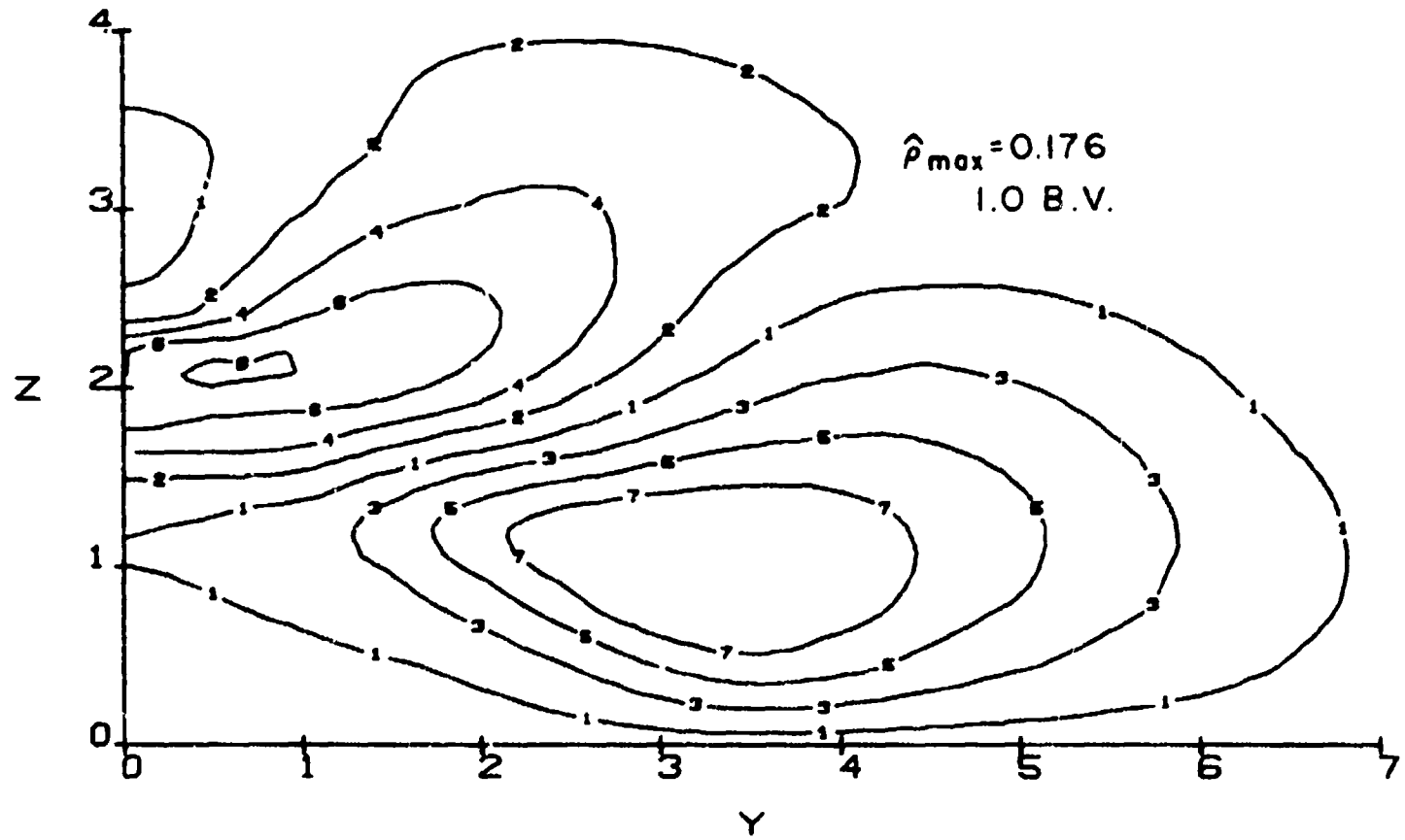

Figure 4.11: Contours of constant $\hat{\rho}$ for the conditions of fig. 4.9 (see fig. 4.2 for contour code).

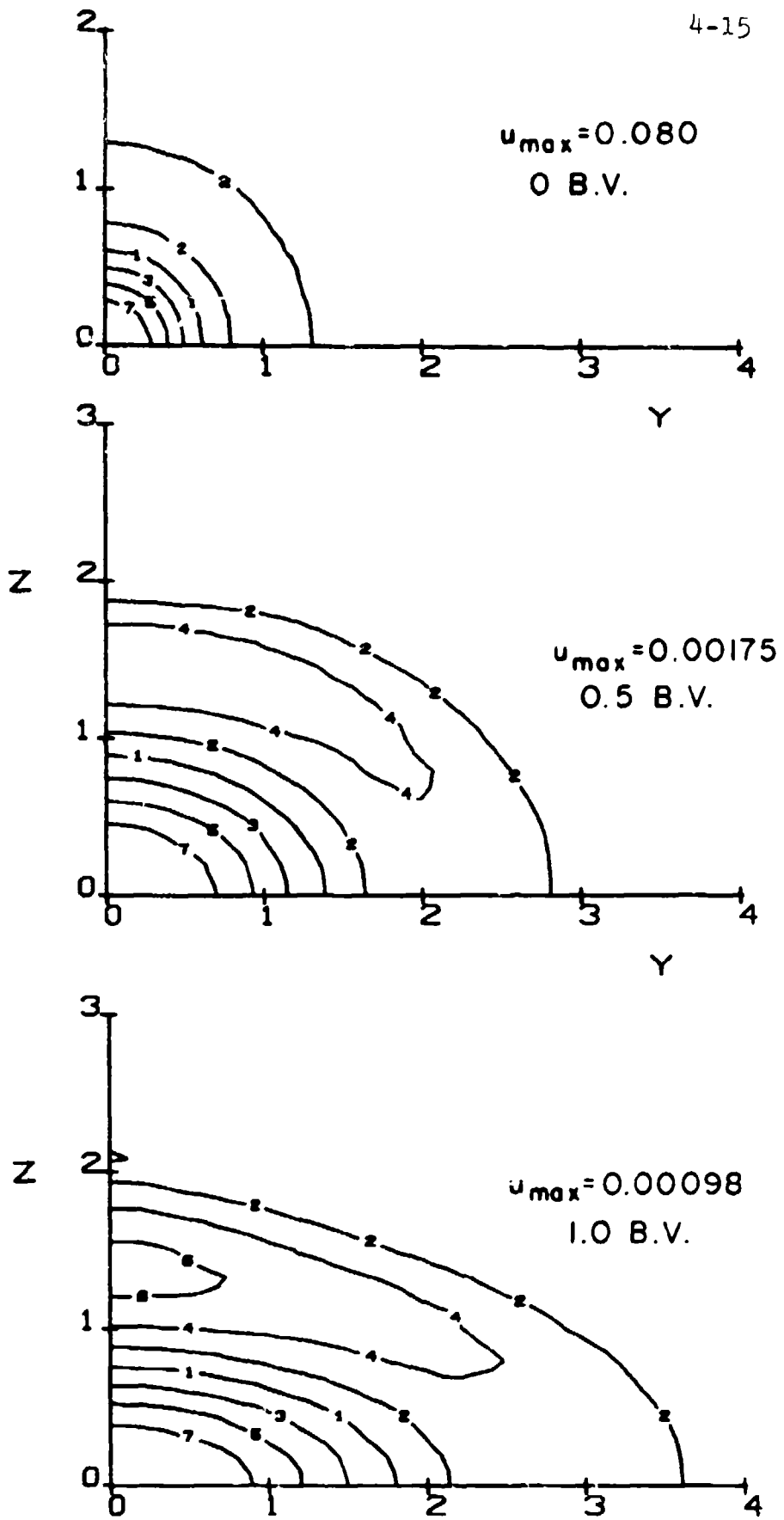

Figure 4.12: Contours of constant u for the conditions of fig. 4.9 (see fig. 4.2 for contour code).

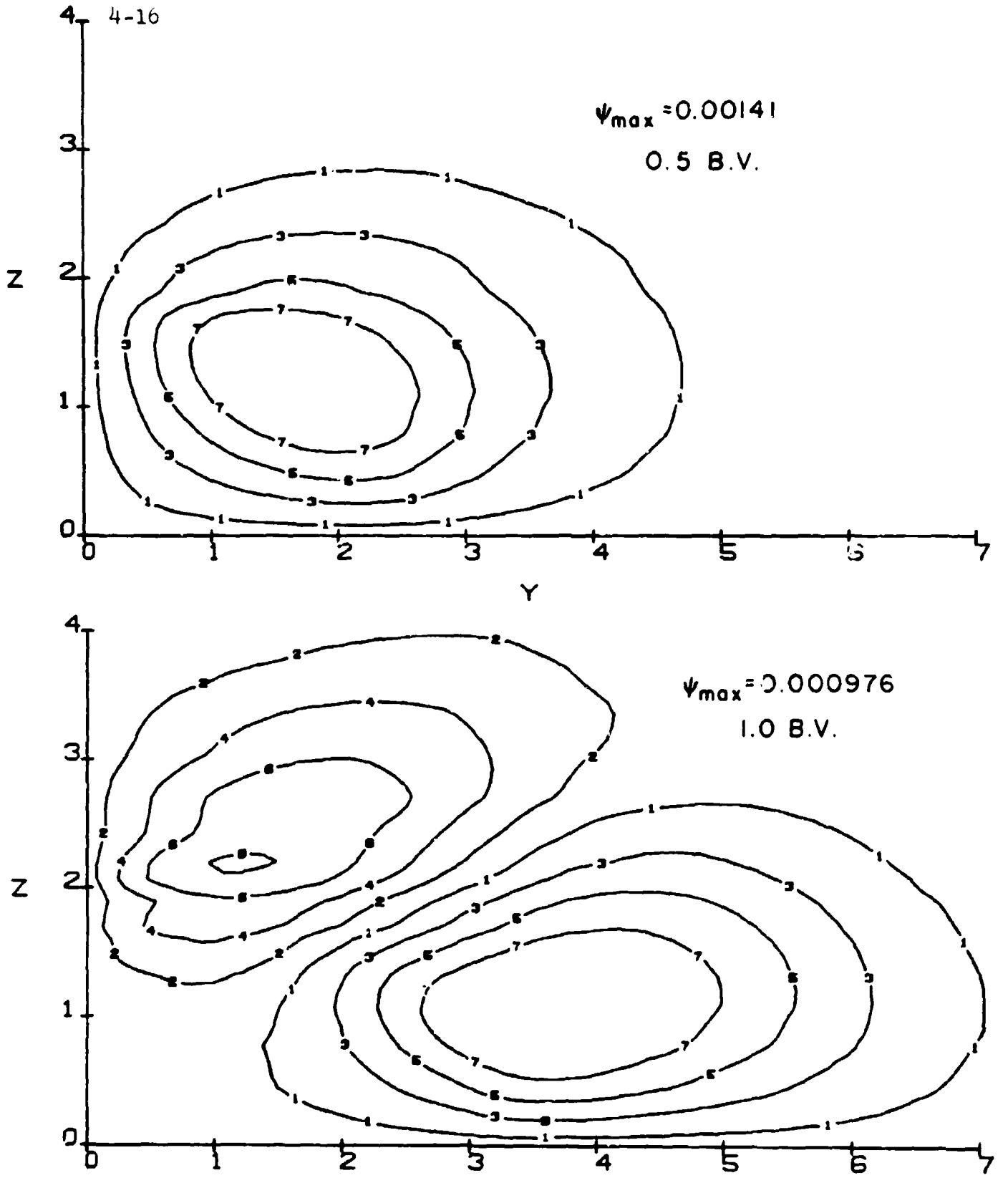

Figure 4.13: Contours of constant ψ for the conditions of fig. 4.9 (see fig. 4.2 for contour code).

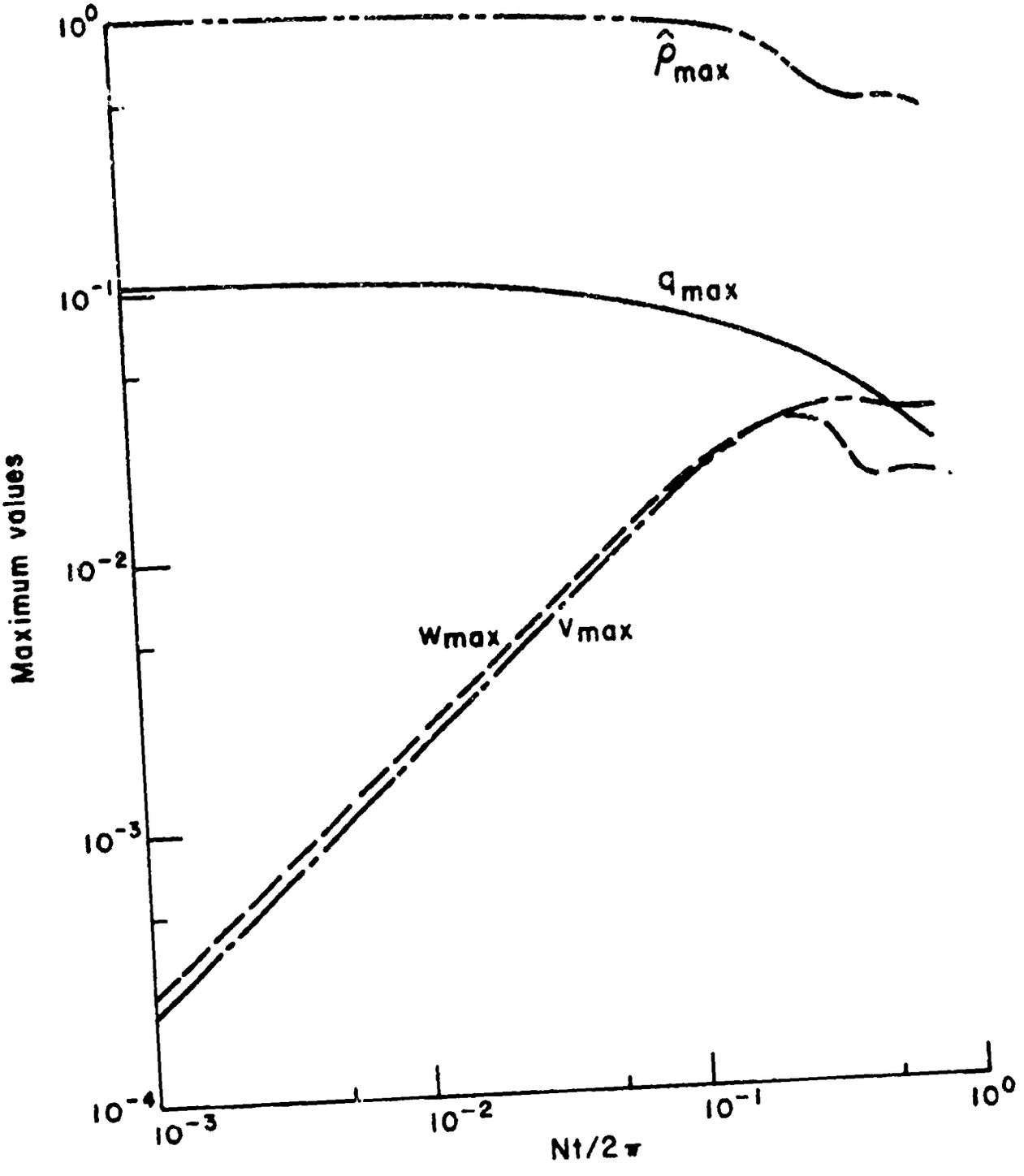

Figure 4.14: The decay of maximum values of q, $\hat{\rho}$, v and w with normalized time for $Ri_o = 0.872$ and $q^2_{max} = 0.0108$, $\hat{\rho}_{max} = 1$, $v = w = 0$.

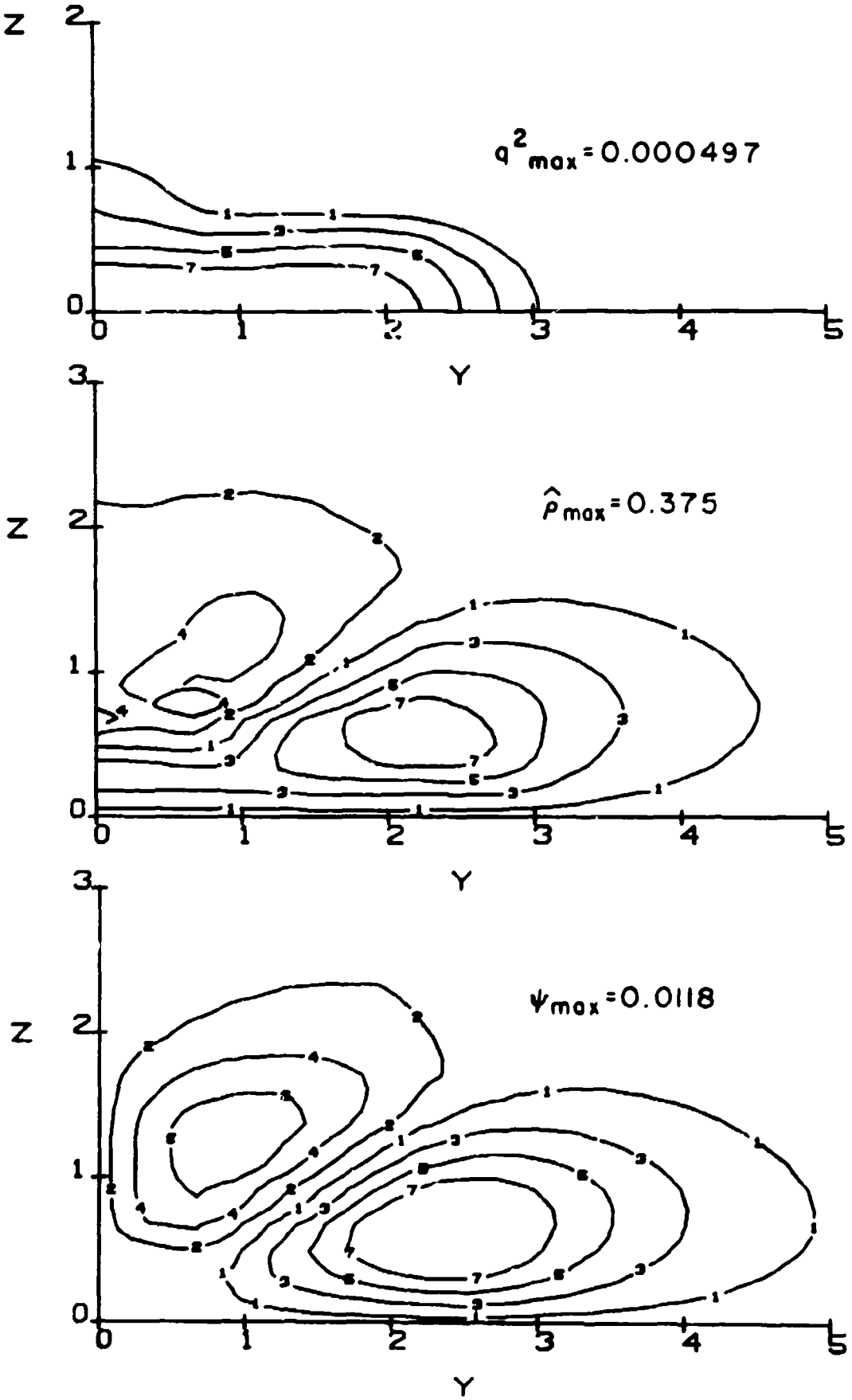

Figure 4.15: Contours of constant q^2 $\hat{\rho}$ and ψ at 1 B.V. for the conditions of fig. 4.14 (see fig. 4.2 for contour code).

Taken together, we see a fairly consistent picture of wake development: q^2 decaying, $\hat{\rho}$ holding fairly constant before falling; and v and w growing with their maximums occurring near 0.5 B.V. The effect of Ri_o can perhaps be best indicated by assembling the plots of the vertical wake height as a function of time for a number of different values of Ri_o. Since the free stream direction x may appropriately be scaled with $Ri_o^{\frac{1}{2}}$ as discussed earlier and since the momentumless wake radius grows approximately as $x^{\frac{1}{4}}$ (ref. 14) it is appropriate to multiply the vertical height H by $Ri_o^{1/8}$ to correlate the different runs. Such a plot is shown in fig. 4.16 with H measured by the point at which q^2 falls to 1/4 its maximum value. For the smallest Ri_o ($= 2.18 \times 10^{-7}$), we see that Λ_z grows with the 1/4th power of time or distance, reaching a broad maximum near 0.3 B.V. For larger values of Ri_o, the curves enter almost horizontally, and then turn to attempt the quarter-power law before reaching a maximum at approximately the same normalized time. For the largest values of Ri_o, the growth phase of wake development is completely missing with the reduction in height coming earlier and being more pronounced.

In fig. 4.16 time is measured from the time of wake initialization. In order to relate this to time measured from generation it would be necessary to add an incremental time $N\Delta t = (x/r_1)(q_{max_1}/U)(Ri_o)^{\frac{1}{2}}$ which for assumed conditions of $r_1 = 1/2$ and $q_{max_1}/U = 0.104$ at 6 diameters behind the body would give $N\Delta t = 1.25(Ri_o)^{\frac{1}{2}}$. The horizontal portion of the curves at early times is caused by the coordinate stretching inherent in the normalization and the logarithmic scale.

The qualitative behavior exhibited in fig. 4.16 agrees very well with experimental observations as seen in fig. 3.17.

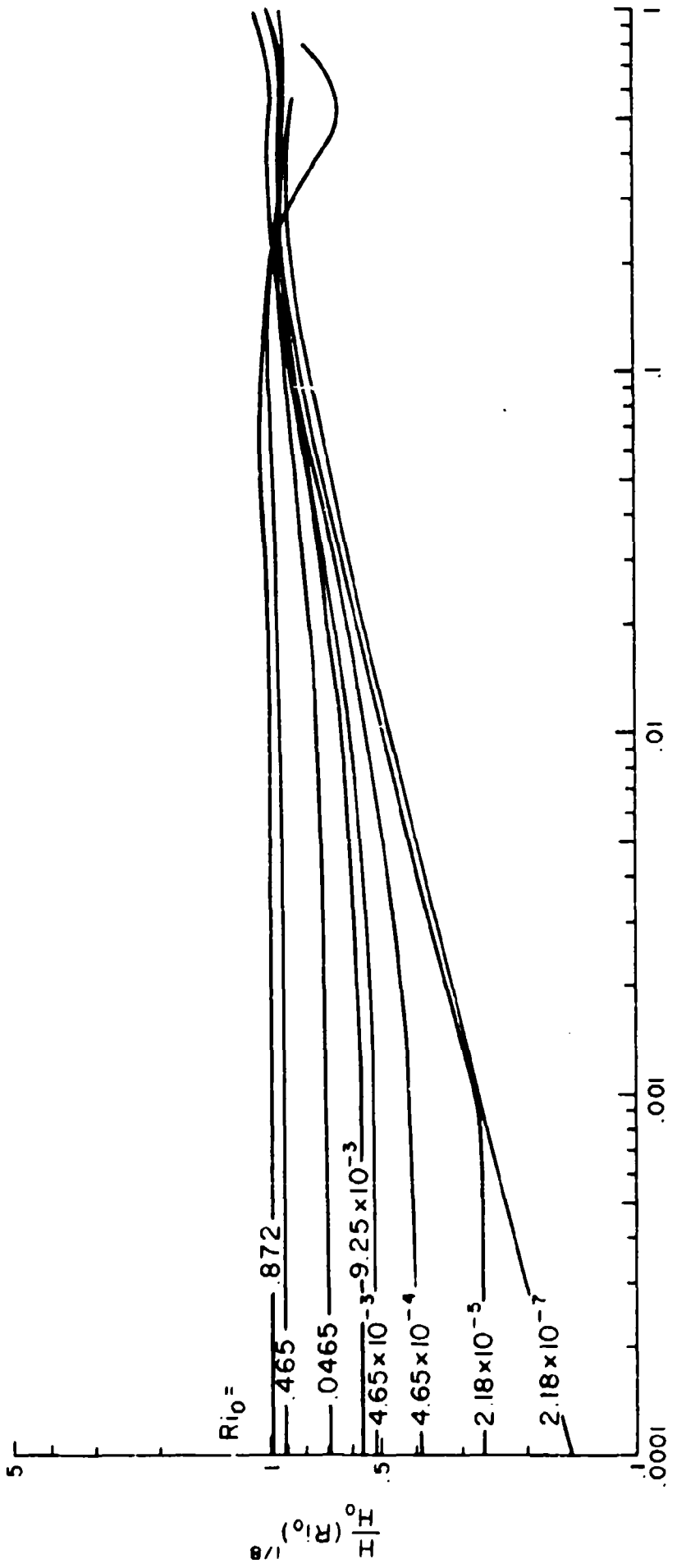

Figure 4.16: A compilation of model predictions of vertical scale height H $(= r_z^*)$ for various values of Ri_o.

4.b Sensitivity to Initial Density Distribution

Figures 4.14 and 4.15 were begun with our linear-exponential form of the initial density profile, eq. (4.1). We may also investigate the sensitivity of wake development to changing this initial density condition. If we begin with no perturbation density anywhere with $Ri_o = 0.872$, we obtain the decay characteristics shown in fig. 4.17 and the contour plots for q^2, $\hat{\rho}$ and ψ given in fig. 4.18. It can be seen by comparison with the maximum values of fig. 4.14 that the q_{max} profile has hardly changed. This would suggest that the initial density does not change the q^2 decay, even through collapse. Of course, $\hat{\rho}$ begins from zero value, and grows at a rate comparable to the first power. But $\hat{\rho}$ never gets to as large a value as beginning with nonzero $\hat{\rho}$ due to the relatively short time available prior to collapse. Since the magnitude of $\hat{\rho}$ drives the cross-plane velocities, v_{max} and w_{max} do not reach as large values as before. Also note that the maximum value of w_{max} occurs at a slightly later time.

The effect of initial density profile on the subsequent wake development is reduced as Ri_o decreases. For values of $Ri_o < 0.01$ there is no discernible effect of initial density profile on wake geometry. In the other limit as Ri_o is increased (corresponding to decreasing Fr for a specified body), the initial conditions increasingly dominate the wake. Below some threshold value of Fr we expect any internal waves generated by the wake to be dominated by waves generated directly by the body so the behavior of the wake in this regime is relatively unimportant for far-field calculations. To demonstrate what may happen on the border of such a low Fr regime we have made a calculation in which the initial wake profiles are dominated by the body wave to such an extent as to create a negative initial density perturbation (i.e., the wake has negative potential energy) equal to half the value of $\hat{\rho}_{L.E.}$ across the profile. These results are shown in figs. 4.19 and 4.20.

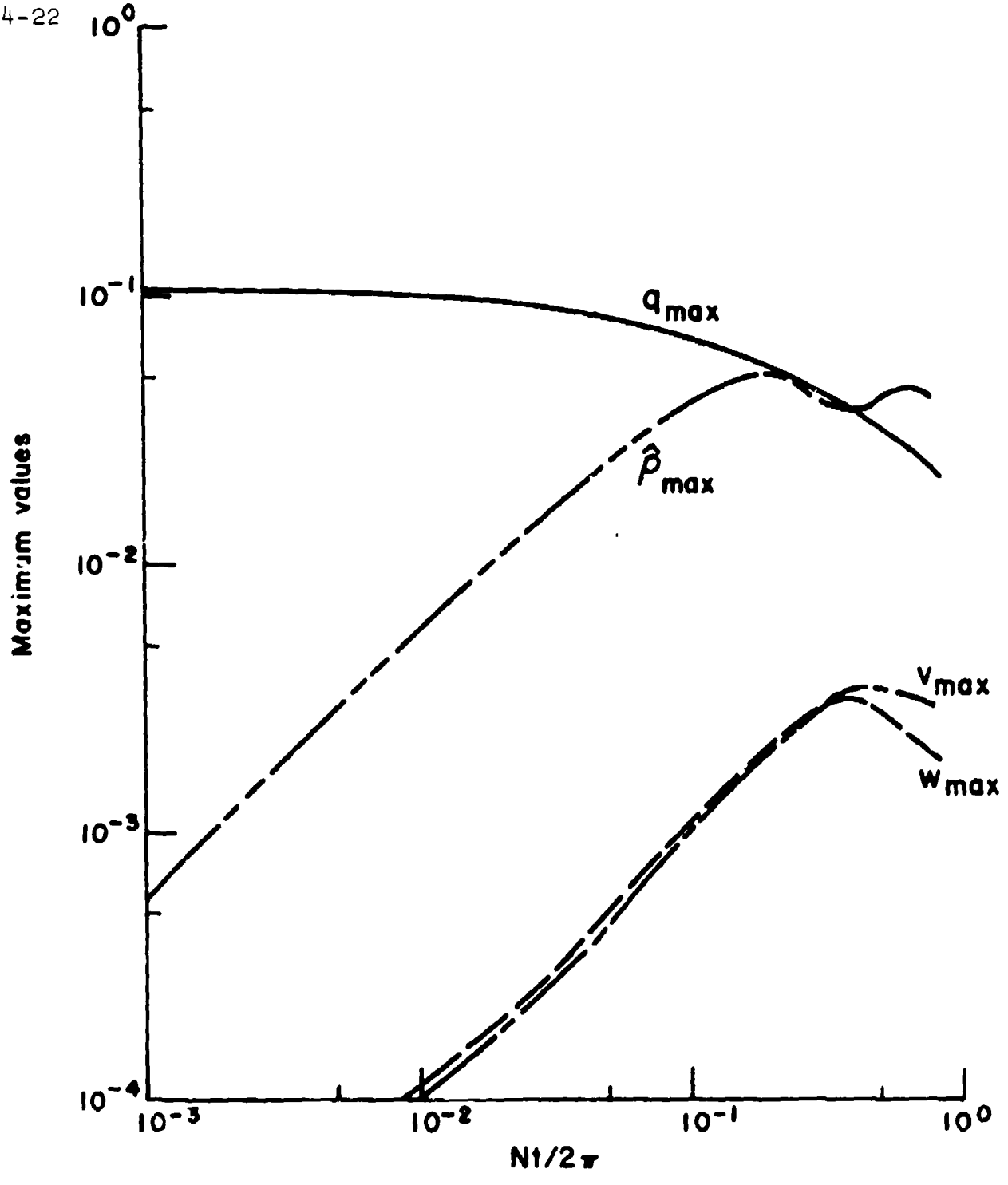

Figure 4.17: The decay of maximum values of q, $\hat{\rho}$, v and w with normalized time for $Ri_o = 0.872$ and $q^2_{max} = 0.0108$, $\hat{\rho} = 0$, $v = w = 0$.

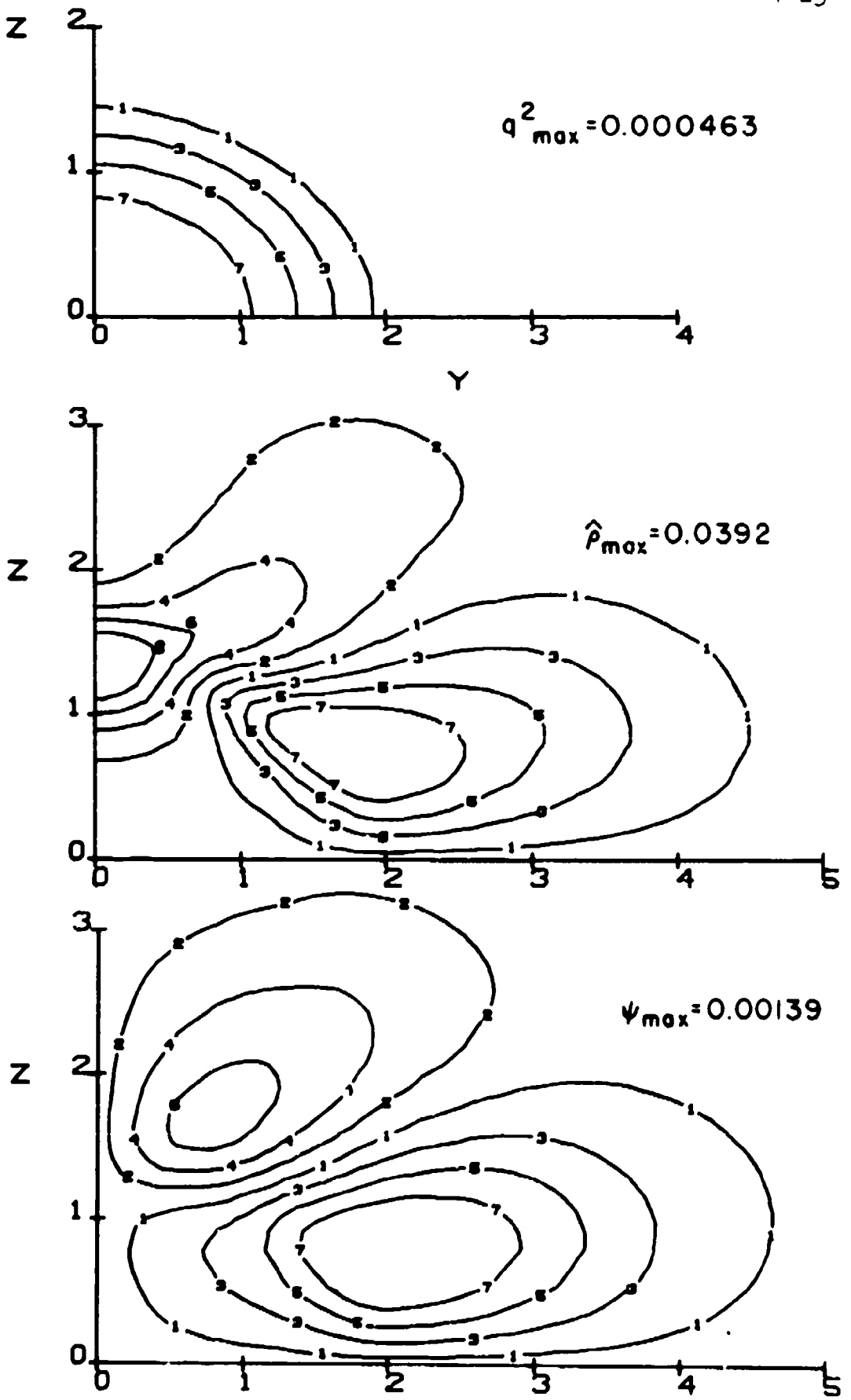

Figure 4.18: Contours of constant q^2, $\hat{\rho}$ and ψ at 1 E.V. for the conditions of fig. 4.17 (see fig. 4.2 for contour code).

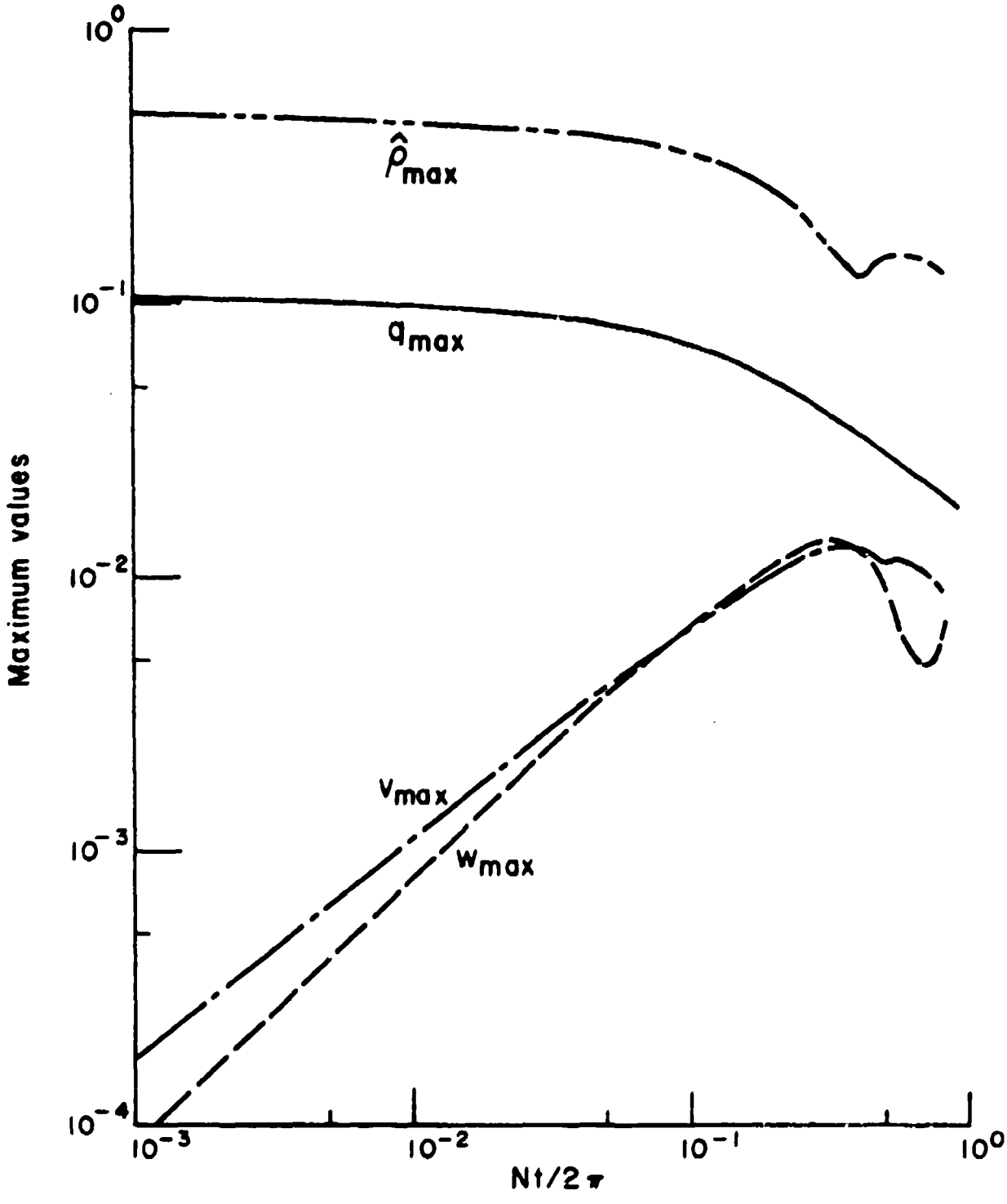

Figure 4.19: The decay of maximum values of q, $\hat{\rho}$, v and w with normalized time for $Ri_o = 0.872$ and $q^2_{max} = 0.0108$, $\hat{\rho}_{max} = 0.5$, $v = w = 0$.

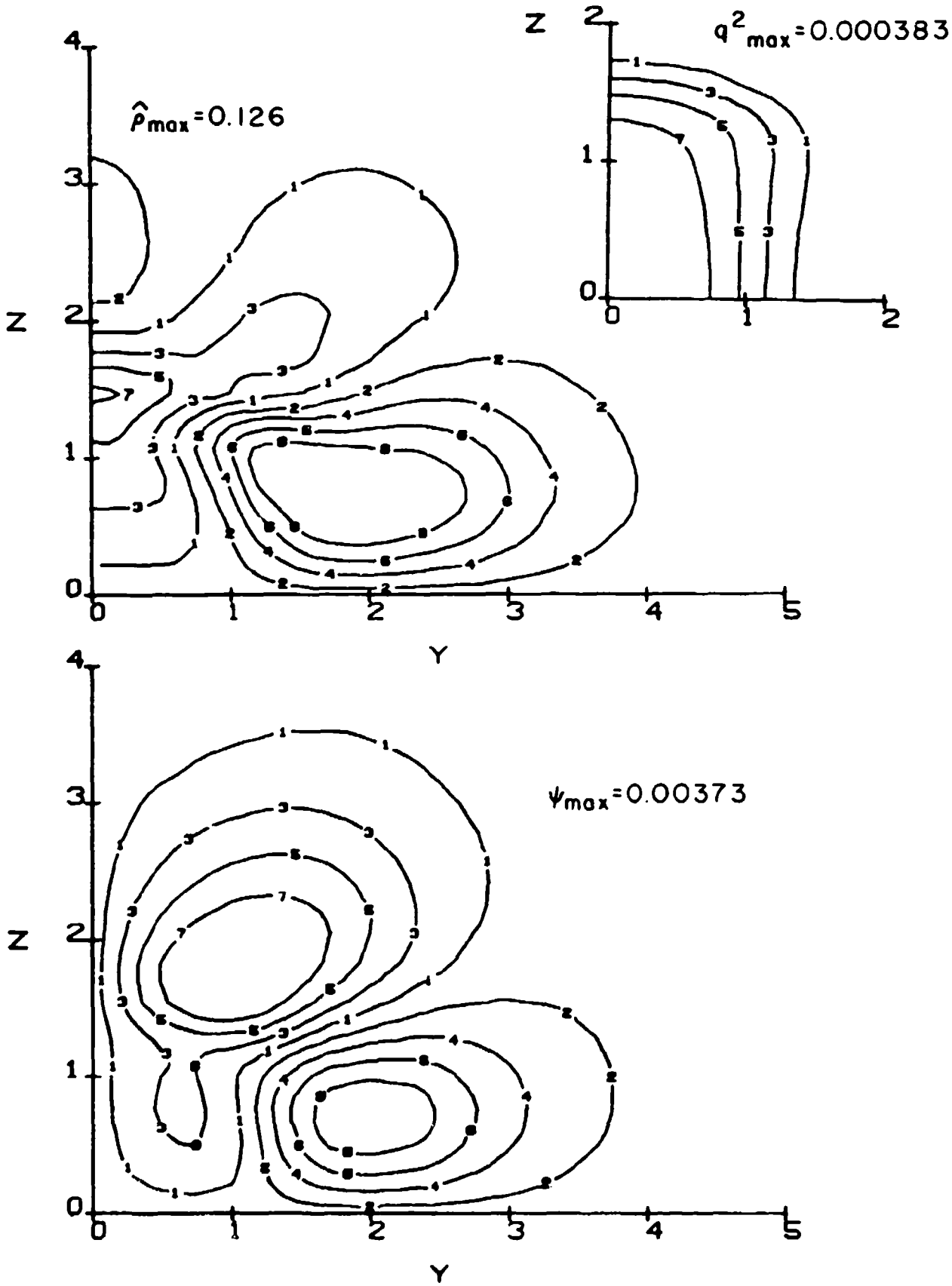

Figure 4.20: Contours of constant q^2, $\hat{\rho}$ and ψ at 1 B.V. for the conditions of fig. 4.19. (see fig. 4.2 for contour code).

Again we see that q_{max} is unchanged; $\hat{\rho}_{max}$ is at a different level, but its decay behavior is much the same as before; while v and w grow and collapse in a range of values between $\hat{\rho}_i = 0$ and $\hat{\rho}_i = \hat{\rho}_{L.E.}$ For this last case v_{max} and w_{max} in fact have slightly different growth rates, in very similar manner to their growth in the run in the Appendix generated from the initial conditions supplied by the FRI data. Here v_{max} grows at a slightly higher rate than w_{max} ; a cross-over in curves occurs; and w shows a strong drop off after the maximum values are reached.

The different behavior of the vertical height of the wake for these three runs are shown in fig. 4.21 by plotting Λ_z versus normalized time. We have also indicated by the dashed line the run made to compare with Appendix A. The slight dipping initially may mean that we have not given a consistent description of the initial profiles to the wake program for this case. The classic picture of a collapsing wake (ref. 1) is not evidenced in any of these runs. A maximum vertical height is reached in each case, but later in all the runs we see Λ_z rebounding and increasing.

4.c Sensitivity to Initial Turbulent Scale

In order to investigate the effect of initial turbulent scale on wake development, it is necessary to use the dynamic scale equation discussed in Section 2. Returning to our axisymmetric program for the full set of equations, we can test the consequences of a variable Λ across the wake profile. This is in fact the reason why we chose to derive and study a dynamic scale equation whose present form is given in eq. (2.21).

For this test we assume that Λ is small near the center of the wake (to simulate turbulence chopped up by the propeller) and growing linearly out to the edge, fig. 4.22. A comparison with our previous initial condition, eq. (2.16) is also given. The very small scale near $r = 0$ causes a sharp reduction in the turbulent

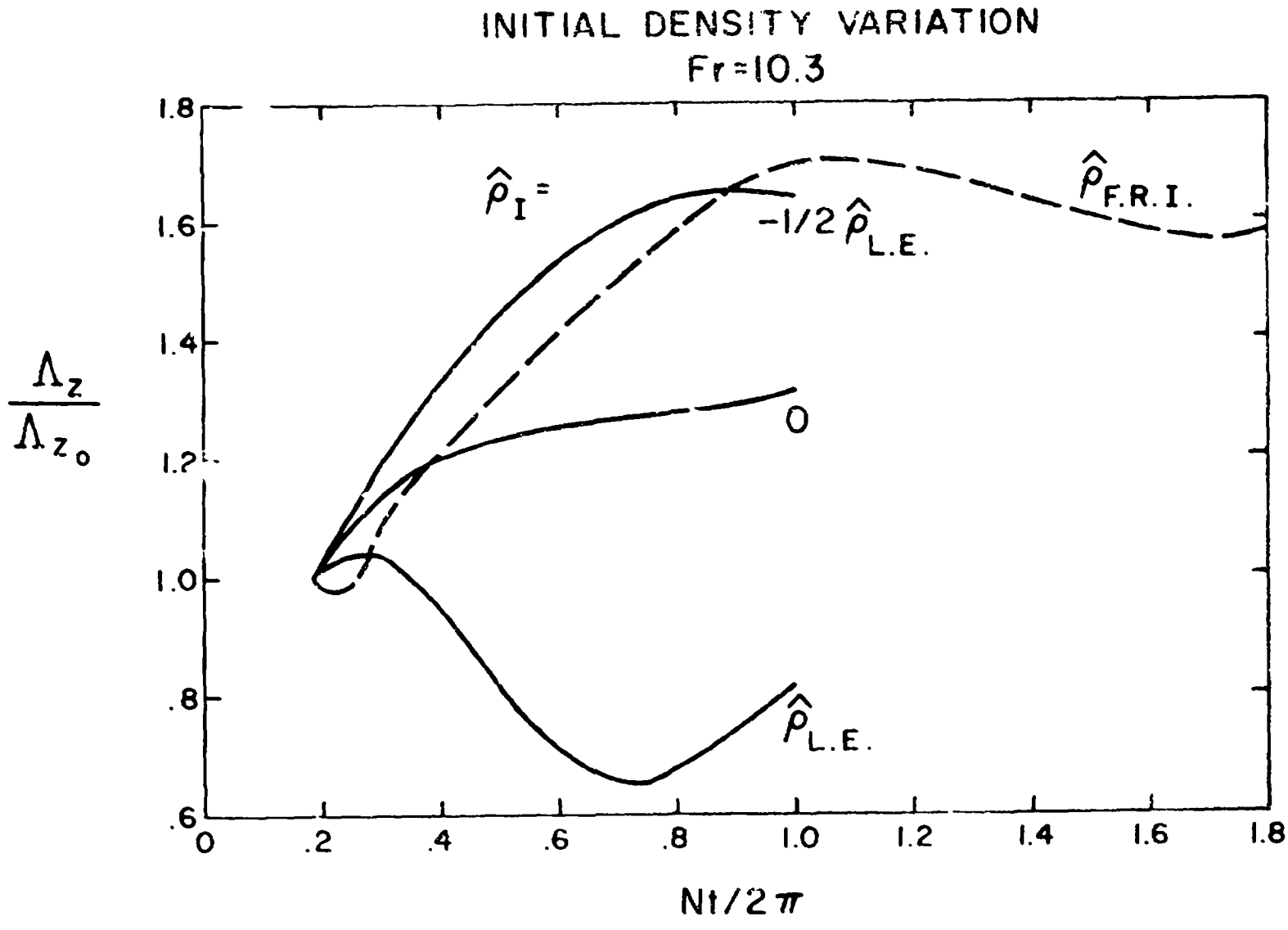

Figure 4.21: The behavior of the vertical scale Λ_z with normalized time for different initial conditions on $\hat{\rho}$.

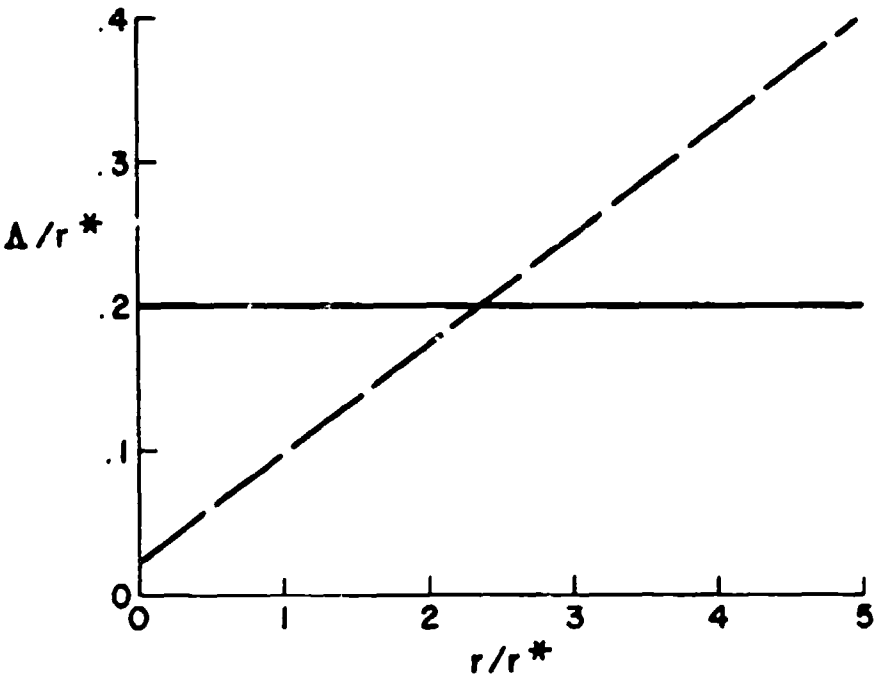

Figure 4.22: The initial profile distribution of scale length Λ versus radius r for an axisymmetric momentumless wake. The comparison is between the profile of eq. (2.16) (——) and our contrived condition (– –).

correlation there, due to the increased dissipation rate. Then the flow settles swiftly into its typical type of behavior. The initial small scale has been chewed up, and replaced by larger eddies associated with the larger scale of the turbulence near the wake edge. The maximum values of w_D, $\overline{w'w'}$, and $\overline{u'w'}$ as a function of distance behind the body for variable and constant Λ are as shown in fig. 4.23. There is very little evidence to suggest that such a strong difference existed at initiation of the two runs. From the fact that the axial velocity fluctuations agree for $x/D \gtrsim 50$ we can expect that the initial turbulent scale will have no effect on ψ_{max} for $Fr \gtrsim 40$.

4.d Sensitivity to Angular Momentum

We now turn to an examination of the sensitivity of wake collapse to variations in momentum in the three directions (marching x ; horizontal y ; vertical z). We first consider the influence of an initial swirl configuration. The initial contours with swirl for q^2, u and ψ are given in fig. 4.24. The density begins with zero value everywhere, and ψ is the product of the two compatible v and w velocities. The two major effects of the swirl may be expected to be an enhancement of mixing in the density profiles and an increased radial spreading of the wake. The first effect will be most important at low Froude numbers when the initial density distribution is important, while the second may persist even as $Fr \to \infty$ since it implies a possibly different decay rate for the turbulent energy. Figure 4.25 shows the influence of swirl on the decay of the wake characteristics for $Fr \to \infty$ when the initial maximum swirl velocity is equal to the initial velocity defect $w_D = 0.08$ U. Although q_{max} decays somewhat slower initially in the swirling case, asymptotically the two cases nearly parallel each other. The ratio of the swirl velocity to the velocity defect chosen for this sample calculation is approximately equal to that observed by Gran (ref. 34) and a factor of three higher than that for Schetz (ref. 32) initial conditions. It thus represents a relative upper limit of the influence that may be expected of propeller-induced swirl.

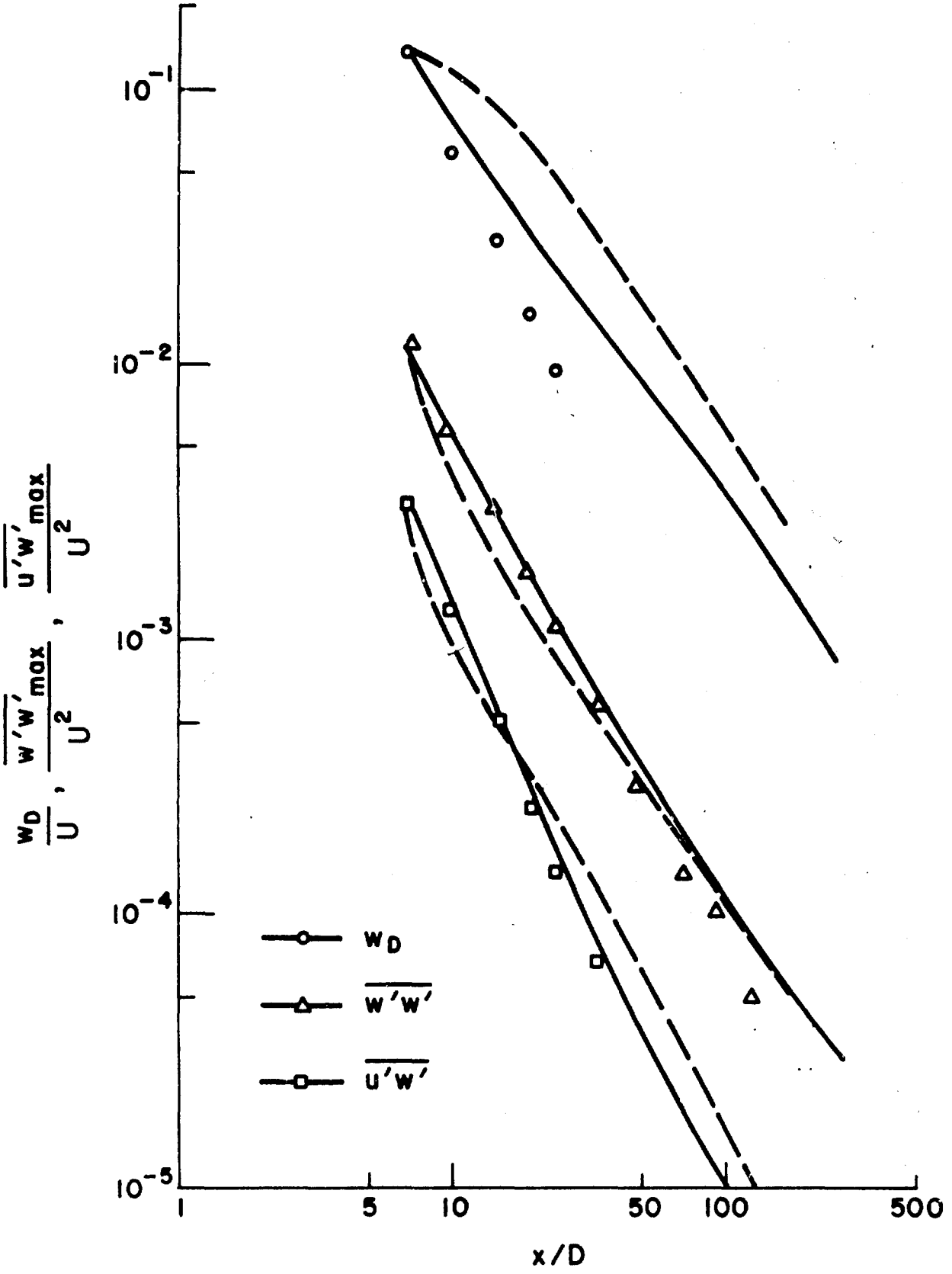

Figure 4.23: Comparison of the decay of velocity defect, shear stress, and turbulent energy for the two initial scale profiles given in fig. 4.22. Naudascher data points, o , □ , Δ , (ref. 25).

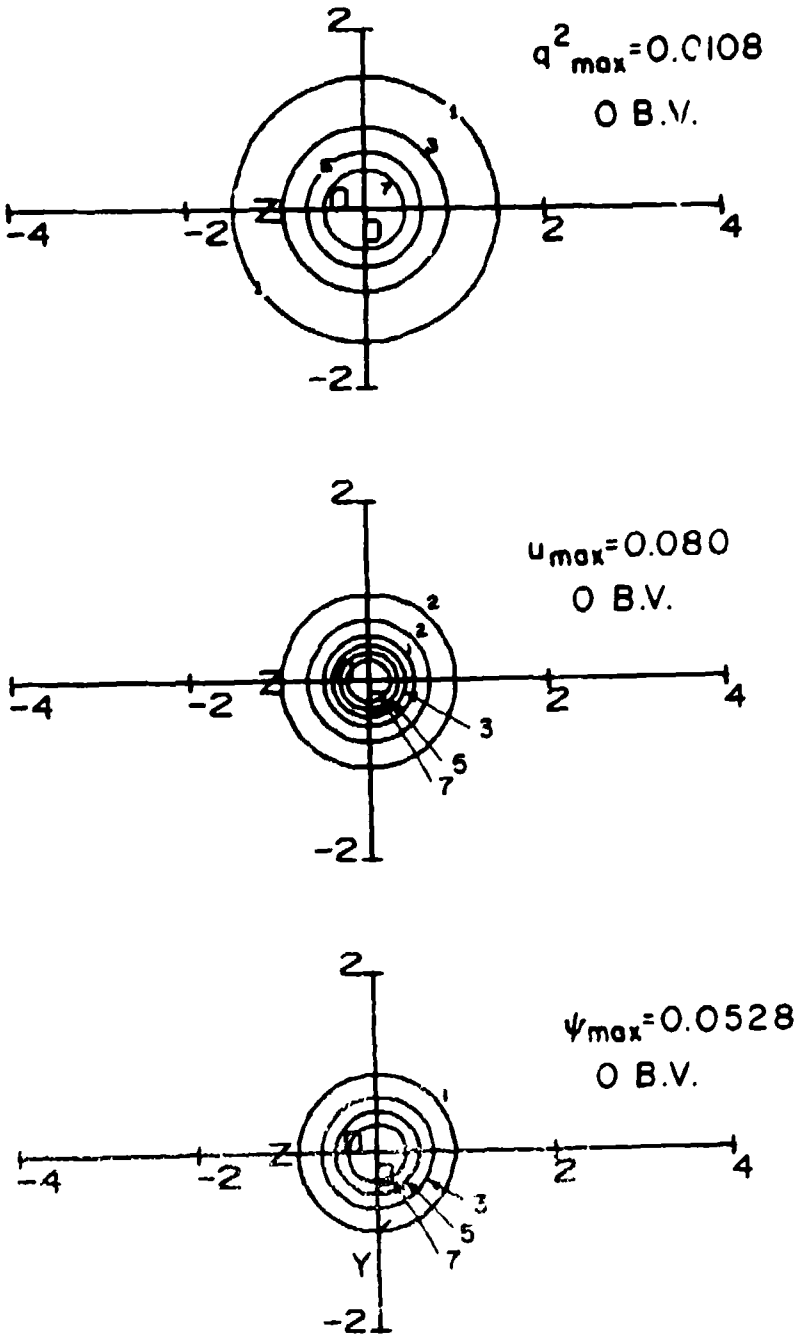

Figure 4.24: The initial contours of constant values of q^2, u and ψ for the swirling cases to be considered in fig. 4.25 - 4.41. We take q^2_{max} = 0.0108, $\hat{\nu}$ = 0, $u_{max} = v_{max} = w_{max} = 0.08$.

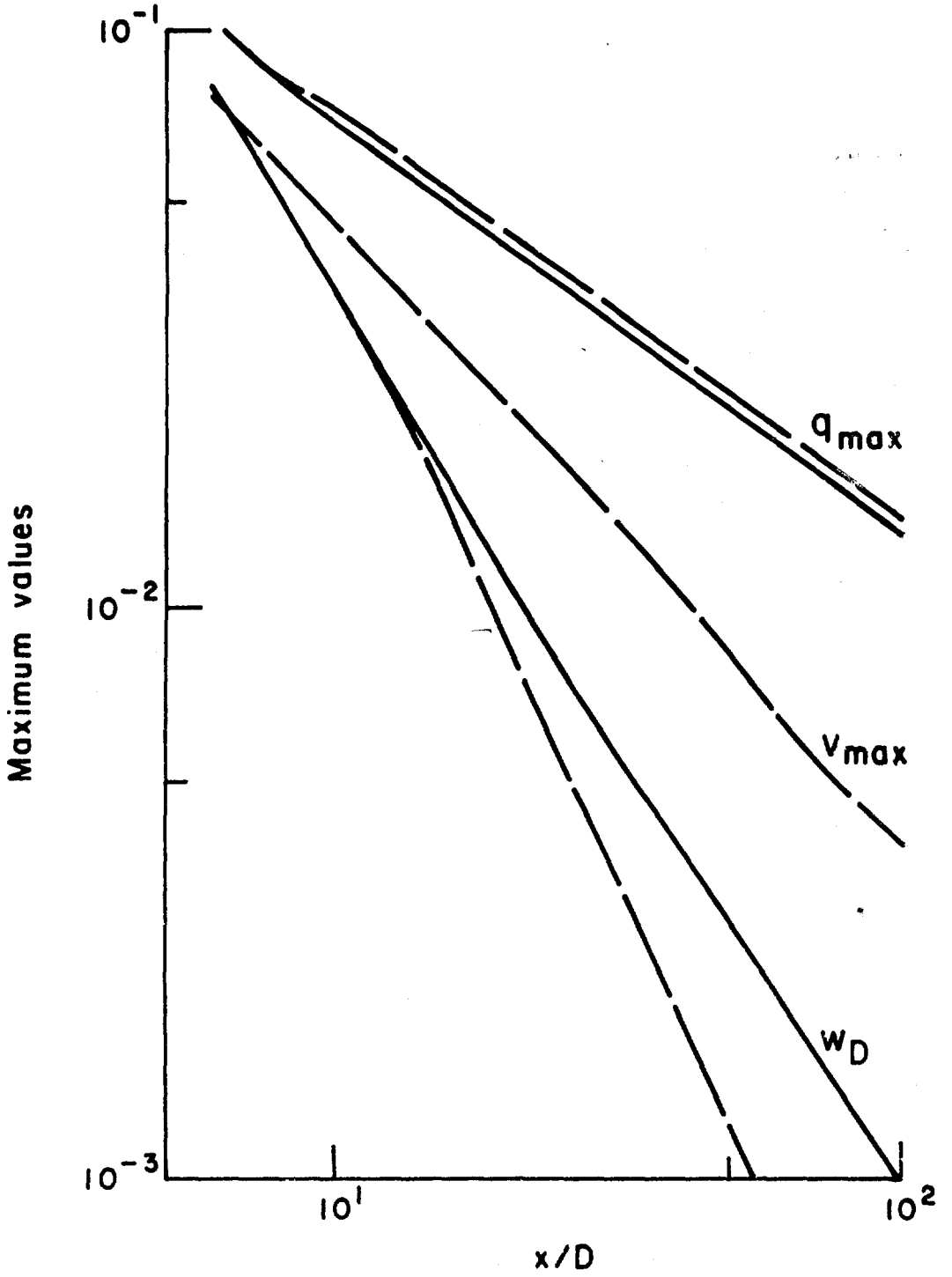

Figure 4.25: The decay of the velocity defect, turbulent energy and maximum swirl velocity for $Fr \to \infty$ for the initial conditions of fig. 4.24 (– –) with that of a nonswirling wake (—).

The decay characteristics for $Fr = 100$ and $Ri_o = 0.00925$ are shown in figs. 4.26 - 4.30. We see that q_{max} appears to decay slowly at first, and then more nearly to the typical $t^{-3/4}$ near collapse. The cross-velocities v and w decay very similarly. We may compare figs. 4.26 - 4.33 with the nonswirl run under identical conditions, figs. 4.9 - 4.13. We see that $\hat{\rho}_{max}$ reaches a larger value ($\approx 1.$ rather than 0.3) with swirl, and does not show the oscillations present in the nonswirling case. The v_{max} and w_{max} are much lower owing to their production by collapse alone, and not collapse plus swirl.

Decreasing Fr to $Fr = 10$ and $Ri_o = 0.925$ yields the plots in figs. 4.31 - 4.35. We see that q_{max}, u_{max}, v_{max} and w_{max} are stalled even longer before they begin decaying. In fact, it appears as though the collapse dynamics has caught w before it decays very much. Likewise, $\hat{\rho}_{max}$ does not reach as large a peak value prior to collapse. The contours are very consistent here.

We may also compare this swirl collapse, fig. 4.31, with the linear-exponential collapse at $Ri_o = 0.872$, shown earlier in fig. 4.14. Although the maximum values take different routes to collapse, at collapse $\hat{\rho}_{max}$, q_{max}, v_{max} and w_{max} possess correspondingly similar magnitudes. We have also repeated fig. 4.16 here as fig. 4.36 with the two dashed curves indicating the two swirling runs.

From these runs we conclude that at low Fr the major effect of propeller-induced swirl appears to be to introduce more complete mixing into the wake as the wake spreads more rapidly, forcing a stronger collapse. At $Fr = 100$ the major influence appears to be an asymmetry remaining in the flow contours which permits the slight difference in vertical height seen in fig. 4.36 and the significant difference in energy radiated in Table 4.1 shown later. For still higher values of Fr we would expect smaller differences due to propeller-induced swirl.

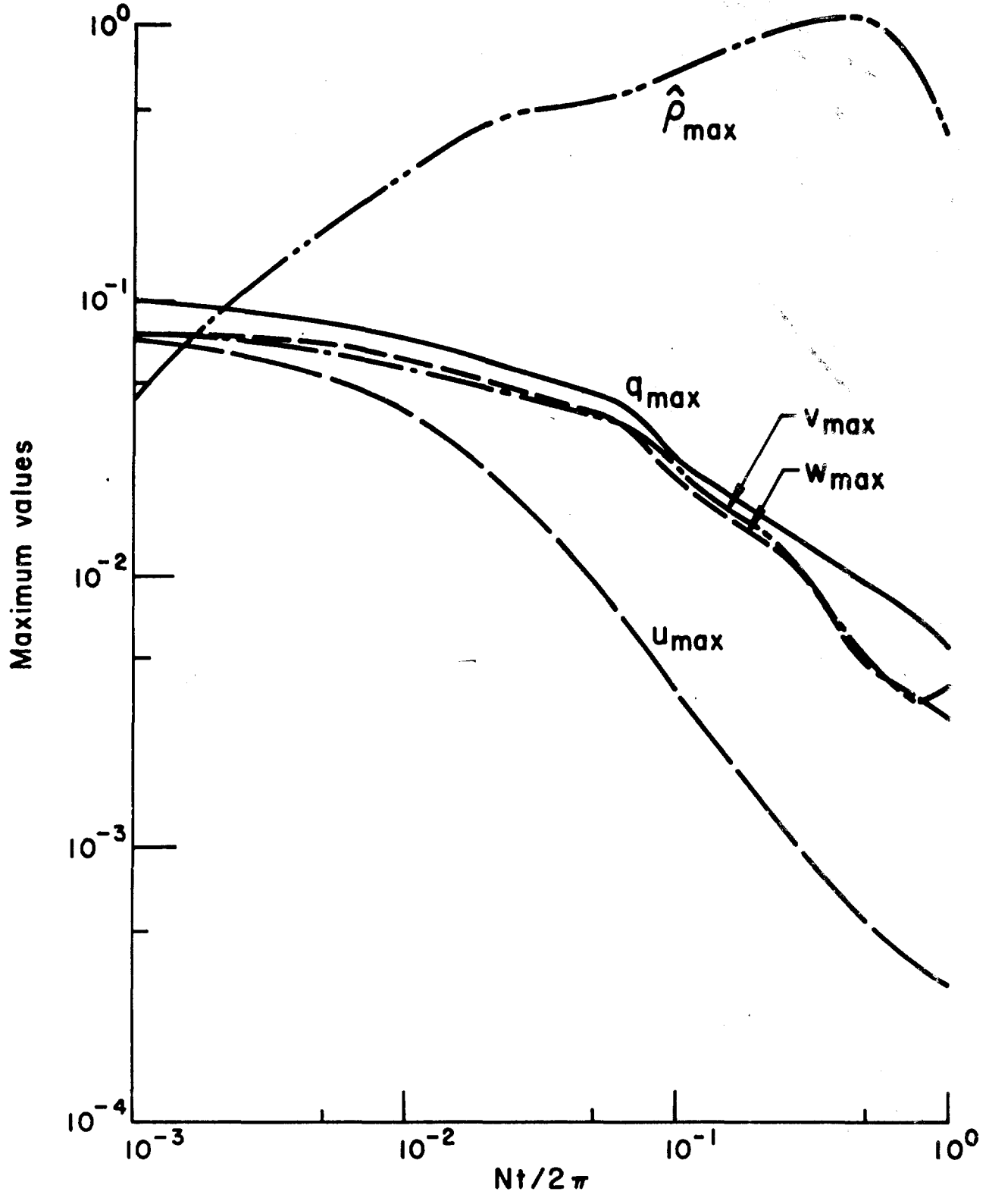

Figure 4.26: The decay of maximum values of q, $\hat{\rho}$, u, v and w for $Ri_o = 0.00925$ with swirl and initial conditions given in fig. 4.24.

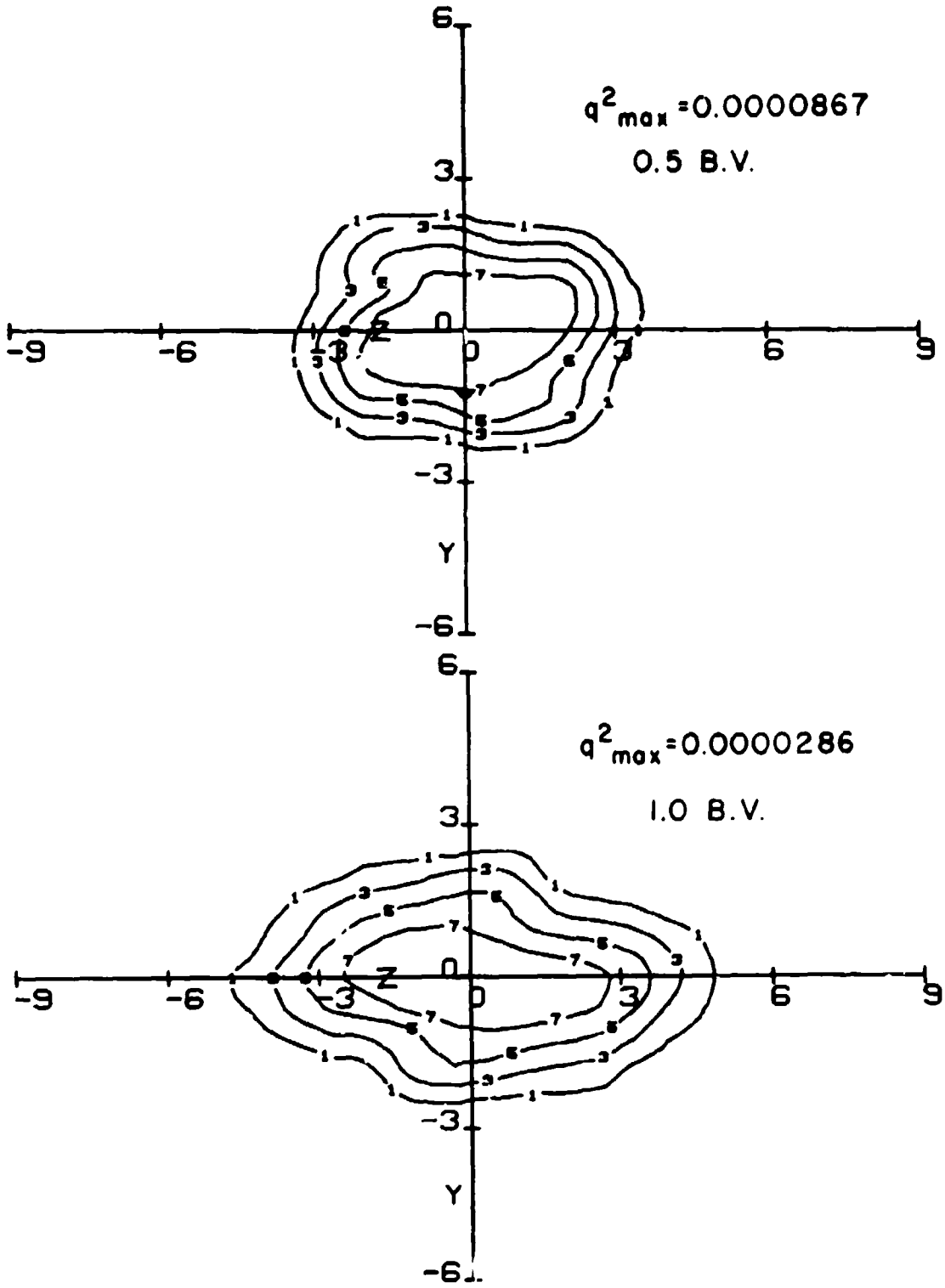

Figure 4.27: Contours of constant q^2 for the conditions of fig. 4.26 (see fig. 4.2 for contour code).

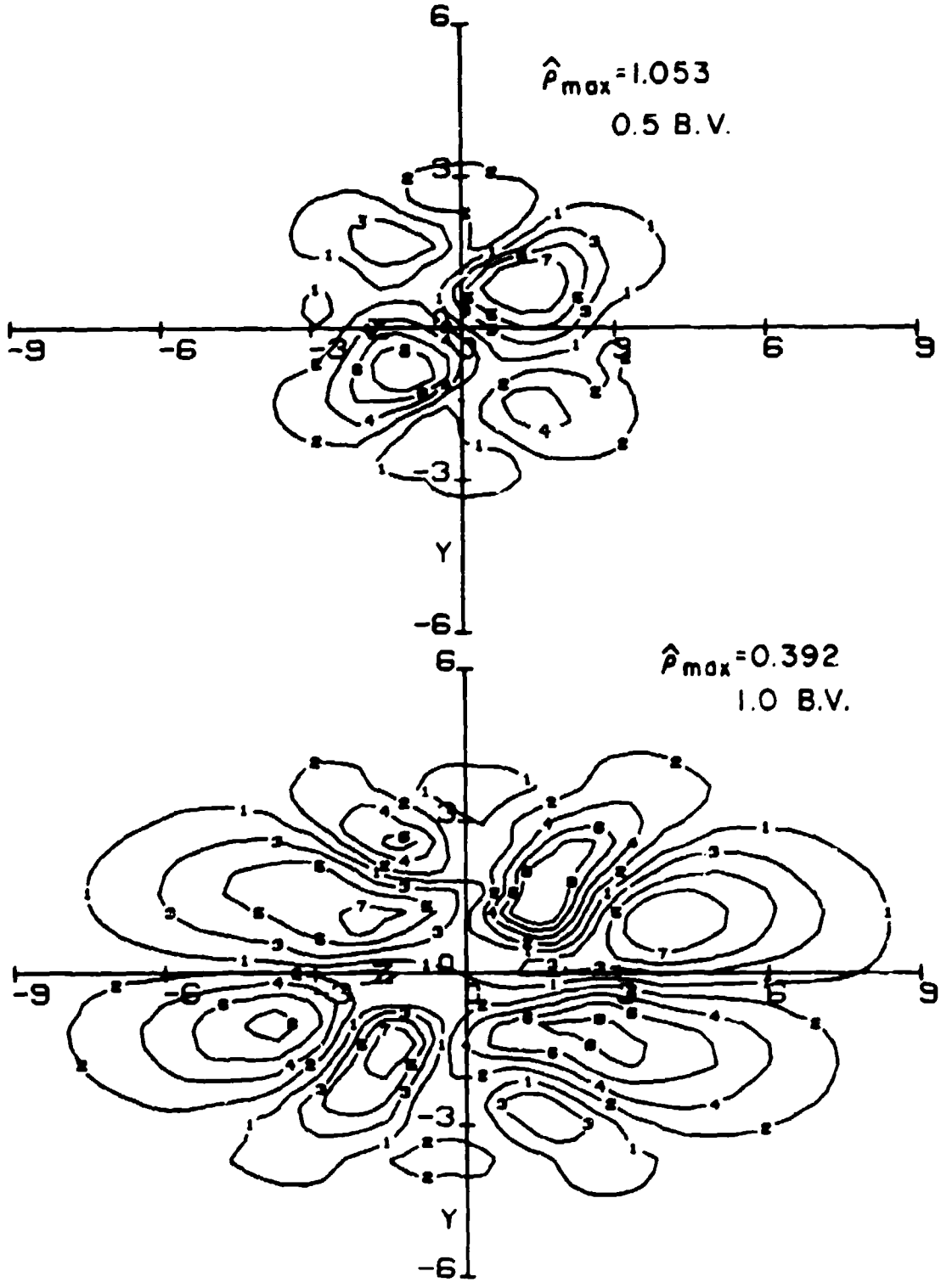

Figure 4.28: Contours of constant $\hat{\rho}$ for the conditions of fig. 4.26 (see fig. 4.2 for contour code).

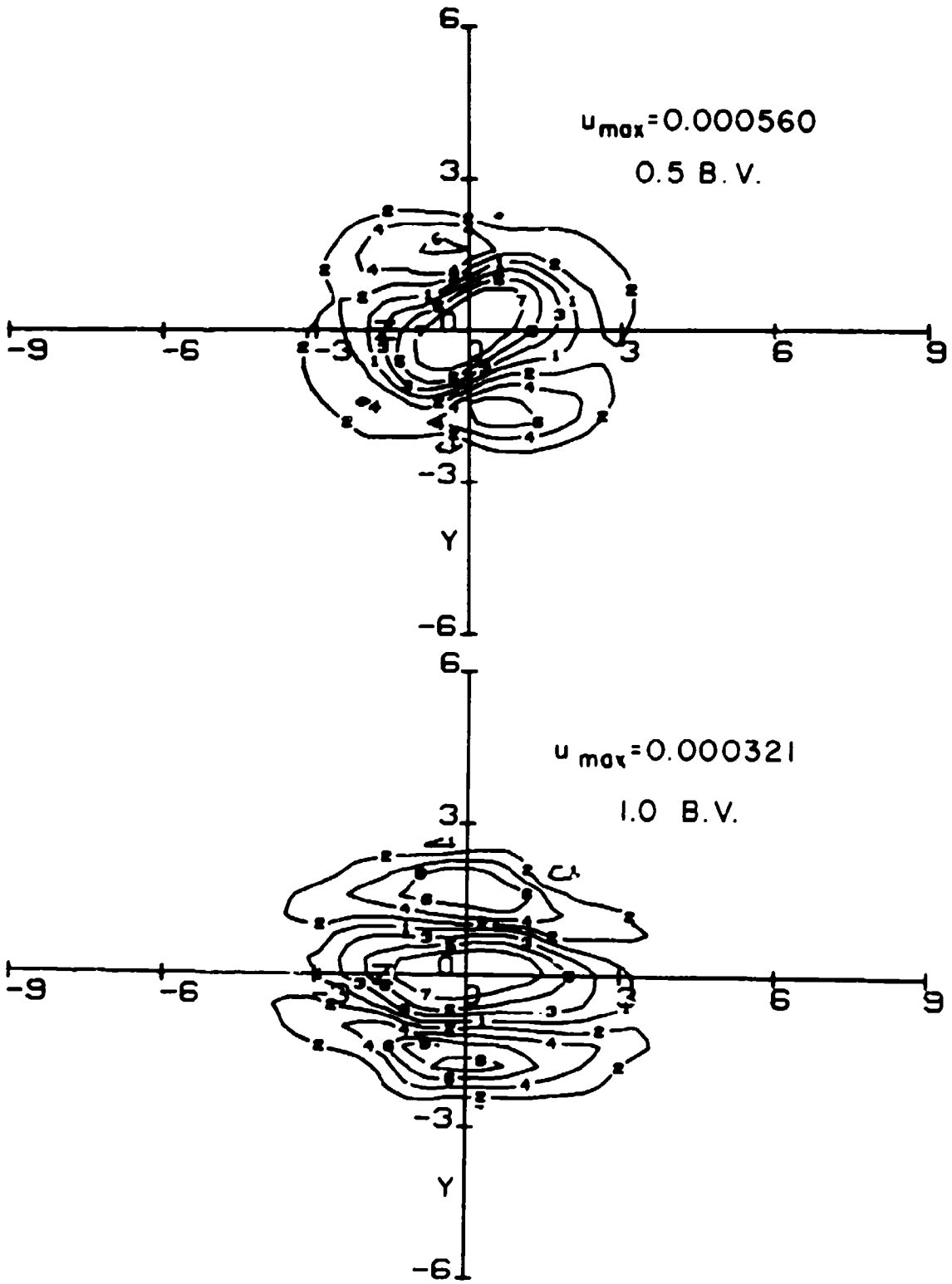

Figure 4.29: Contours of constant u for the conditions of fig. 4.26 (see fig. 4.2 for contour code).

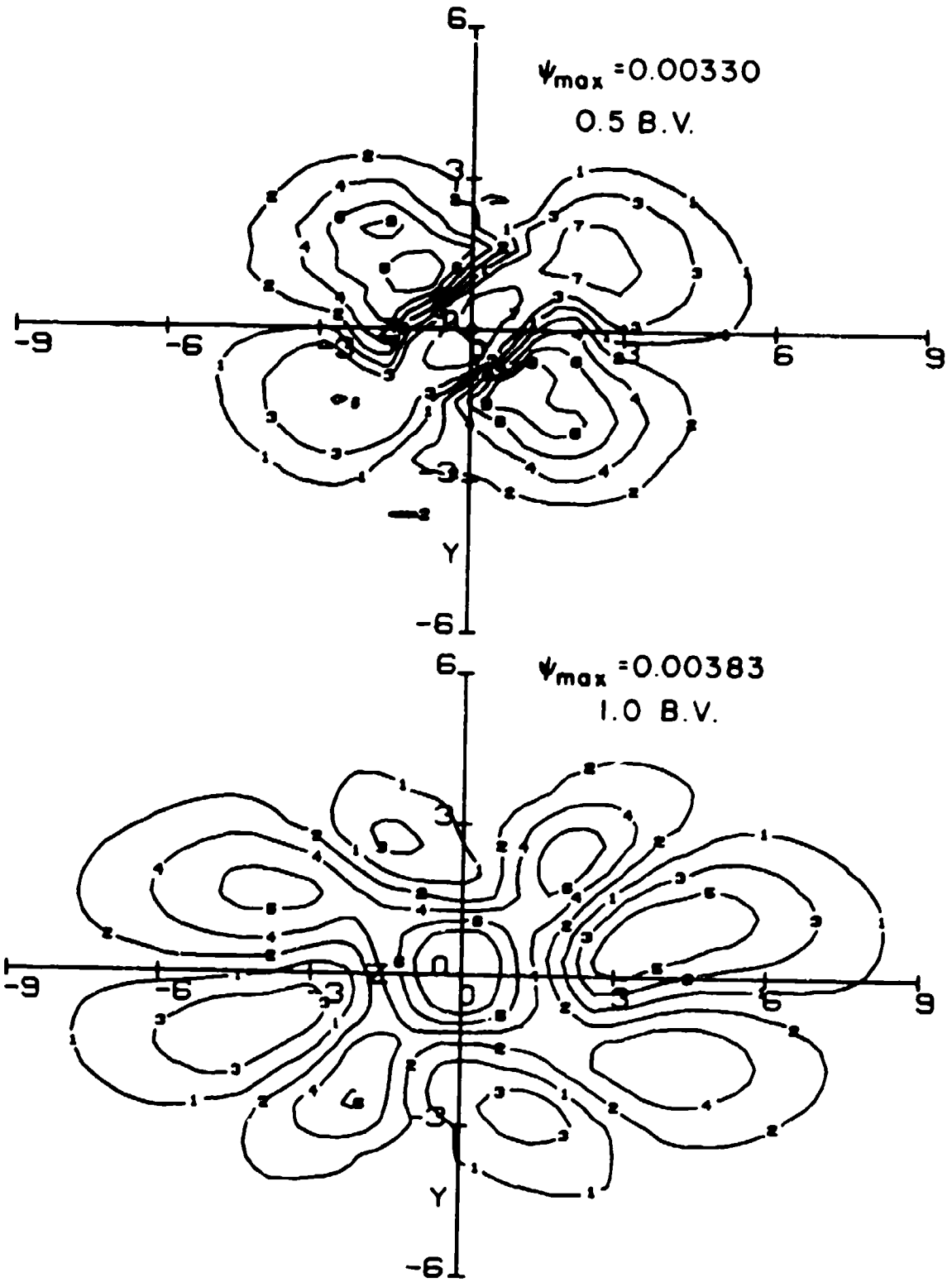

Figure 4.30: Contours of constant ψ for the conditions of fig. 4.26 (see fig. 4.2 for contour code).

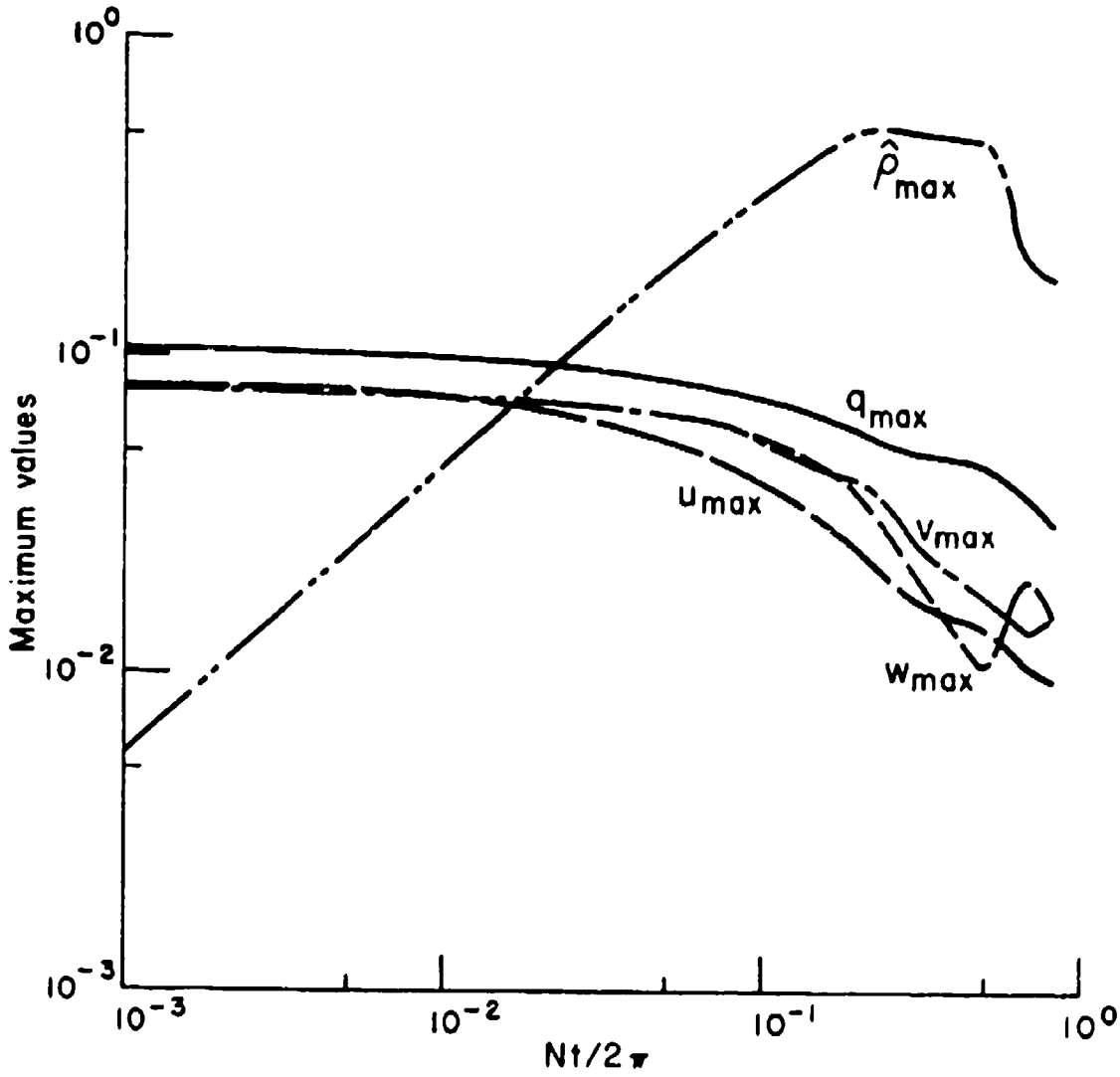

Figure 4.31: Decay of maximum values of q, $\hat{\rho}$, u, v and w for $Ri_o = 0.925$ with swirl and the initial conditions given in fig. 4.24.

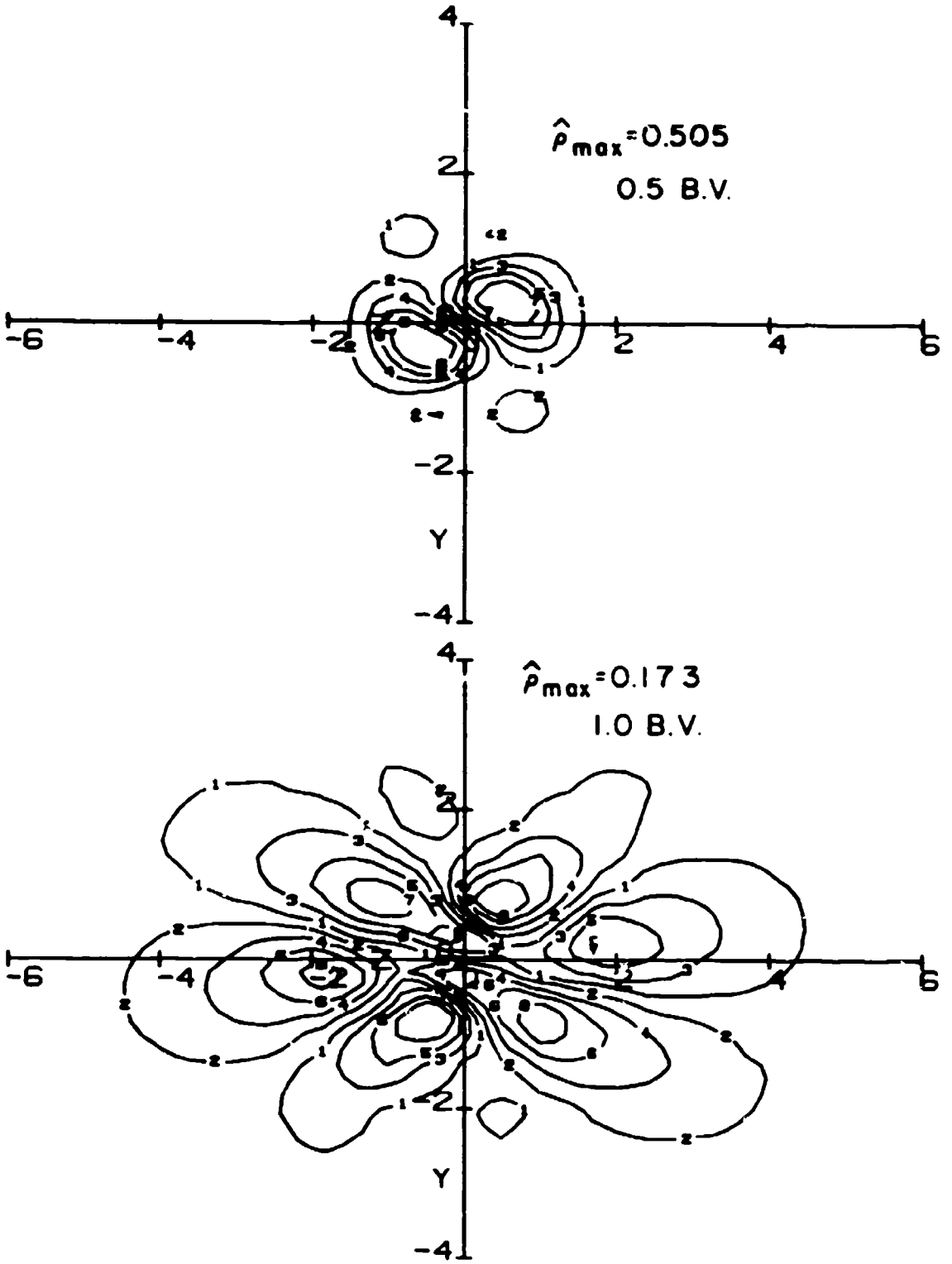

Figure 4.33: Contours of constant $\hat{\rho}$ for the conditions of fig. 4.31 (see fig. 4.2 for contour code).

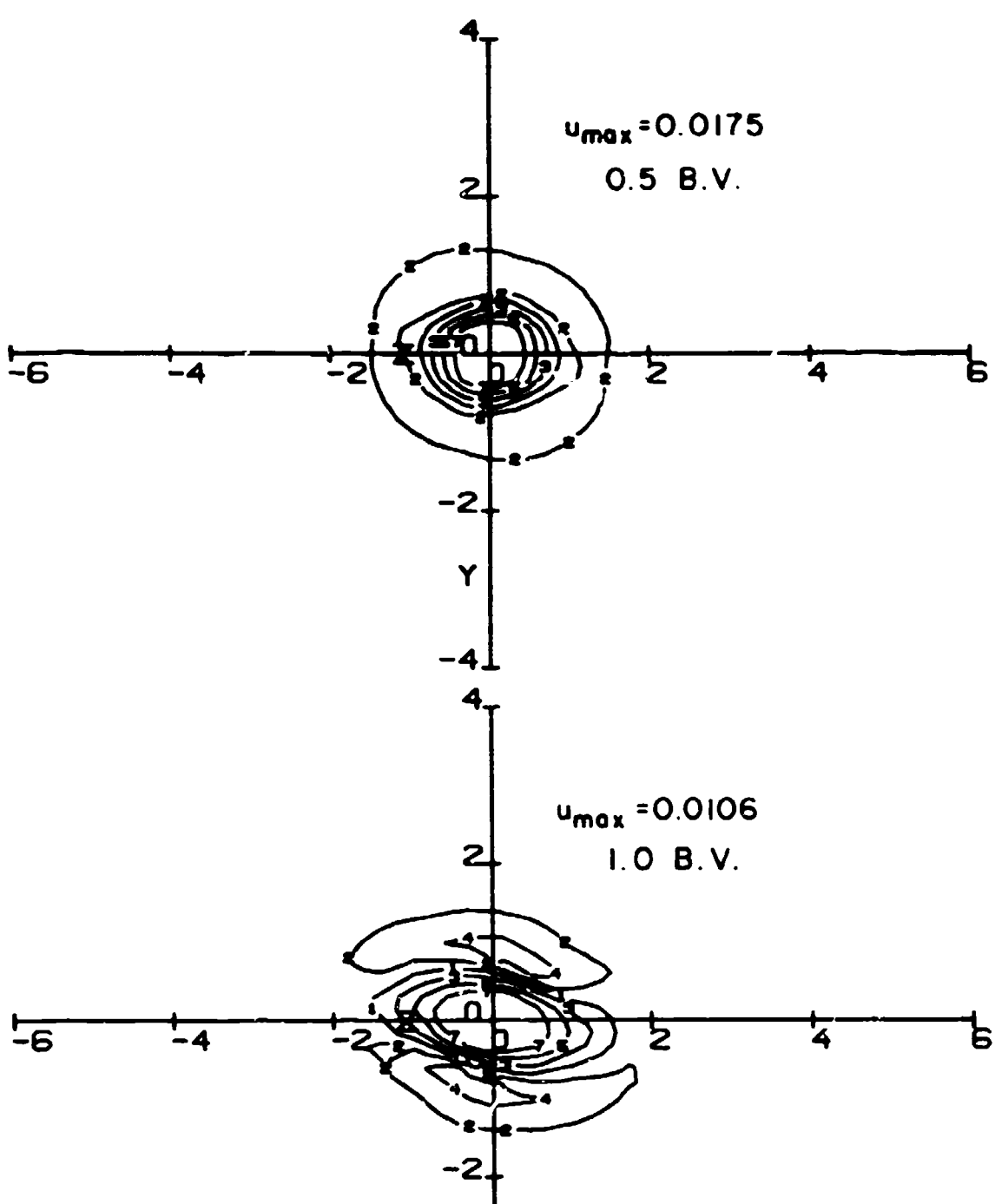

Figure 4.34: Contours of constant u for the conditions of fig. 4.31 (see fig. 4.2 for contour code).

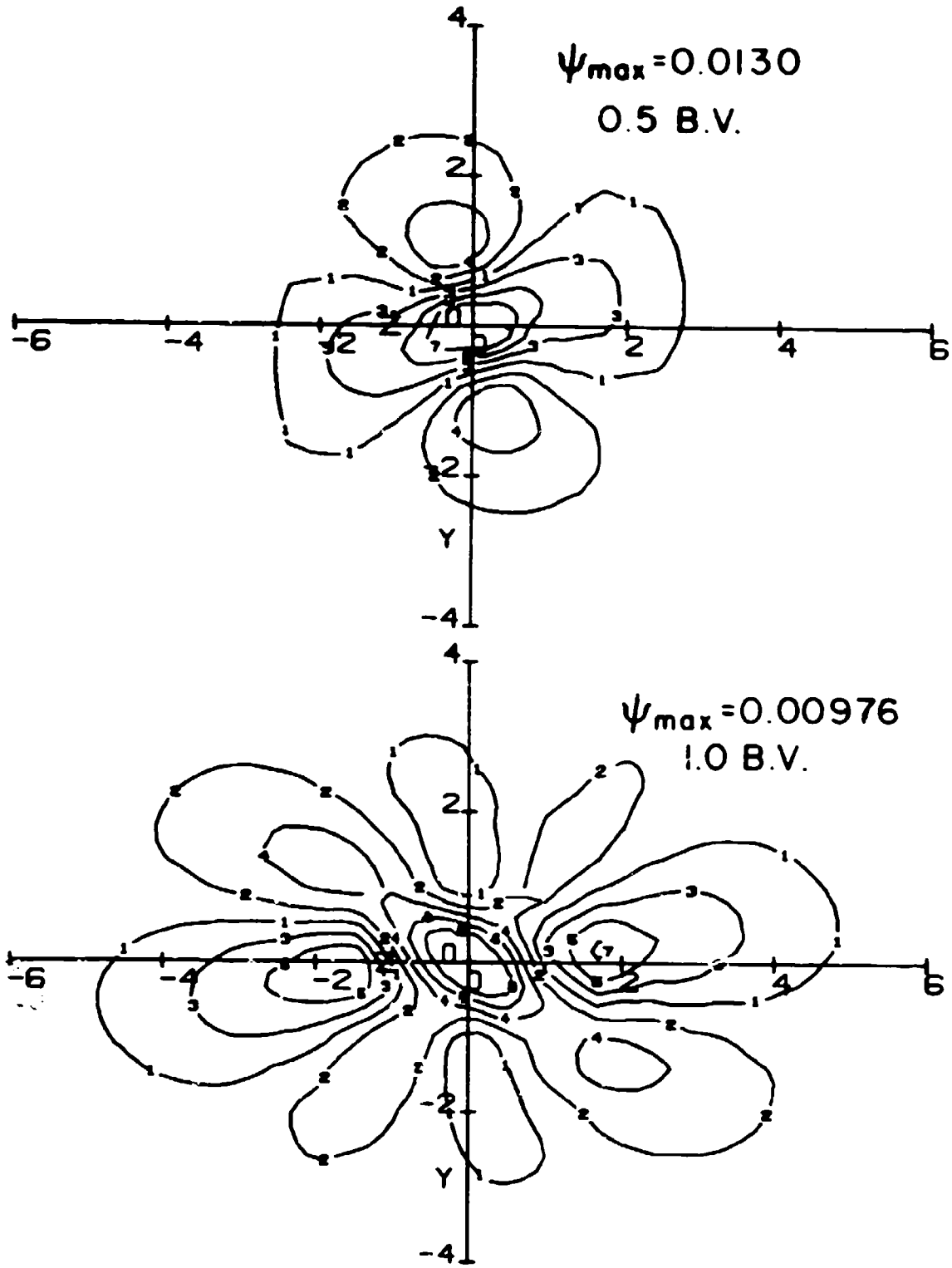

Figure 4.35: Contours of constant ψ for the conditions of fig. 4.31 (see fig. 4.2 for contour code).

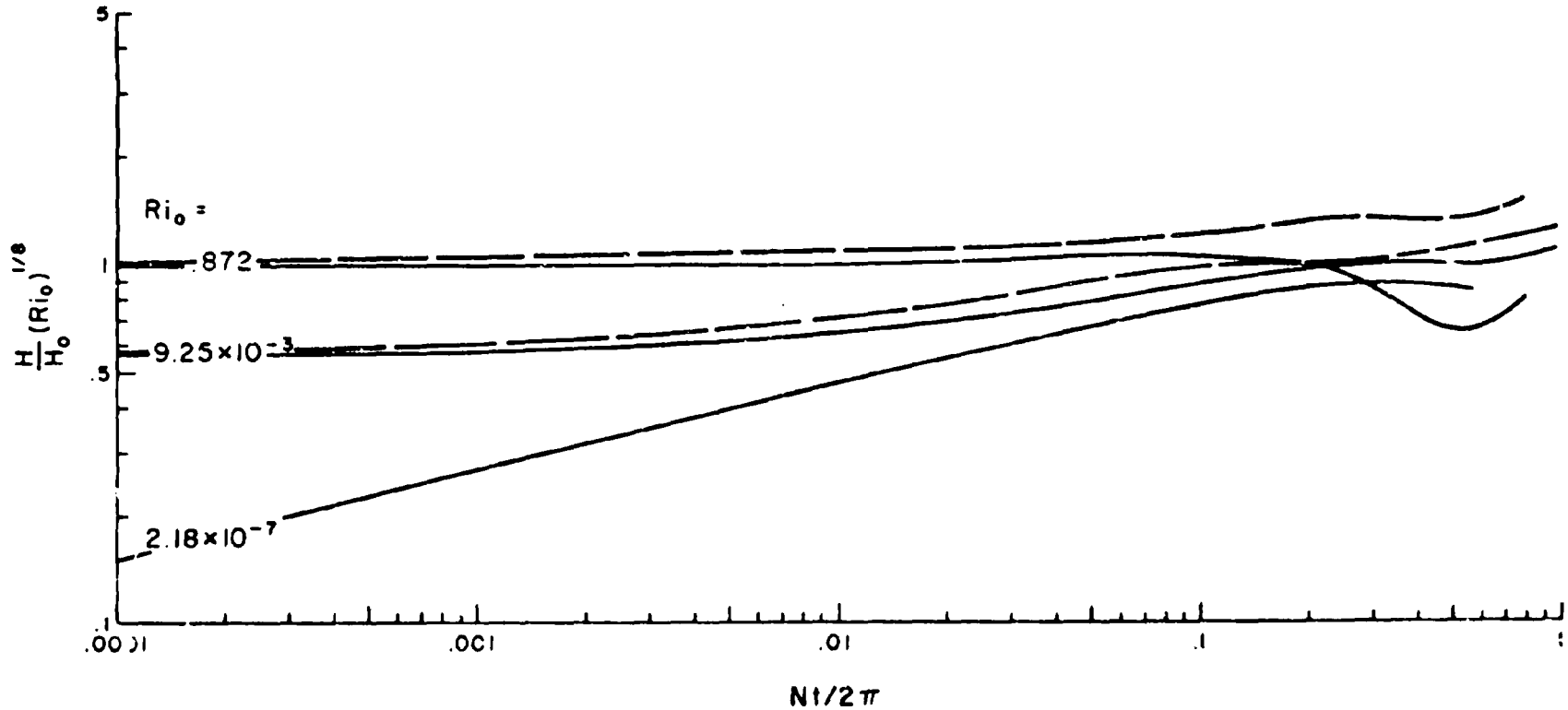

Figure 4.36: Comparison of the normalized vertical scale behavior vs. normalized time for the two swirling cases (– –) of fig. 4.26 and 4.31 with fig. 4.15.

4.e Sensitivity to Axial Momentum

We may estimate the effect of nonzero streaming momentum (in the x direction) by returning to the FRI data run given in the Appendix. If we use a symmetrical version of their q^2 and u profiles, along with our linear-exponential density profile, we obtain the collapse characteristics shown in fig. 4.37-4.41. In comparing the time history of the maximum values with the $Ri_o = 0.872$ run, fig. 4.14, we see a very close similarity across the entire B.V. scale. There is a slower decay in the turbulence level reflecting the fact that a wake with momentum decays at a slower rate than a momentumless wake (see figs. 2.4 and 2.6). However this has little effect on the cross flow. Apparently the low Fr and the well-mixed nature of the initial condition make the collapse of the wake imminent so the slight difference in turbulent decay rate does not have time to affect the other flow quantities. We would expect the influence of axial momentum to increase as Fr is increased and the wake is permitted to decay further before the major cross-flow is generated.

4.f Sensitivity to Vertical Momentum

When we include some lift force, to simulate vertical momentum, we begin the wake run with profiles in which we have two vortices located away from the center of the turbulent wake (only the $y > 0$ side will be shown). The maximum velocity of the lift induced vortex is approximately equal to the axial velocity defect yielding a positive lift that is 0.5 times the integrated turbulent kinetic energy divided by the free stream velocity (for a propulsive efficiency of 0.5 this would correspond to a lift-to-drag ratio of 1). This ratio is a larger value than we would typically expect from a nearly axisymmetric body. The initial density is taken to be zero, and we run with $Fr = 100$, or $Ri_o = 0.00925$. The maximum values and contour plots for negative trim are shown in figs. 4.42 - 4.46. We see that the maximums exhibit a behavior similar to the behavior

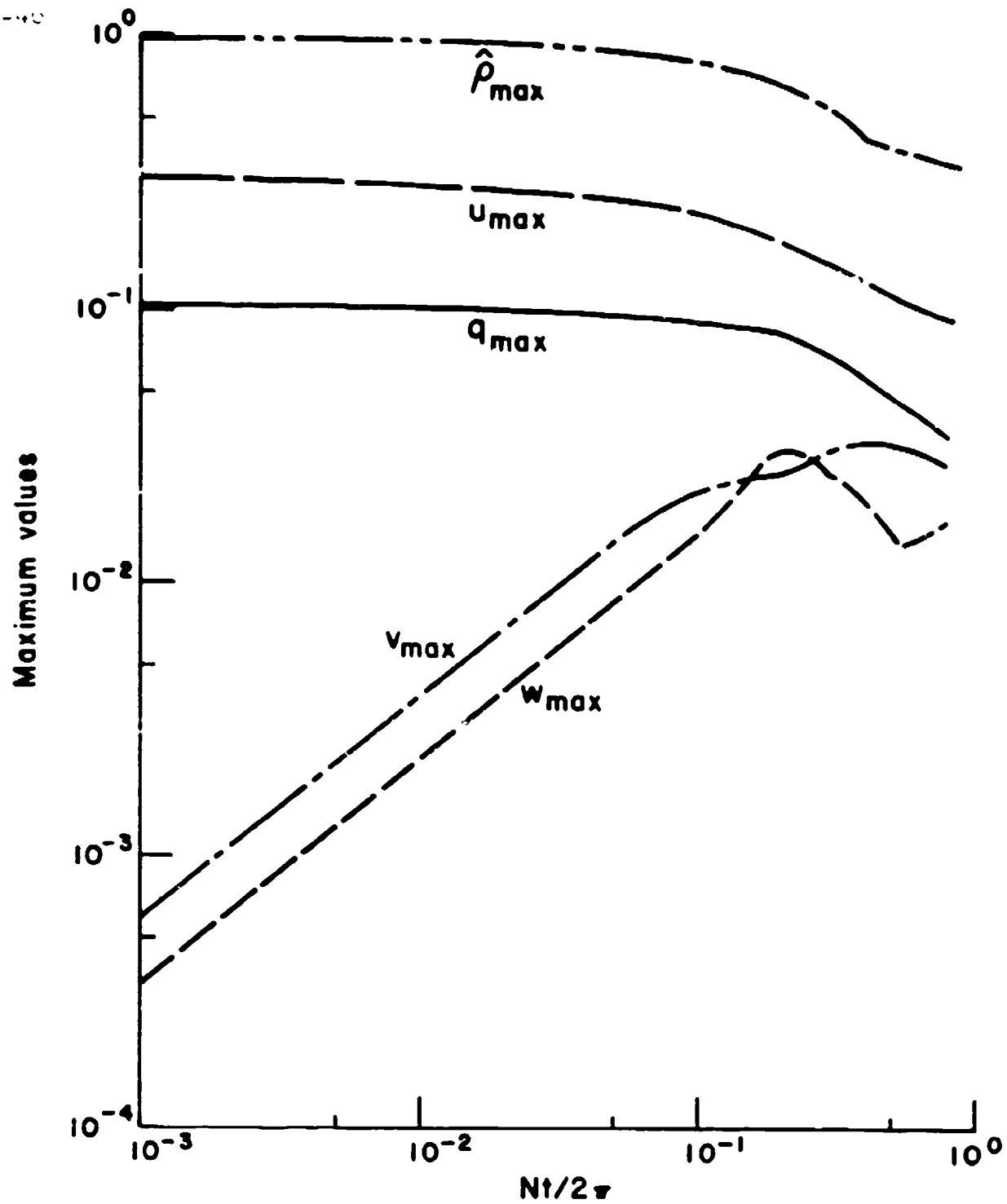

Figure 4.37: Decay of maximum values of q, $\hat{\rho}$, u, v and w for $Ri_o = 0.855$ for a wake behind a drag body. Here, $q^2_{max} = 0.0108$, $\hat{\rho}_{max} = 1$, $u_{max} = 0.305$, $v = w = 0$.

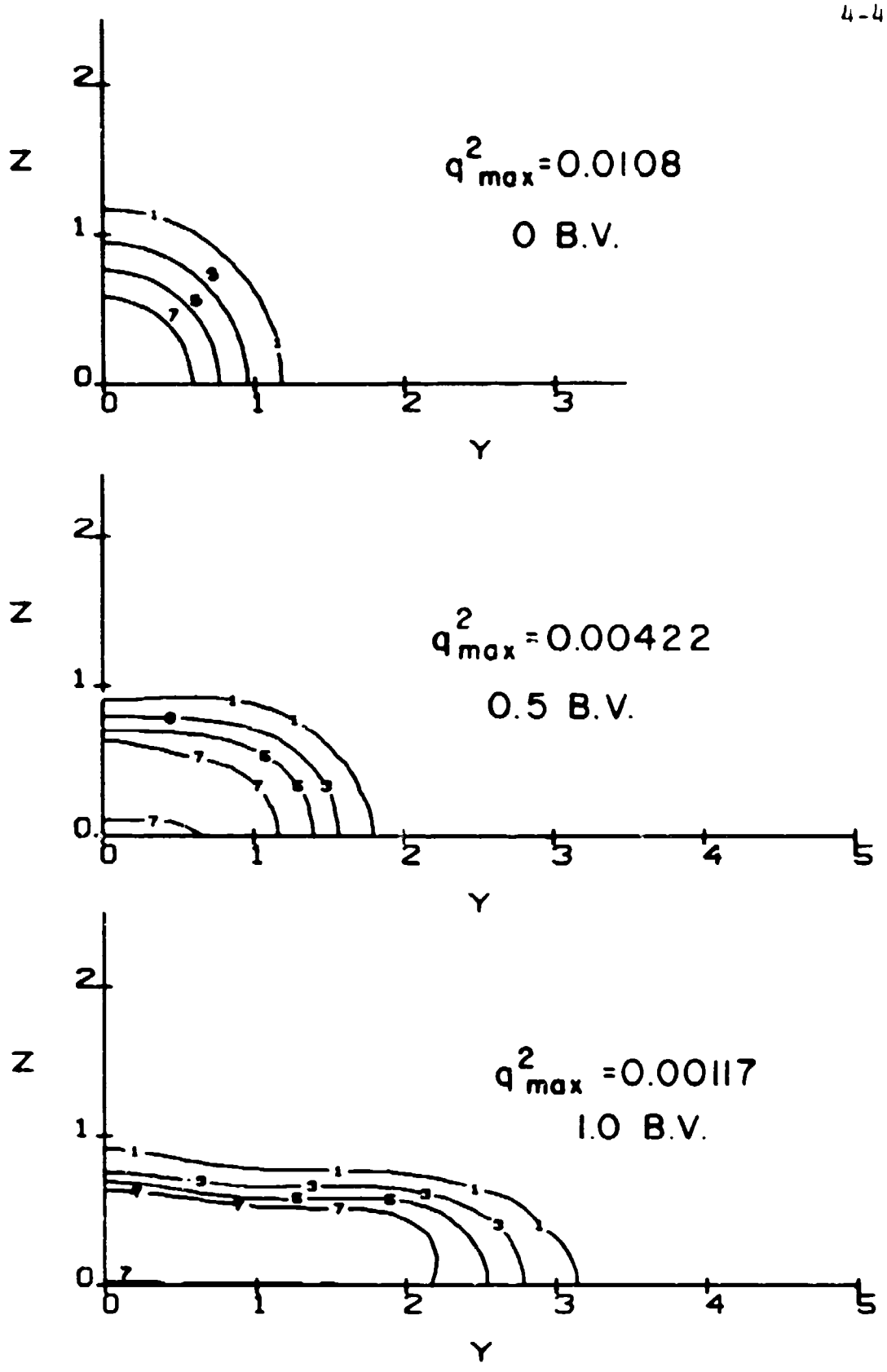

Figure 4.38: Contours of constant q^2 for the conditions of fig. 4.37 (see fig. 4.2 for contour code).

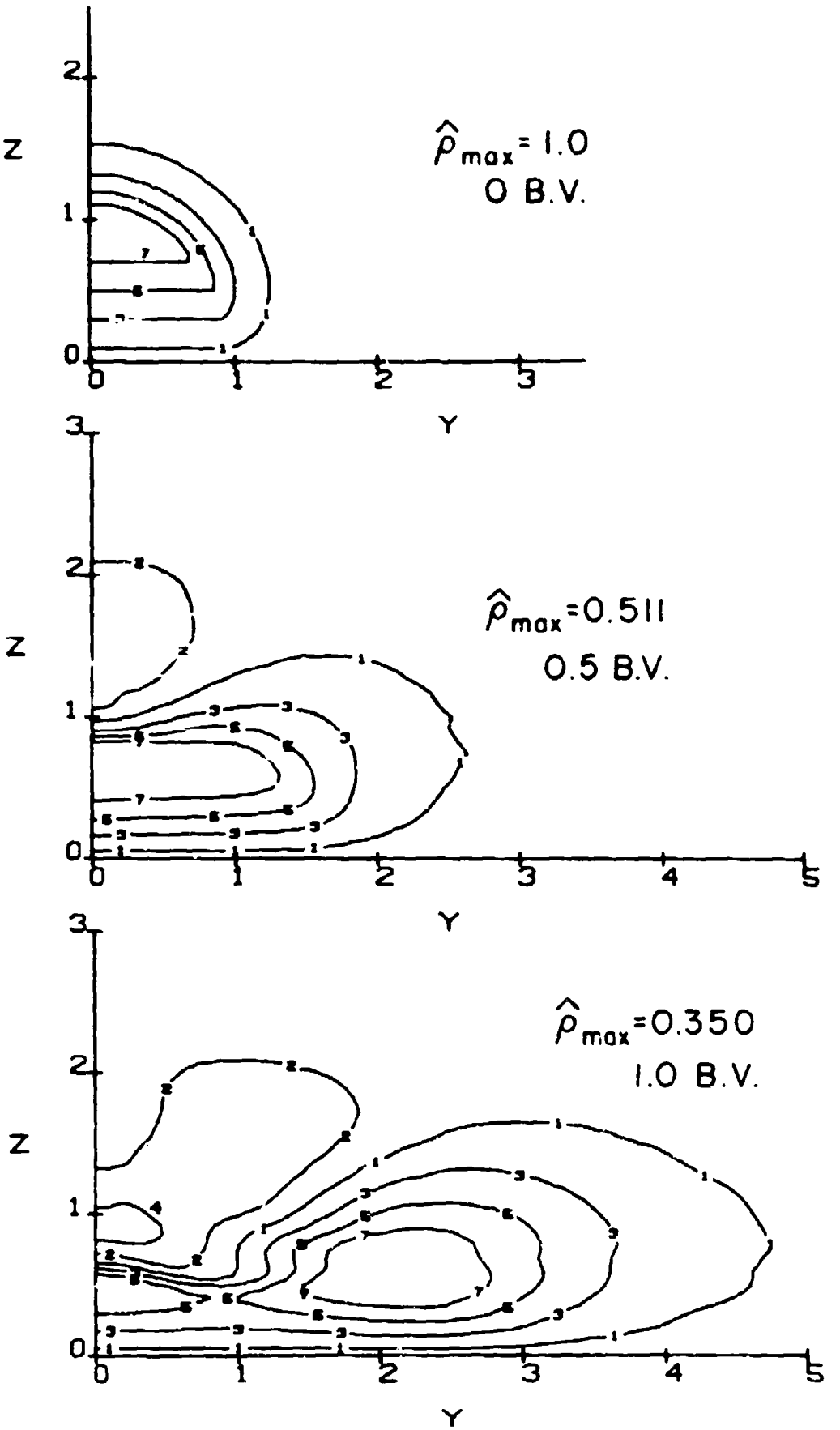

Figure 4.39: Contours of constant $\hat{\rho}$ for the conditions of fig. 4.37 (see fig. 4.2 for contour code).

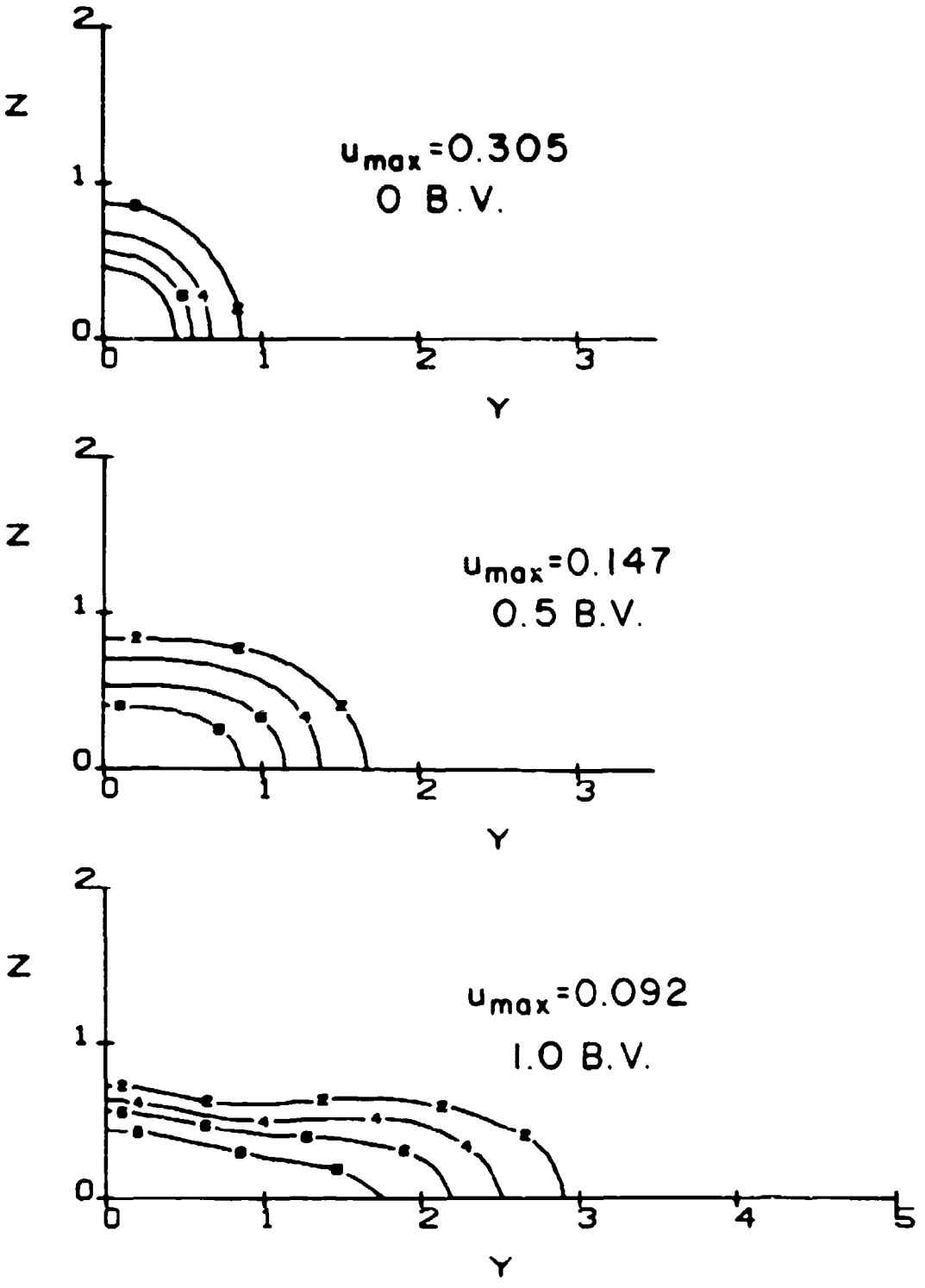

Figure 4.40: Contours of constant u for the conditions of fig. 4.37 (see fig. 4.2 for contour code).

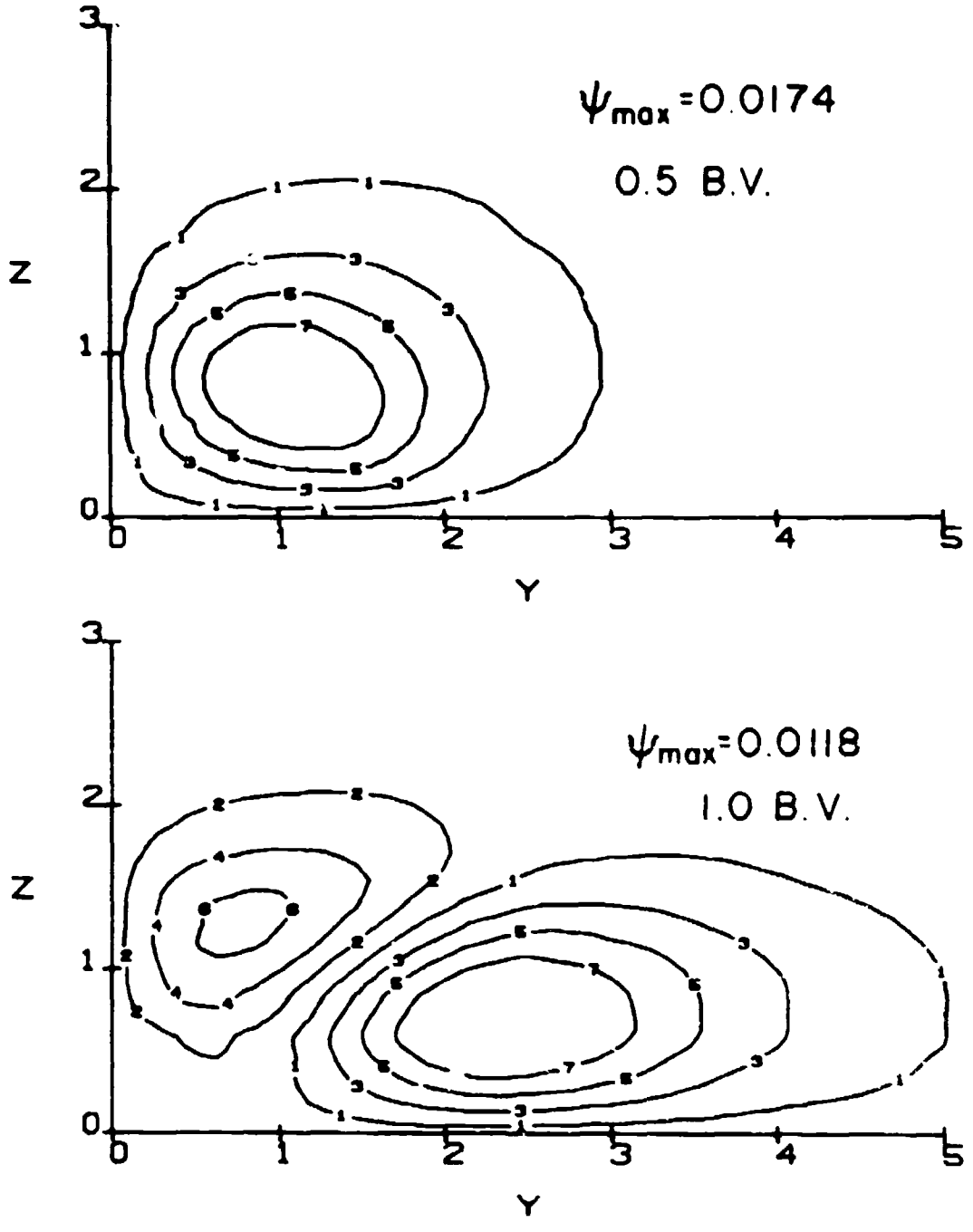

Figure 4.41: Contours of constant ψ for the conditions of fig. 4.37 (see fig. 4.2 for contour code).

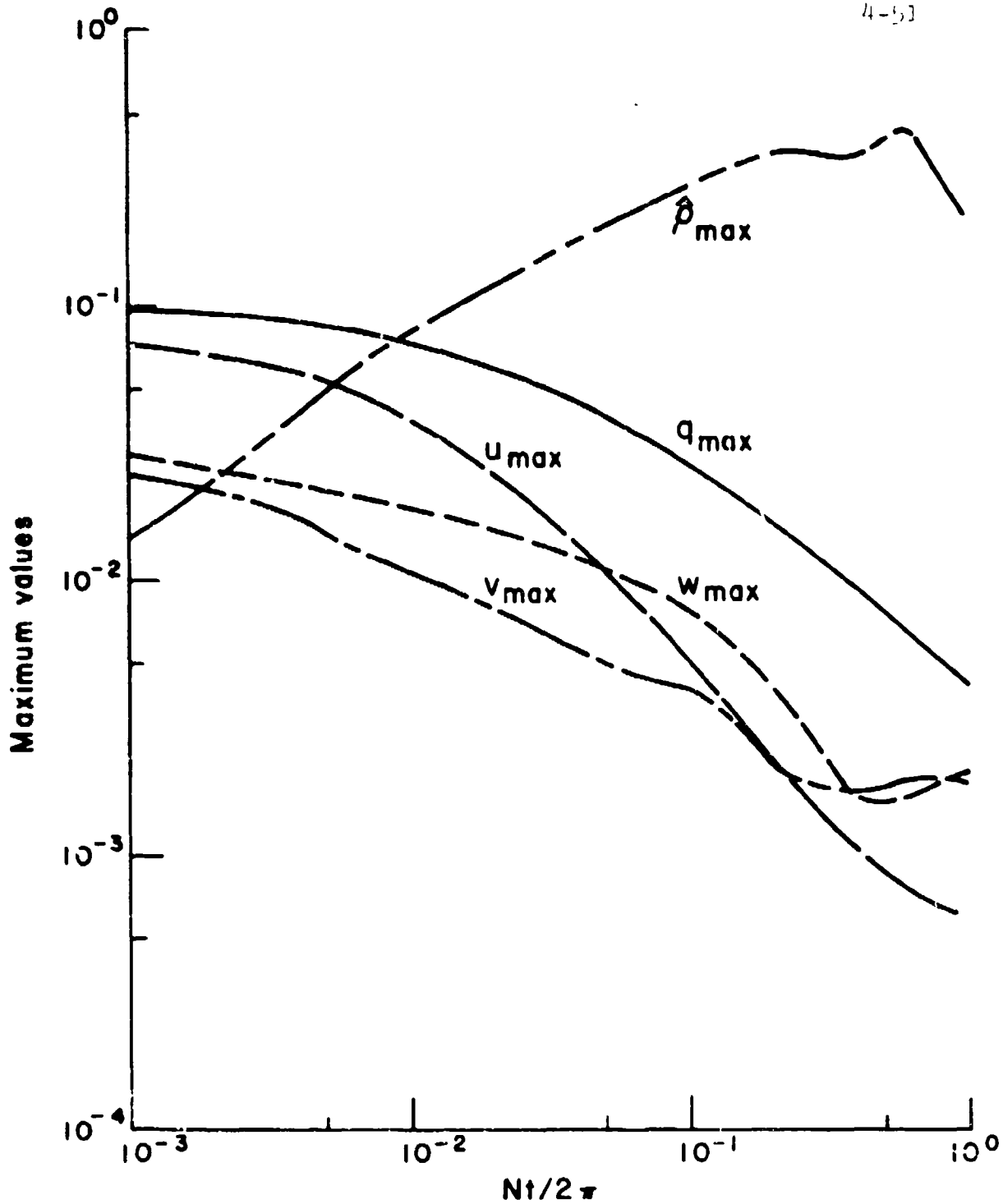

Figure 4.42: The decay of maximum values of q, $\hat{p}$, u, v and w for a vortex pair generating negative lift force at $Ri_o = 0.00925$. Here we begin with $q^2_{max} = 0.0108$, $\hat{p} = 0$, $u_{max} 0.08$, and lift/drag ≈ -1.

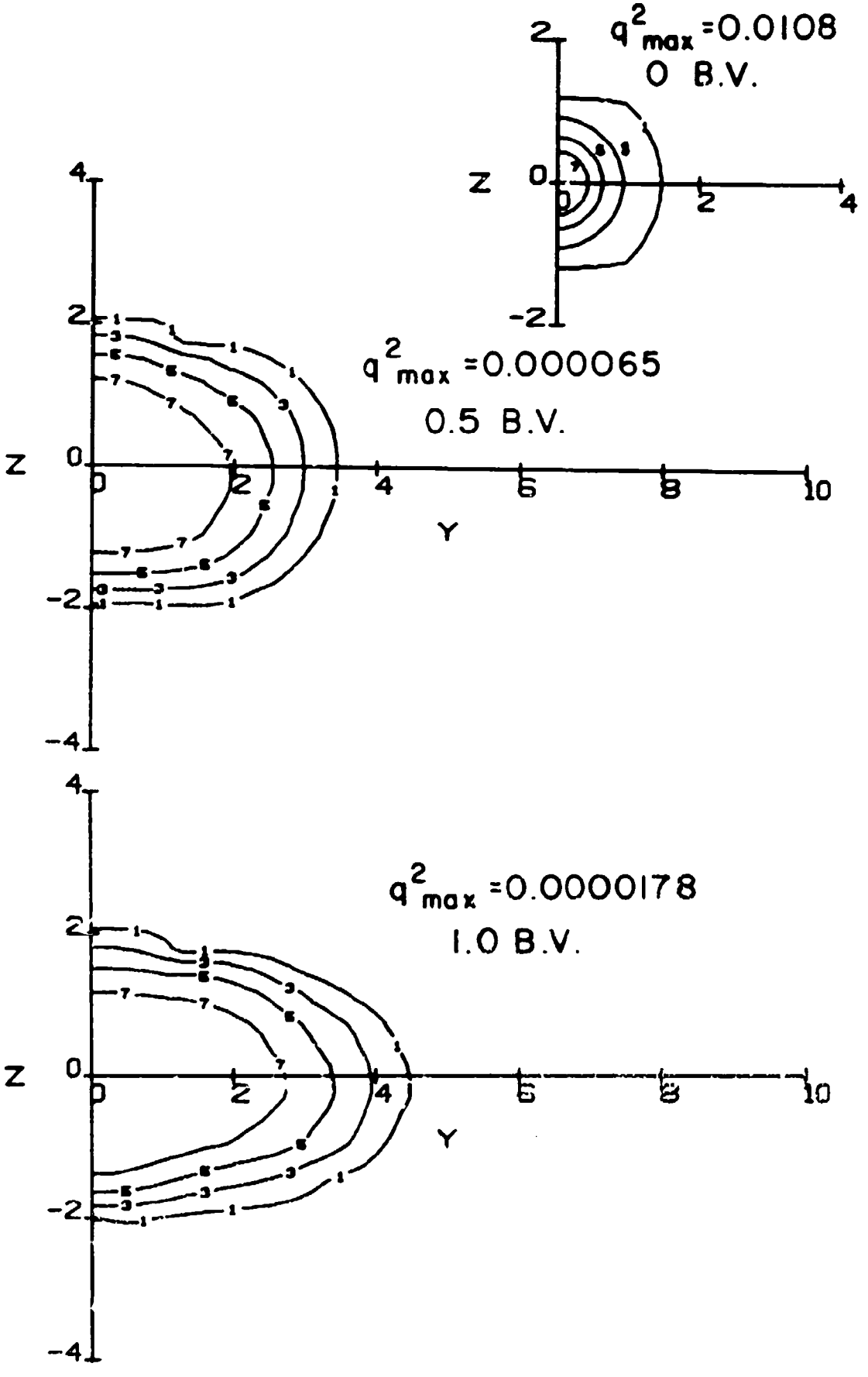

Figure 4.43: Contours of constant q^2 for the conditions of fig. 4.42 (see fig. 4.2 for contour code).

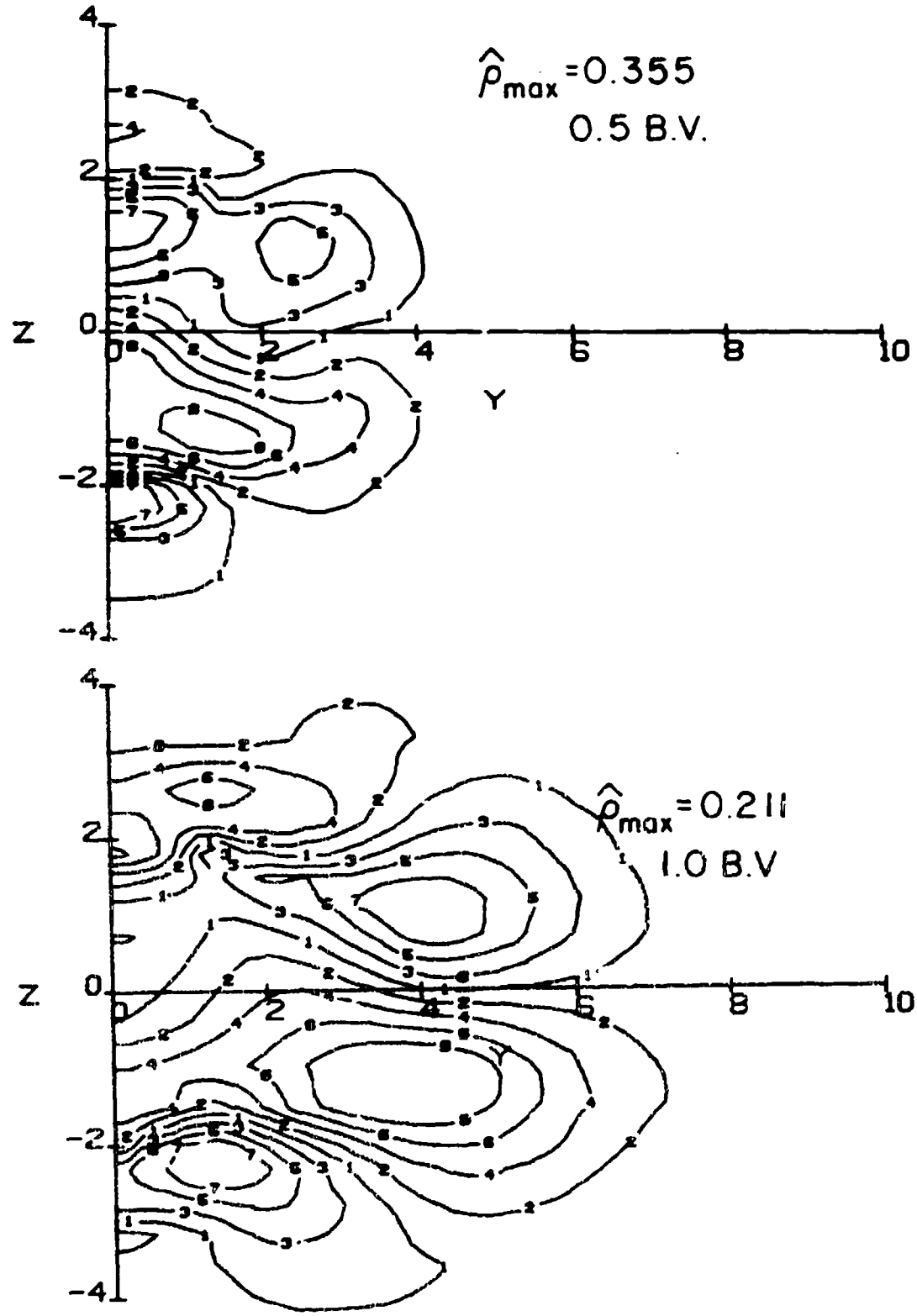

Figure 4.44: Contours of constant $\hat{\rho}$ for the conditions of fig. 4.42 (see fig. 4.2 for contour code).

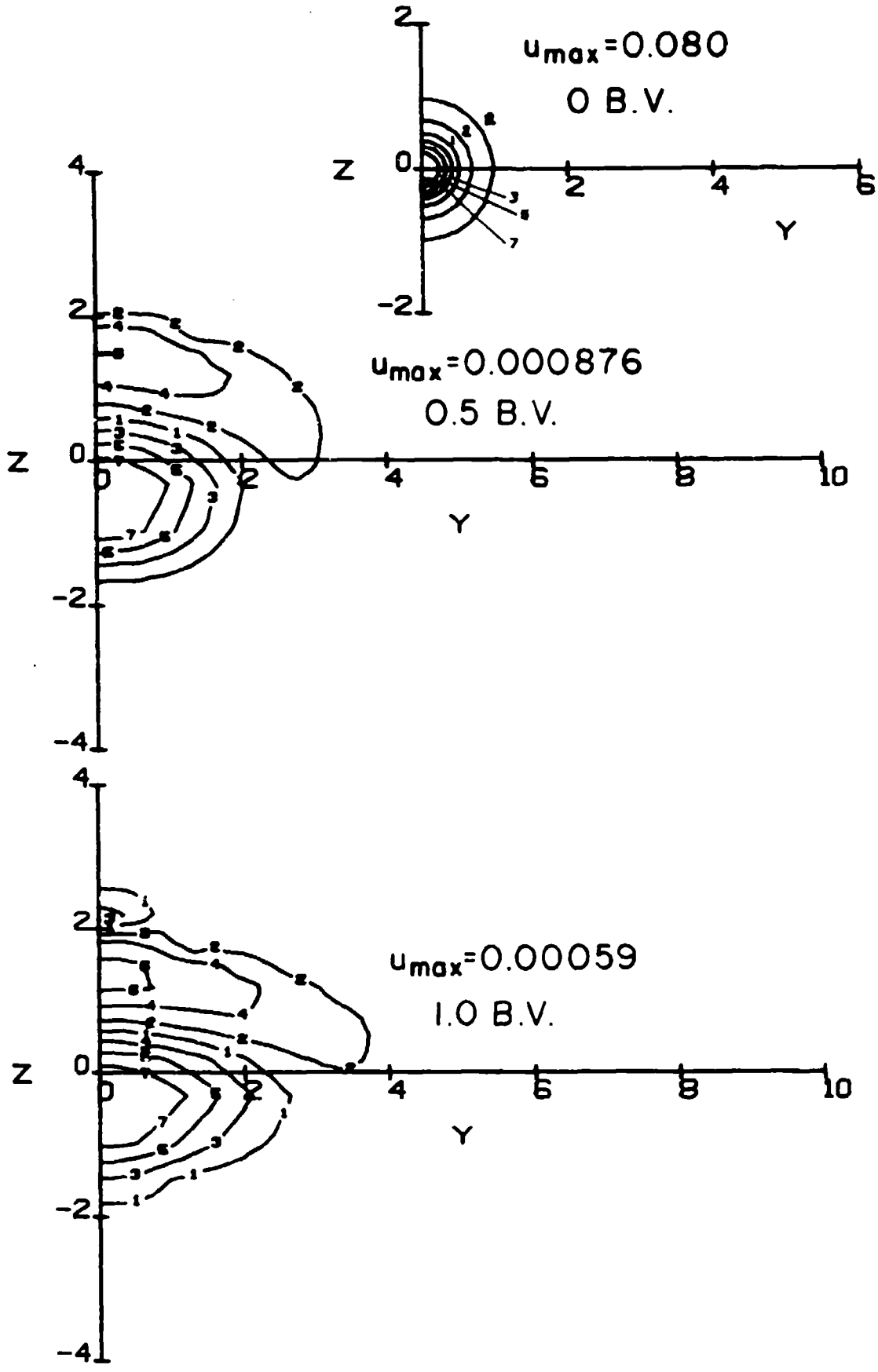

Figure 4.45: Contours of constant u for the conditions of fig. 4.42 (see fig. 4.2 for contour code).

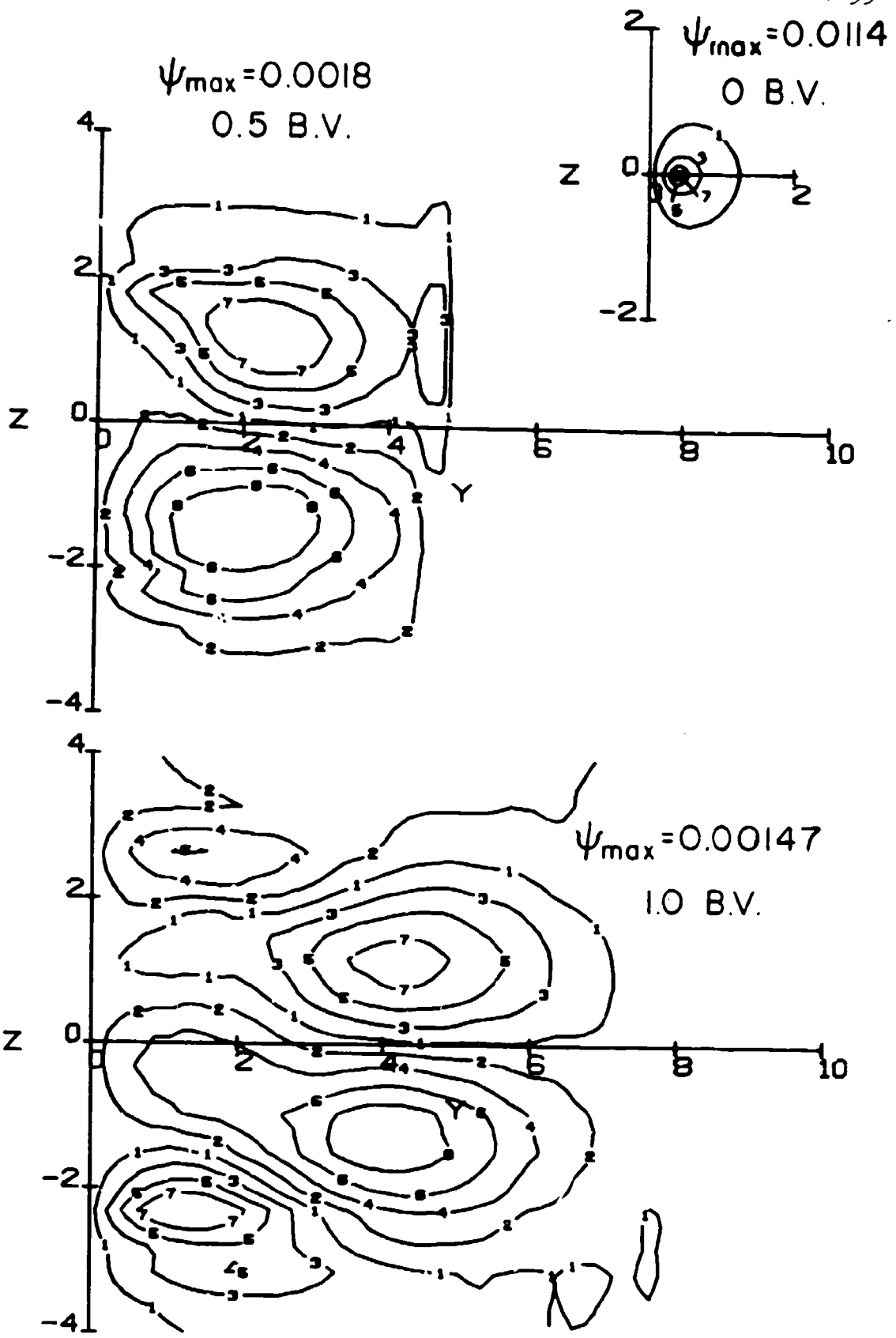

Figure 4.46: Contours of constant ψ for the conditions of fig. 4.42 (see fig. 4.2 for contour code).

in the swirling case, but not with similar decay characteristics, particularly for the three velocity components. The density again shows the collapse effect, with w_{max} dropping rapidly there. The contours exhibit some of the vortex motion; we see that the vortex is eventually dissipated by the turbulence, and lost by the stratified collapse.

We see that lift force makes relatively little difference in the decay characteristics. If we now repeat the calculation but reverse the forcing role (to make the lift positive) we obtain the decay behavior plotted in fig. 4.47 and the contours in figs 4.48 - 4.51. A comparison of fig. 4.42 and 4.47 shows very little difference across the B.V. scale for q_{max}, $\hat{\rho}_{max}$, u_{max}, v_{max} and w_{max}. The contours show a mirror effect, particularly in u, until collapse dominates at 1 B.V.

For a further clarification of the role of lift forces we made a run for the $Fr \to \infty$ limit. In this limit, there can be no gravity induced cross flow, but only the presence of two vortices decaying together. Our calculation shows that indeed the vortices drift downward from their initial positions and travel away from each other. Such behavior is well-predicted by linear theory. In this case, then, the density perturbation is decoupled from the flow dynamics. In fig. 4.52 we show the printer plot of density at a station $x/D = 10.7$ downstream of initialization. This type of plot is the typical output from the WAKE program generating most of the results presented in this report. We can easily discern the spirals present in the vortex field. Note that the negative values of $\hat{\rho}$ have larger absolute values than do the positive values, reflecting the fact that the total wake has moved downward.

Table 4.1 presents a summary of the runs made investigating the sensitivity of the strength of the gravity-induced cross flow on initial conditions. In addition to listing the figures where detailed plots of the time history of major parameters and contours at selected times may be found, we have included two parameters which measure the overall strength of the internal waves generated by the wake. These are the maximum value of the cross-flow stream

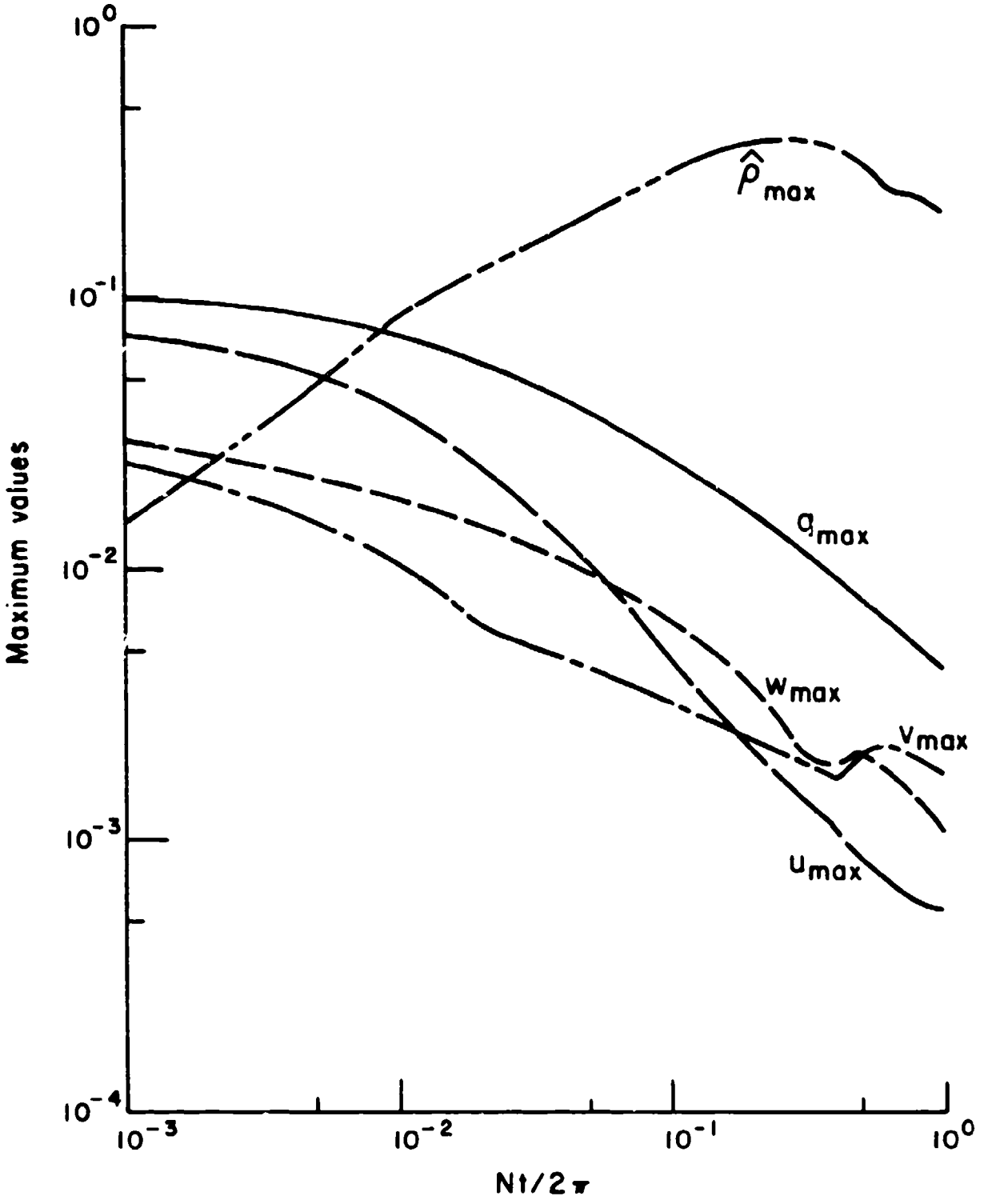

Figure 4.47: Decay of maximum values of q, $\hat{\rho}$, u, v and w for a vortex pair generating positive lift force at $Ri_8 = 0.00925$. Here we begin with $q^2_{max} = 0.0108$, $\hat{\rho} = 0$, $u_{max} \approx 0.08$, and lift/drag ≈ 1.

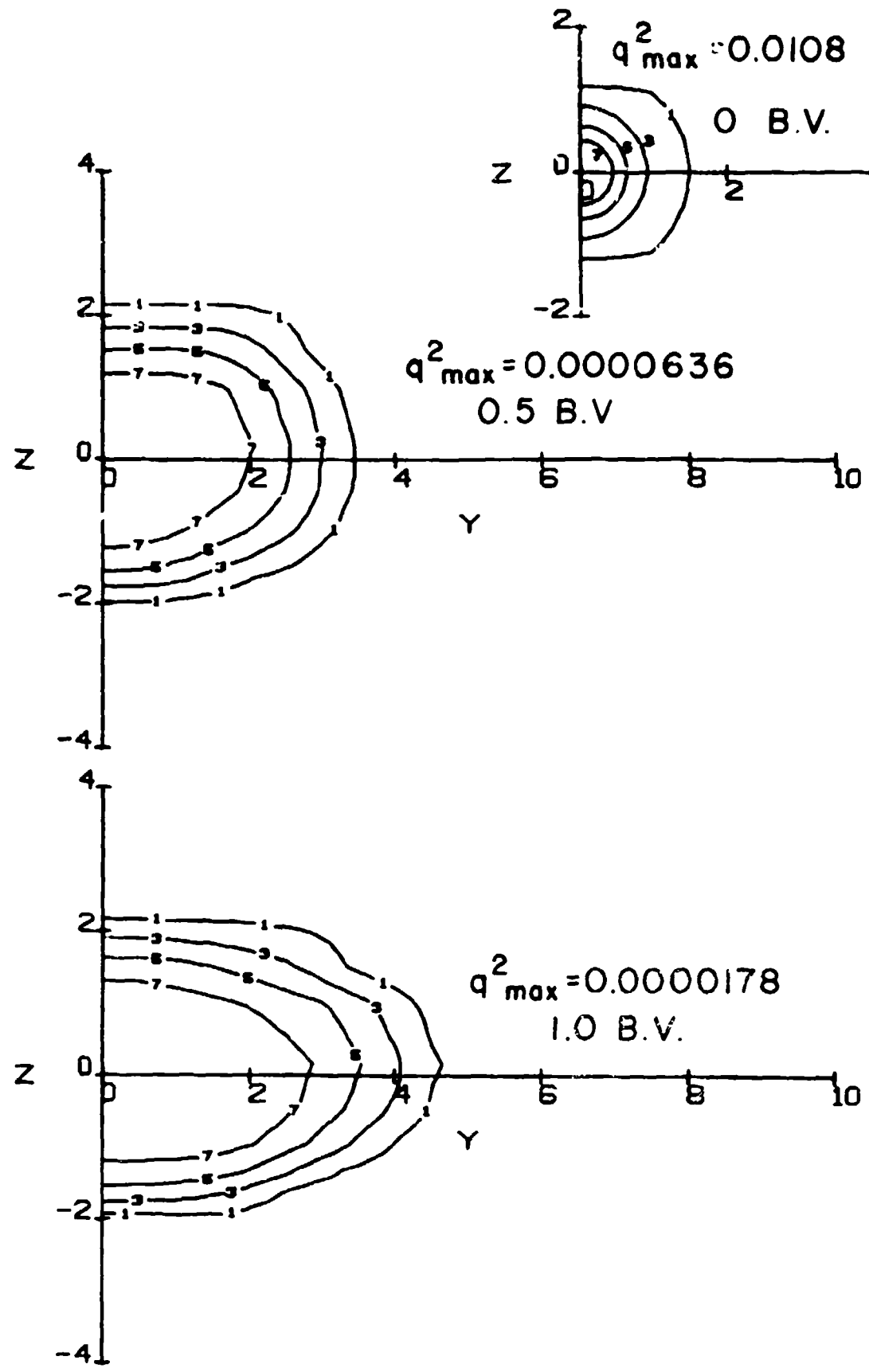

Figure 4.48: Contours of constant q^2 for the conditions of fig. 4.47 (see fig. 4.2 for contour code).

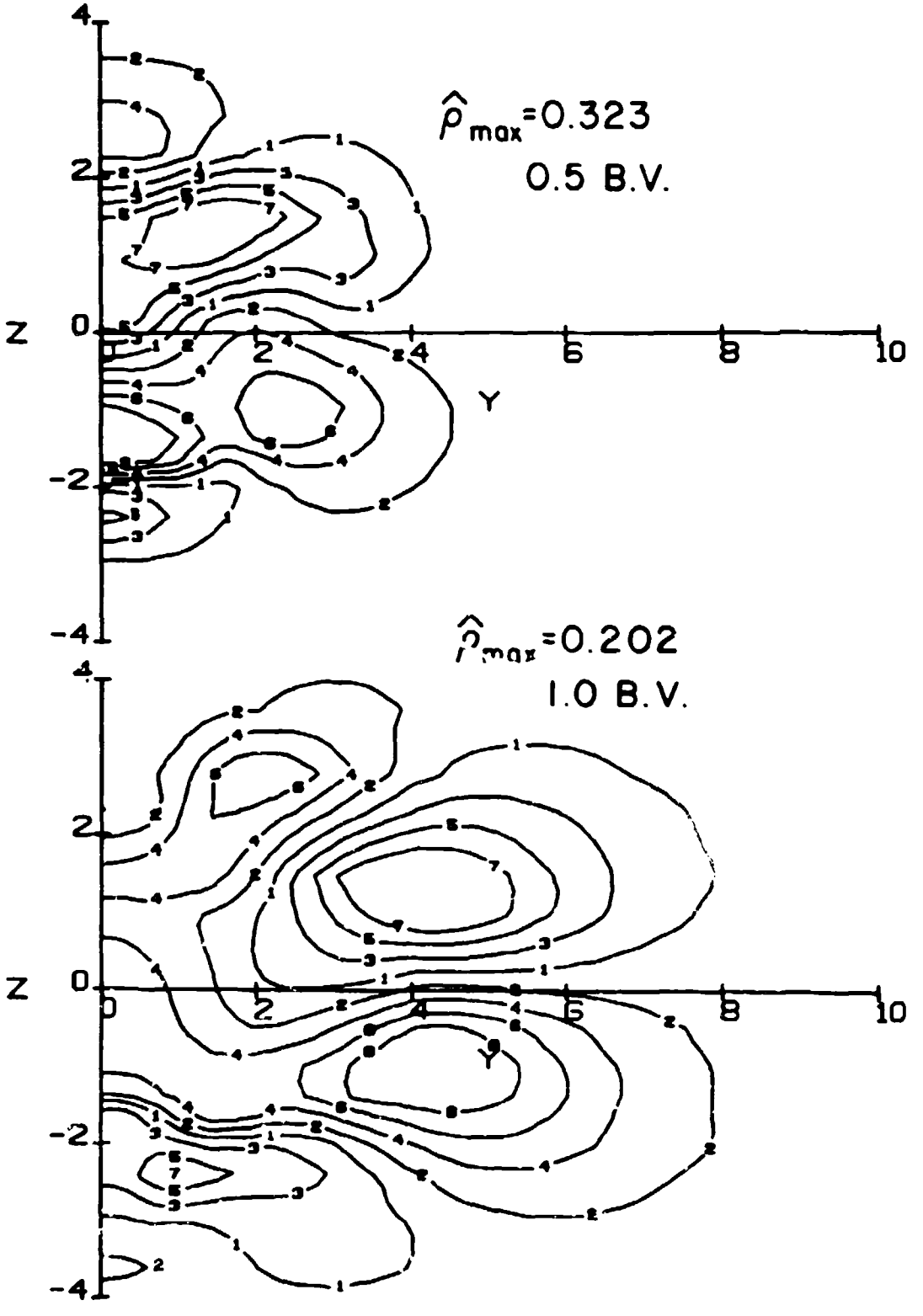

Figure 4.49: Contours of constant $\hat{\rho}$ for the conditions of fig. 4.47 (see fig. 4.2 for contour code).

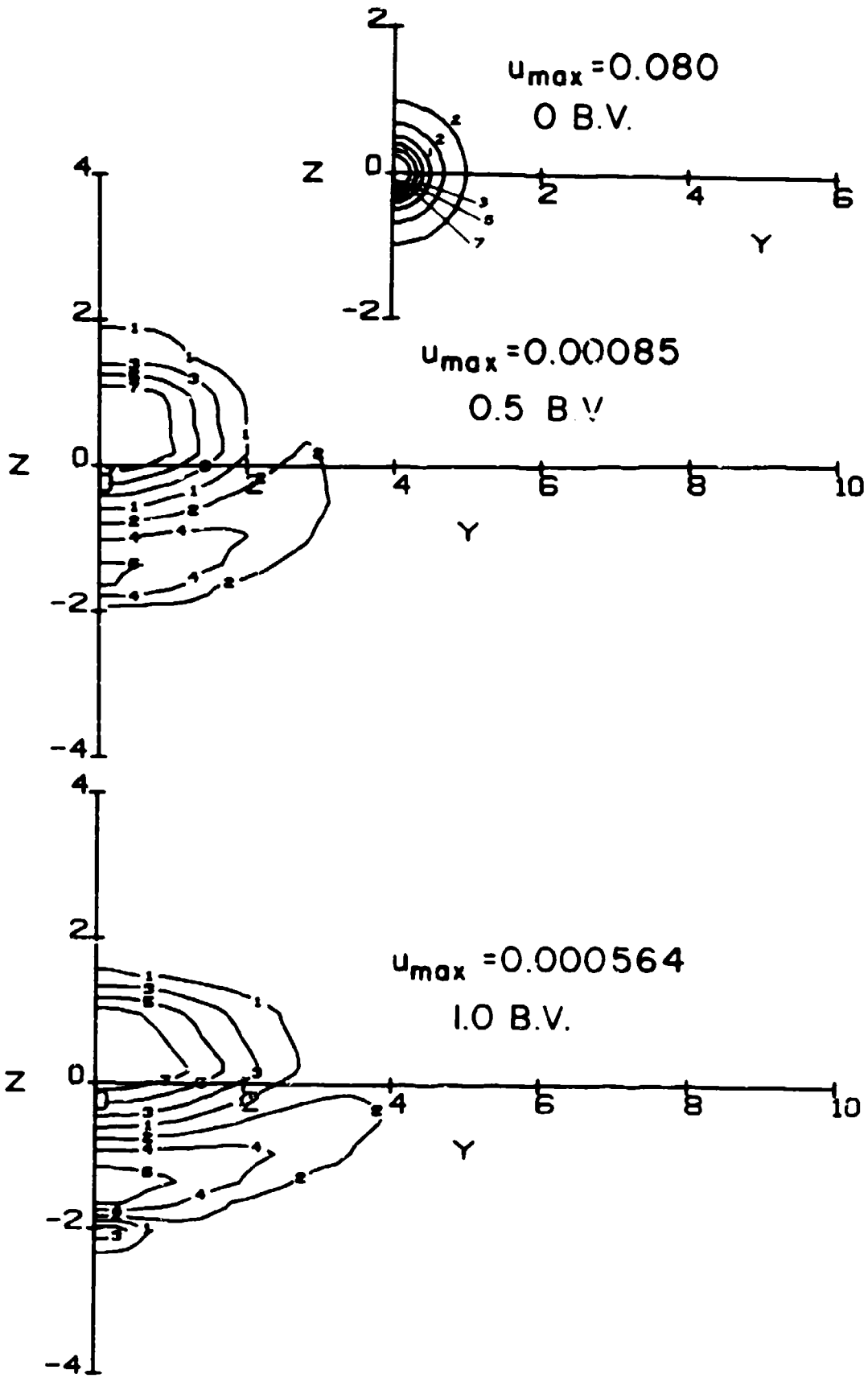

Figure 4.50: Contours of constant u for the conditions of fig. 4.47 (see fig. 4.2 for contour code).

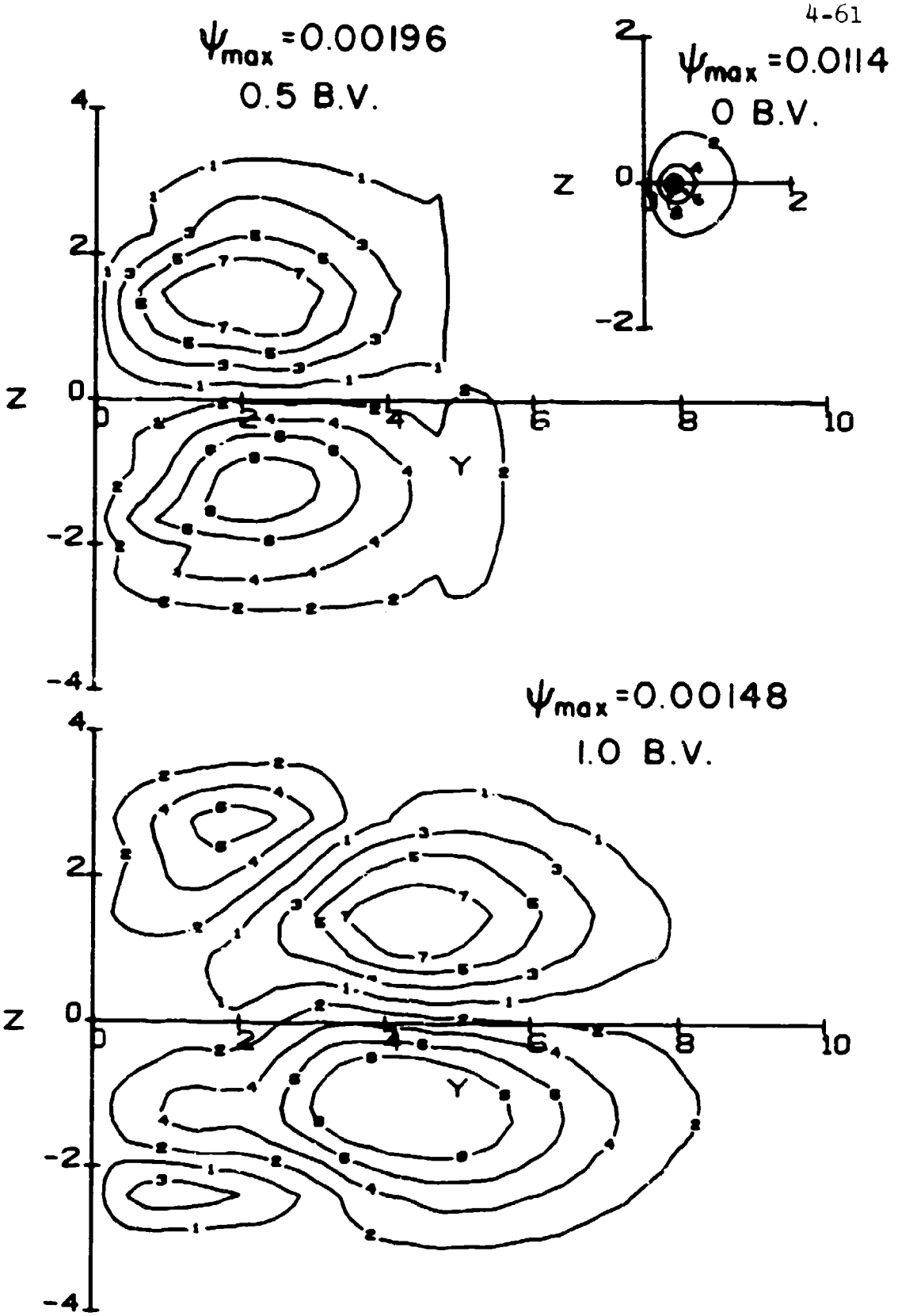

Figure 4.51: Contours of constant ψ for the conditions of fig. 4.47 (see fig. 4.2 for contour code).

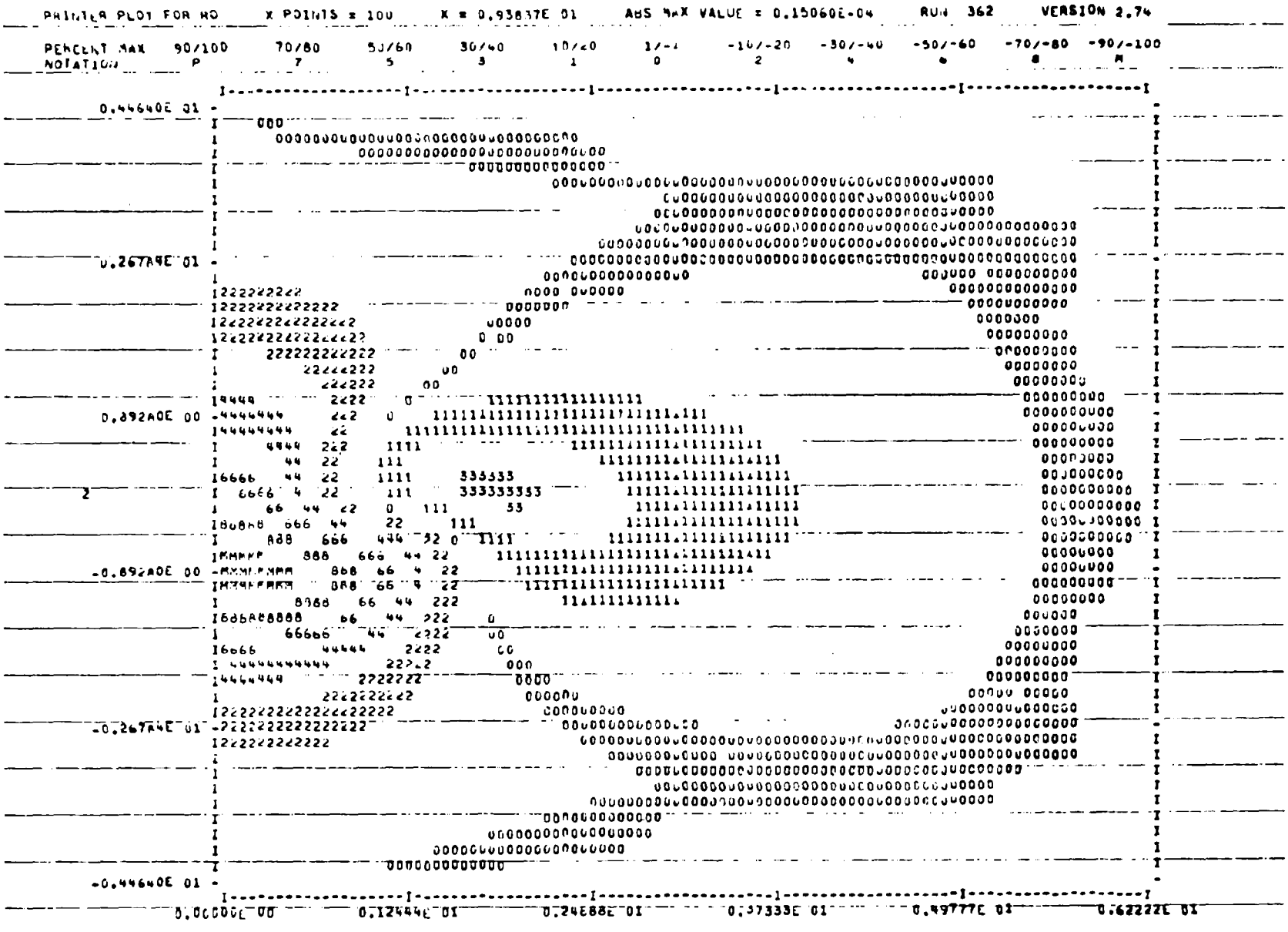

Figure 4.52: A printer plot picture of the perturbation density profile at x/D = 10.7 after initialization for a wake with a vortex pair at $Fr \to \infty$. We begin with $q^2 = \rho = u = 0$, and $v_{max} = w_{max} = 1.0$. Here $\hat{\rho}_{max} = 1.5 \cdot 10^{-5}$ and the notation is as given on the curve for the various level of $\hat{\rho}$ value.

TABLE 4.1

Figure Numbers	Fr	Ri_o	$\hat{r}_1$	Initial Momentum	$\frac{v_{max}}{q_o r_1}$	Energy Radiated at 1 B.V. / Initial Energy	Curve Identification (fig. 4.53)
4.1 - 4.4	20600	2.18×10^{-7}	1.	Momentumless	0.000858	0.016	1
4.5 - 4.8	2060	2.18×10^{-5}	1.	Momentumless	0.00245	0.083	2
4.9 - 4.13	100	0.00925	0	Momentumless	0.0137	0.034	3
4.14- 4.15	10.3	0.872	1.	Momentumless	0.175	0.382	4
4.17- 4.18	10.3	0.872	0	Momentumless	0.020	0.191	5
4.19- 4.20	10.3	0.872	-0.5	Momentumless	0.0365	0.430	6
4.26- 4.30	100	0.00925	0	Propeller-induced swirl	0.039*	0.131	7
4.31- 4.35	10	0.925	0	Propeller-induced swirl	0.118*	0.228	8
4.37- 4.41	10.2	0.855	1.	M = -0.096	0.170	0.208	9
4.42- 4.46	100	0.00925	0	negative lift	0.020	0.065	10
4.47- 4.51	100	0.00925	0	positive lift	0.031	0.068	11
A.1 - A.6	10.2	0.855	-0.5	M = -0.199	0.182	0.250	

M is normalized momentum = $\int_o^\infty \frac{u}{U}\,(u/U - 1)\,\frac{2rdr}{(D/2)^2}$ from ref. 14.

* local maximum above 0.5 B.V.

function and the integrated value of the energy radiated away from the wake by the internal waves. The first of these is computed directly by the program from the velocity field at any time. However the radiated energy cannot be computed directly because of the existence of the absorbing liner. Rather, it is computed indirectly from an energy balance by subtracting the energy remaining and the energy dissipated from the initial energy. This admittedly is not very accurate when the energy dissipated exceeds 95% of the initial energy. Theoretically we can expect the ratio of the energy radiated to the initial energy to decrease as $Ri_o^{-1/2}$ as $Ri_o \to 0$, while $v_{max}/q_o r_i$ should decrease like $Ri_o^{-1/4}$.

As a further summary, the curves of the decay of the turbulence intensity as a function of x/L are repeated in fig. 4.53. The curves are labeled as noted in Table 4.1. The momentumless wakes for $Ri_o \to \infty$ have their turbulence intensity decay approximately as $(x/D)^{-3/4}$. As Ri_o is increased, the rate of decay increases when $x/D \gtrsim Fr$. When the curve ends somewhere between 1 and 2 Brunt-Väisalä periods after initiation, the turbulent intensity is approximately 20% lower than the value of the $Ri_o \to \infty$ curve. Propeller swirl or lift forces cause some slight departure from this basic trend but the largest difference is caused by the introduction of axial momentum. Now the $Ri_o \to \infty$ curve corresponds to the self-similar, finite momentum decay rate of $(x/D)^{-2/3}$ shown dashed in fig. 4.53. Again, as Fr is decreased, the decay rate of q will depart from this when $x/L \approx Fr$. This dashed curve then represents an upper bound on the turbulent intensity. For wakes which start almost momentumless, the decay curve can initially follow the steeper momentumless rate and (as seen in ref. 14) cross over to that appropriate for the momentum wake far downstream. The two momentumless curves shown on the present curve for high Fr had identically zero momentum since they were divided into a Phase I and Phase II calculation as described earlier. The total spread due to any uncertainty in Fr is less than that due to uncertainties in momentum.

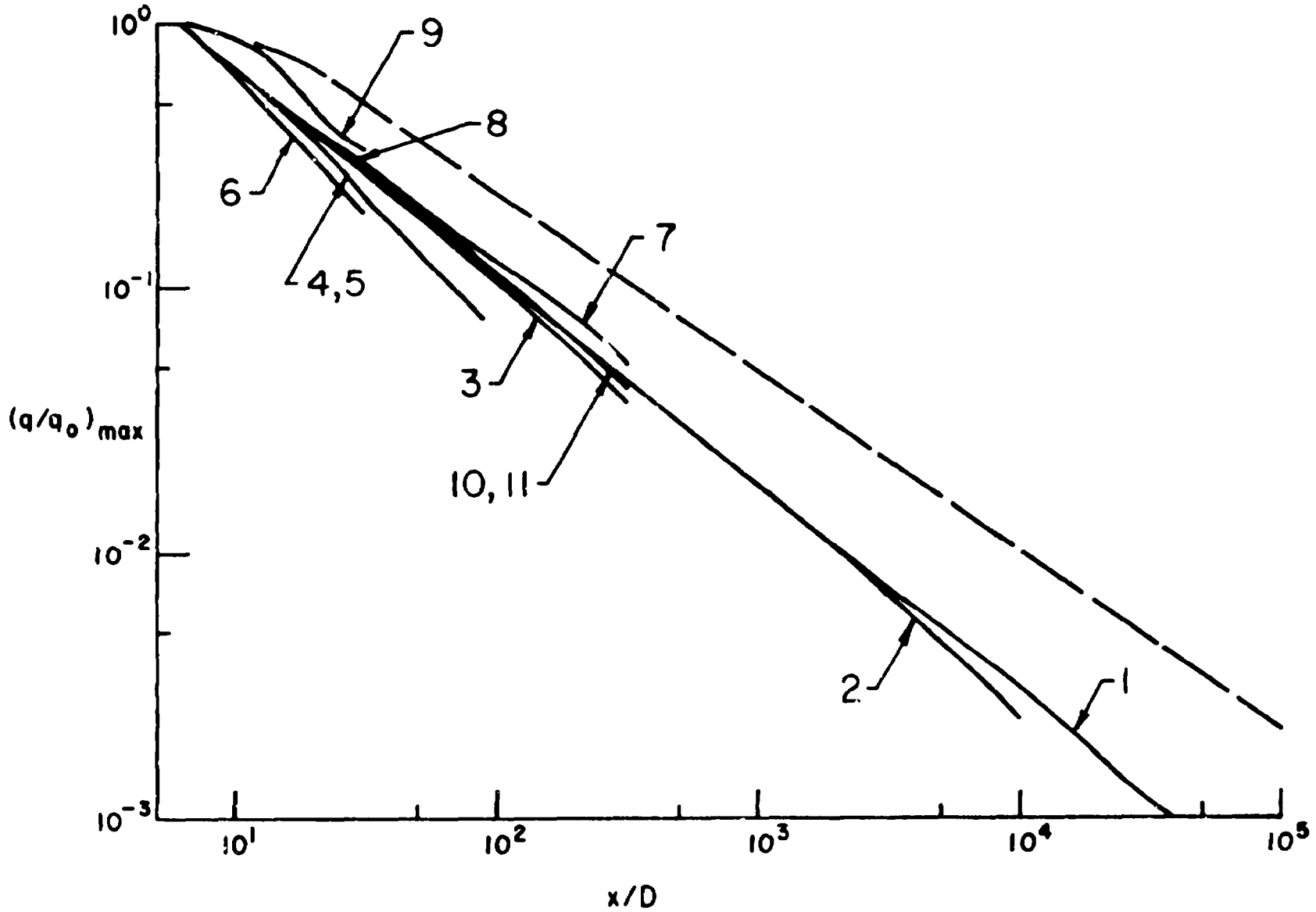

Figure 4.53: A comparison curve of the decay of turbulent energy as a function of x/D distance downstream of generation. The numbers identifying the curves are cross-referenced to runs in this report in Table 4.1. The dashed curve represents our solution of a wake with axial mean momentum, and is a reference curve drawn from the results of ref. 14.

5. CONCLUDING REMARKS

We believe the primary goal of constructing a practical model for wakes including the influences of stratification, axial momentum, vertical momentum, and angular momentum based on second-order closure of the turbulence equations has been accomplished. Although the comparisons of model predictions with some individual experimental observations have been disappointing, agreement with the majority of the experimental data has been quite favorable. There are three basic areas in which the model needs further development: 1) in the numerical implementation so that the full dynamic equation for each Reynolds stress can be solved when it is indicated that the quasi-equilibrium approximation is not valid; 2) in further validation of the macroscale treatment so that a higher confidence can be placed in the model predictions for an untested flow; and 3) in the removal of the approximation that the axial velocity is a small perturbation from the free stream velocity in the fully three-dimensional wake program so that computations are valid closer to the body.

A number of model runs have been made to investigate the sensitivity of the wake development to initial conditions. Some of the more interesting conclusions from this investigation are that: 1) the primary variable affecting the strength of the generated internal waves is the Richardson number; 2) the decay of the turbulent energy as a function of x/b is less sensitive to Froude number than it is to axial momentum; 3) an increase in the initial density perturbation leads to an increase in the gravity induced cross-flow for low Fr but has no influence when $Ri_o < 10^{-2}$; 4) the relatively low value of swirl induced by a propeller-propelled body causes a slightly lower initial decay in wake turbulence although the asymptotic decay rate remains approximately proportional to $x^{-3/4}$; 5) at $Fr = 100$ the swirl induced by a propeller causes an approximate factor of three increase in the wave radiated energy for a wake that is assumed to start with

no initial density perturbation primarily because of the more efficient density mixing of the swirl case; 6) a lift force changes the contour pattern of the primary variables at 1 B.V. without any significant change in the maximum values.

6. REFERENCES

1. Schooley, A. H. and R. W. Stewart: "Experiments with a Self-Propelled Body Submerged in a Fluid with a Vertical Density Gradient," J. Fluid Mechanics, 15, 1963, pp. 83-96.

2. Schooley, A. H.: "Wake Collapse in a Stratified Fluid," Science, 157, 1967, pp. 421-423.

3. Wu, J.: "Mixed Region with Internal Wave Generation in a Density-Stratified Medium," J. Fluid Mechanics, 35, 1969, pp. 531-544.

4. Wessel, W. R.: "Numerical Study of the Collapse of a Perturbation in an Infinite Density Stratified Fluid," Phys. Fluids, Supplement II, 1969, pp. 171-176.

5. Hartman, R. J. and H. W. Lewis: "Wake Collapse in a Stratified Fluid: Linear Treatment," J. Fluid Mech., 51, 1972, pp. 613-618.

6. Young, J. A. and C. W. Hirt: "Numerical Calculation of Internal Wave Motions," J. Fluid Mech. 56, 1972, pp. 265-276.

7. Mei, C. C.: "Collapse of a Homogeneous Fluid Mass in a Stratified Fluid," 12th Int. Congr. Appl. Mech., Springer Press, (1969), pp. 321-330.

8. Merritt, G. E.: "Wake Growth and Collapse in a Stratified Flow," AIAA J., 12, 1974, pp. 940-948.

9. Ko, D. R. S.: "A Phenomenological Model for the Momentumless Turbulent Wake in a Stratified Medium," TRW Report 20086-6007-RU-00, April 1973.

10. Dugan, J. P., A. C. Warn-Varnas and S. A. Piacsek: "Numerical Model for Mixed Region Collapse in a Stratified Fluid," NRL Memorandum Report 2597, June 1973.

11. Ko, D. R. S. and R. L. Gran: "A Phenomenological Model for the Momentumless Turbulent Wake in a Stratified Medium, A Progress Report," Flow Research Note No. 41, December 1973.

12. Donaldson, Coleman, DuP.: "Construction of a Dynamic Model of the Production of Atmospheric Turbulence and the Dispersal of Atmospheric Pollutants," American Meteorological Society Workshop in Micrometeorology, (D. A. Haugen, editor) Science Press, (1973), pp. 313-392.

13. Lewellen, W. S. and M. Teske: "Prediction of the Monin-Obukhov Similarity Functions from an Invariant Model of Turbulence," J. Atmospheric Sciences 30, 1973, pp. 1340-1345.

14. Lewellen, W. S., M. Teske, and Coleman duP. Donaldson: "Application of Turbulence Model Equations to Axisymmetric Wakes," AIAA J., 12, No. 5, 1974, pp. 620-626.

15. Lewellen, W. S., M. Teske, and Coleman duP. Donaldson: "Second-Order, Turbulent Modeling Applied to Momentumless Wakes in Stratified Fluids," A.R.A.P. Report No. 206, Nov. 1973.

16. Rotta, J. C.: Turbulente Strömungen, Teubner Press, Stuttgart, 1972.

17. Rodi, W.: "The Prediction of Free Turbulent Boundary Layers by Use of a Two-Equation Model of Turbulence," Dissertation submitted to Mechanical Engineering Department, Imperial College, London, December 1972.

18. Daly, B. J. and F. H. Harlow: "Transport Equations in Turbulence," The Physics of Fluids, 13, pp. 2634-2649, Nov. 1970.

19. Lumley, J. L. and B. Khajeh-Nouri: "Computational Modeling of Turbulent Transport," to appear in Advances in Geophysics.

20. Bradshaw, P.: "The Understanding and Prediction of Turbulent Flow," Aero. J. 76, pp. 403-418, 1972.

21. Mellor, G. L and H. J. Herring: "A Survey of Mean Turbulent Field Closure Models," AIAA J. 11, No. 5, pp. 590-599, 1973.

22. Gad-El-Hak, M, and S. Corrsin: "Measurements of the Nearly Isotropic Turbulence Behind a Uniform Jet Grid," J. Fluid Mechanics, 62, pp. 115-143, 1974.

23. Wygnanski, I. and H. Fiedler: "Some Measurements in the Self-Preserving Jet," J. Fluid Mechanics, 38, pp. 577-612, 1969.

24. Chevray, R.: "The Turbulent Wake of a Body of Revolution," ASME J. of Basic Engineering 90, Series D. pp. 275-284, 1968.

25. Naudascher, E.: "Flow in the Wake of Self-Propelled Bodies and Related Sources of Turbulence," J. Fluid Mechanics 22, pp. 625-656, 1965.

26. Coles, D.: "Measurements in the Boundary Layer on a Smooth Flat Plate in Supersonic Flow, Part I: The Problem of the Turbulent Boundary Layer," JPL Report No. 20-69, 1953.

27. Kato, H. and O. M. Phillips: "On the Penetration of a Turbulent Layer into Stratified Fluid," J. Fluid Mechanics 37, pp. 643-656, 1969.

28. Mellor, G. L. and T. Yamada: "A Hierarchy of Turbulence Closure Models for Planetary Boundary Layers," to be published.

29. Roache, P. J.: Computational Fluid Dynamics, Hermosa Publishers (1972), pp. 130-185, 194-195.

30. Carnahan, B., H. A. Luther, and J. O. Wilkes: Applied Numerical Methods, Wiley and Sons (1969), pp. 452-453, 508.

31. Dorr, F. W.: "The Direct Solution of the Discrete Poisson Equation on a Rectangle," SIAM Review 12, No. 2, pp. 248-263, 1970.

32. Schetz, J. A. and A. K. Jakubowski: "Wind Tunnel Studies of the Turbulent Wake Behind Self-Preserved, Slender Bodies," VPI-Aero-014, June 1974.

33. Sullivan, R. D.: "A Program to Compute the Behavior of a Three-Dimensional Turbulent Vortex," ARL TR 74-0009, 1974.

34. Gran, R. L.: "An Experiment on the Wake of a Slender Propeller-Driven Body," TRW Report 20086-6006-RU-00, June 1973.

35. FRI body wake data, private communication.

36. Lin, J. T. and Y. H. Pao: "Turbulent Wake of a Self-Propelled Slender Body in Stratified and Non-Stratified Fluids: Analysis and Flow Visualizations," Flow Research Report No. 11, July 1973.

APPENDIX

MODEL PREDICTIONS FOR STRATIFIED WAKE DEVELOPMENT GENERATED FROM FRI'S INITIAL CONDITIONS

The initial profiles from Flow Research, Inc.'s stratified towing tank experiment (ref. 35) were given at $x/D = 6$ for several stations in y and z for the principal variables q^2, $\hat{\rho}$ and u. With these curves, we constructed an extrapolated curve fit which passed reasonably well through the given profile data. The initial contours in the first-quadrant solution plane are shown in fig. A.1. An unusual feature of these initial conditions is the character of the initial density. In our typical turbulent wake runs, $\hat{\rho}$ is a positive departure from the background for $z > 0$. This is the behavior expected in a wake more uniformly mixed than the surrounding stratified fluid. Instead, it seems that at $x/D = 6$, the wake is dominated by the body generated internal wave to give a wake with a stronger density gradient inside than outside. In this light, the FRI data presents a challenging problem to the wake program - to compute for a set of initial conditions its inventors did not envision.

Contours of q^2, $\hat{\rho}$, u, and streamline ψ are presented in figs. A.2 - A.5 at 0.5, 1.0 and 1.5 Brunt-Vaisala (B.V.) periods after run initialization. Figure A.6 gives the time history of the maximum values. We observe from here the typical type of behavior: the decay of q^2 downstream; the spread of u with time; and the buildup of the cross-plane velocities v and w to their maximum value near 0.5 B.V. However, because of the initial sign of the density perturbation, the development of the vertical height of the wake is quite different. This comparison is shown in fig. A.21.

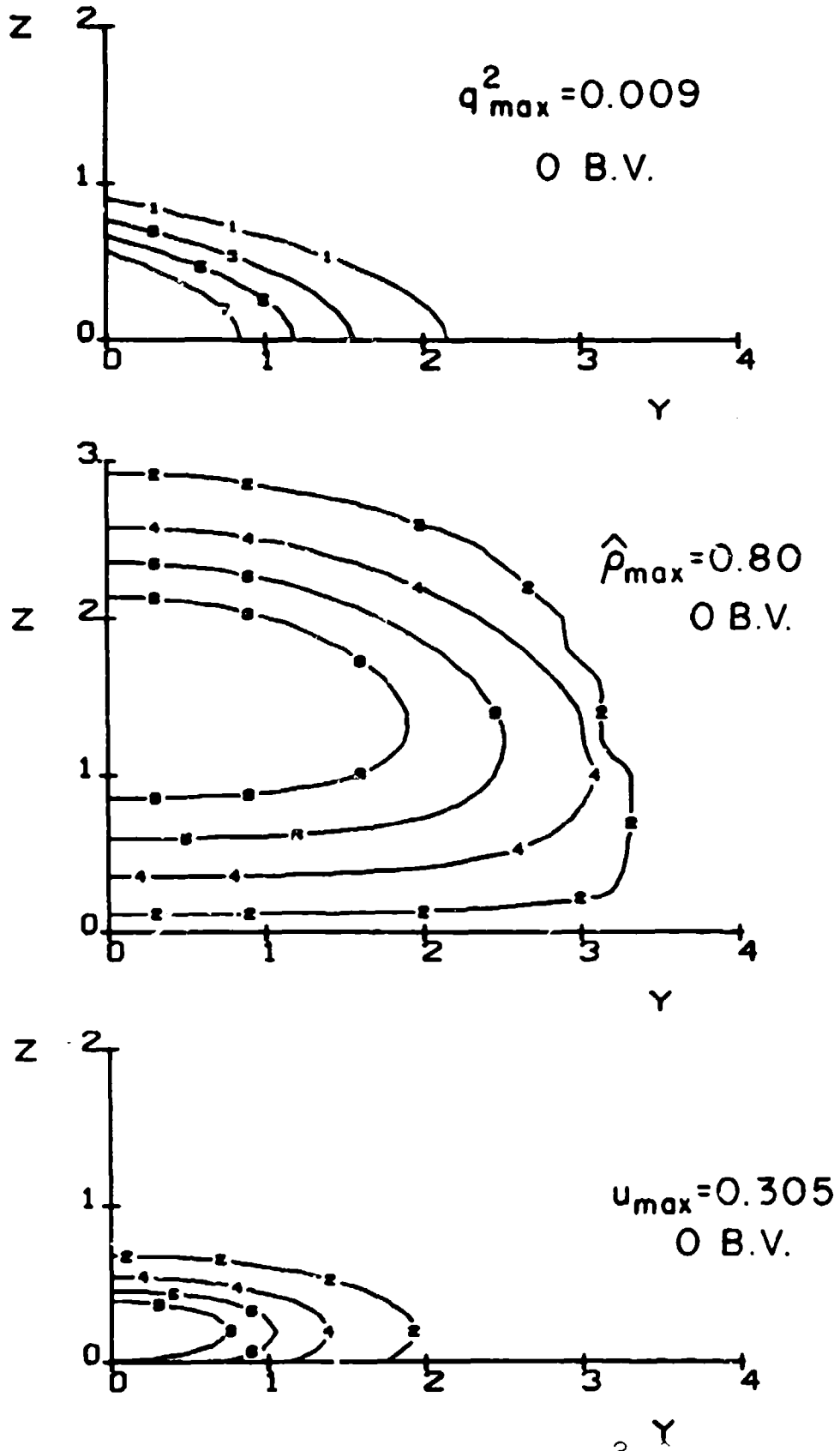

Figure A.1: The initial contour profiles for q^2, ρ and u for the Flow Research Inc. data (ref. 35) with Ri_o = 0.855 and q^2_{max} = 0.009, $\hat{\rho}_{max}$ -0.80 and u_{max} = .305 (see fig. 4.2 for contour code).

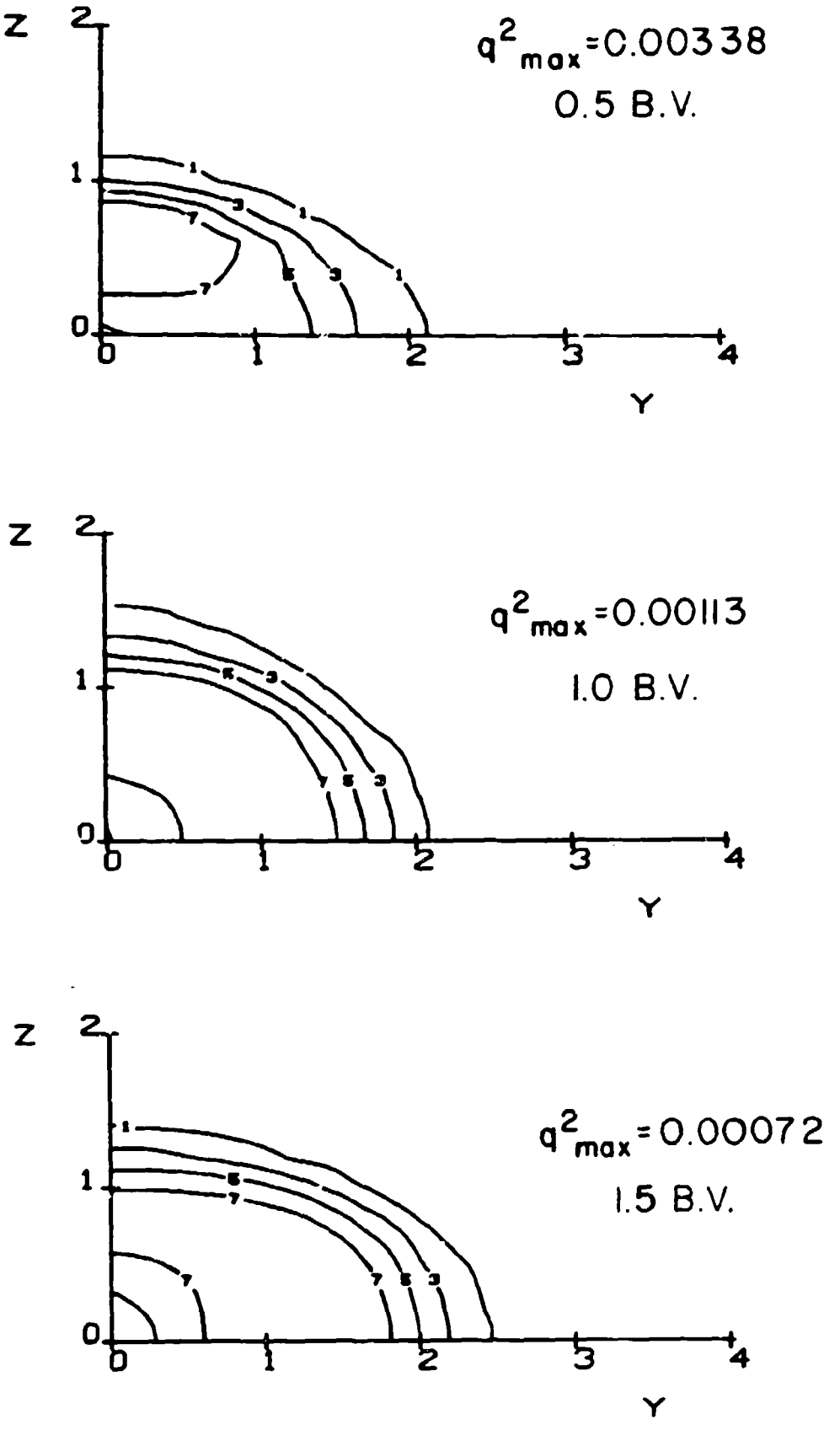

Figure A.2: Contours of constant q^2 for the conditions of fig A.1 (see fig. 4.2 for contour code).

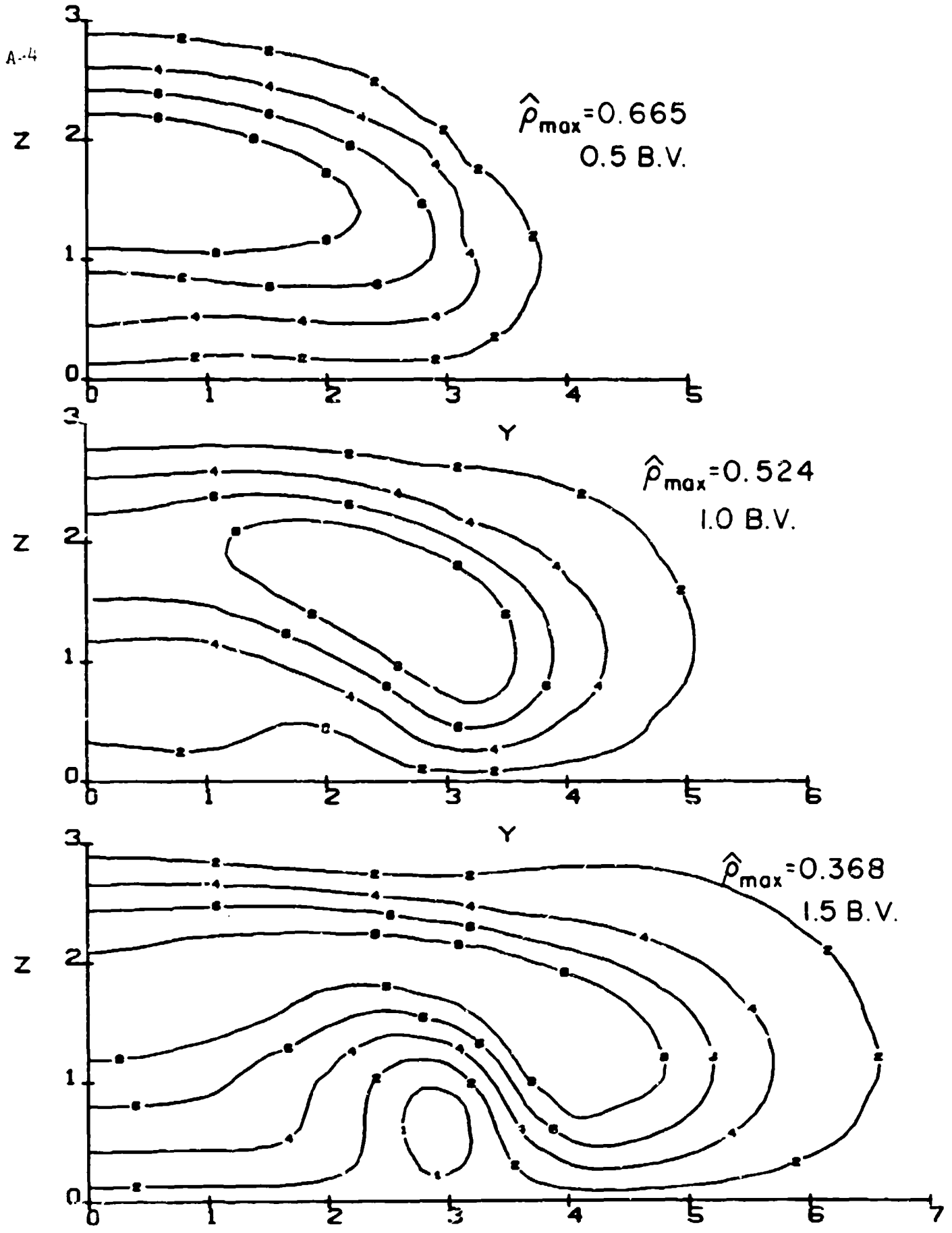

Figure A.3: Contours of constant $\hat{\rho}$ for the conditions of fig. A.1 (see fig. 4.2 for contour code).

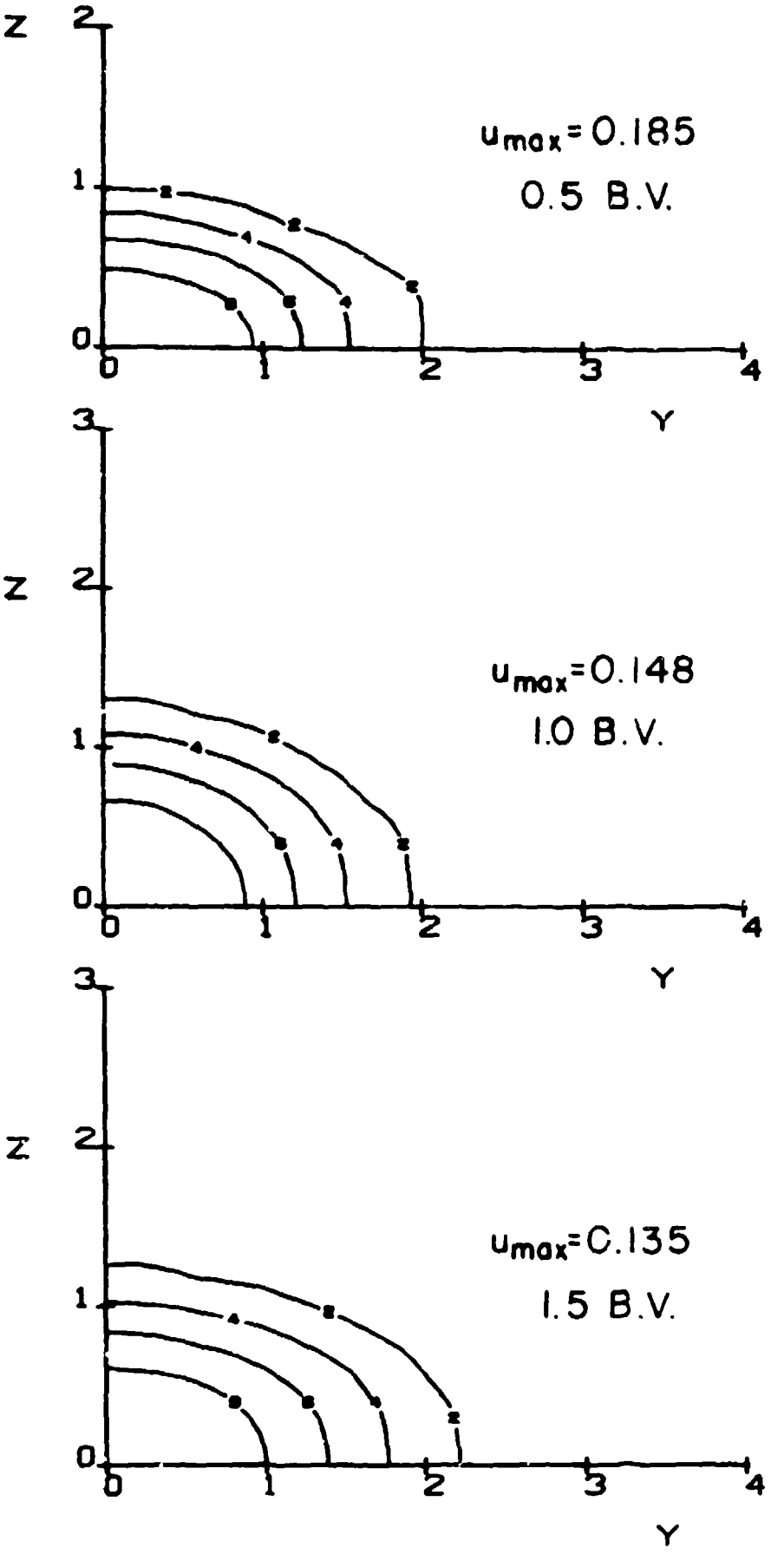

Figure A.4: Contours of constant u for the conditions of fig. A.1 (see fig. 4.2 for contour code).

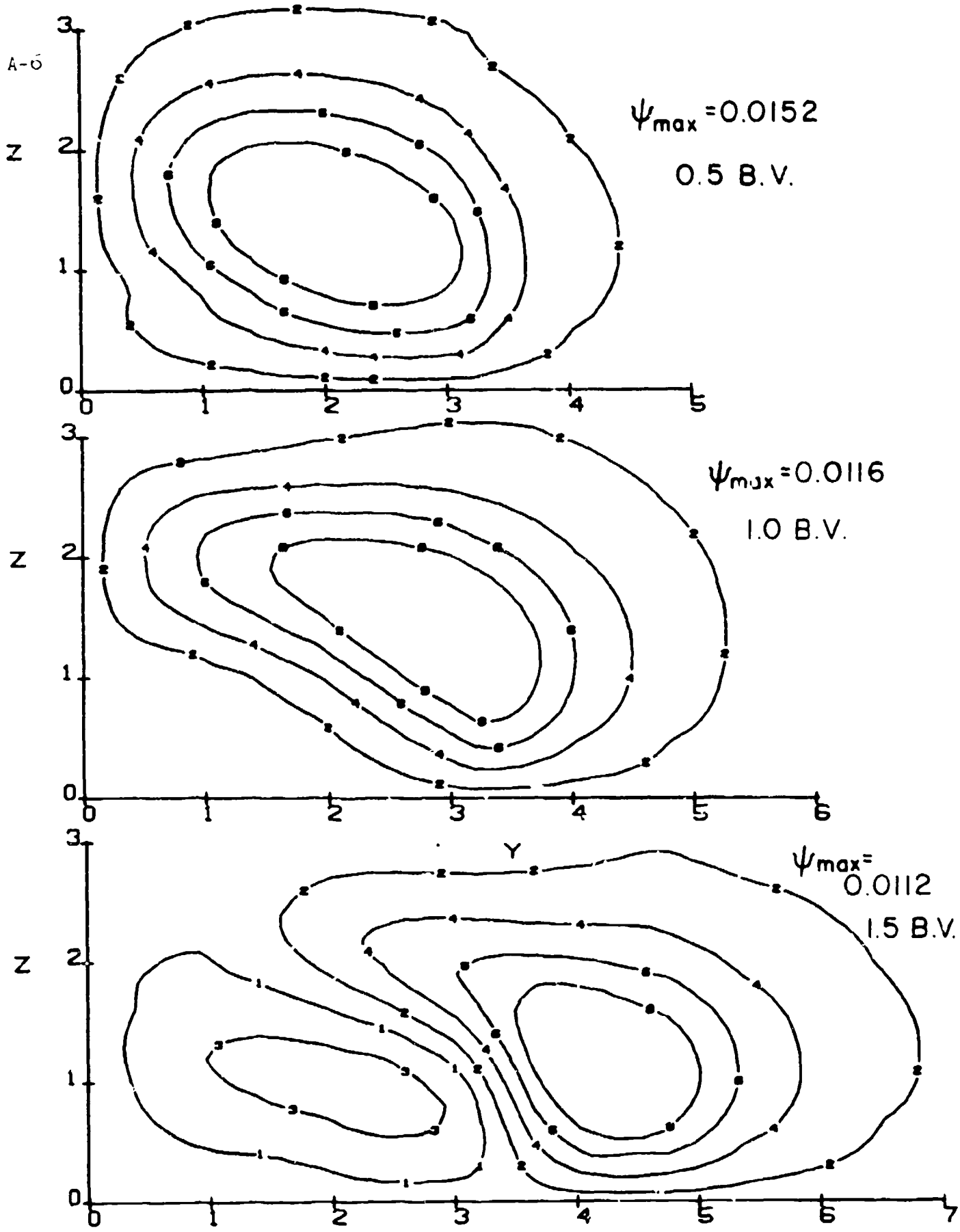

Figure A.5: Contours of constant ψ for the conditions of fig. A.1 (see fig. 4.2 for contour code).

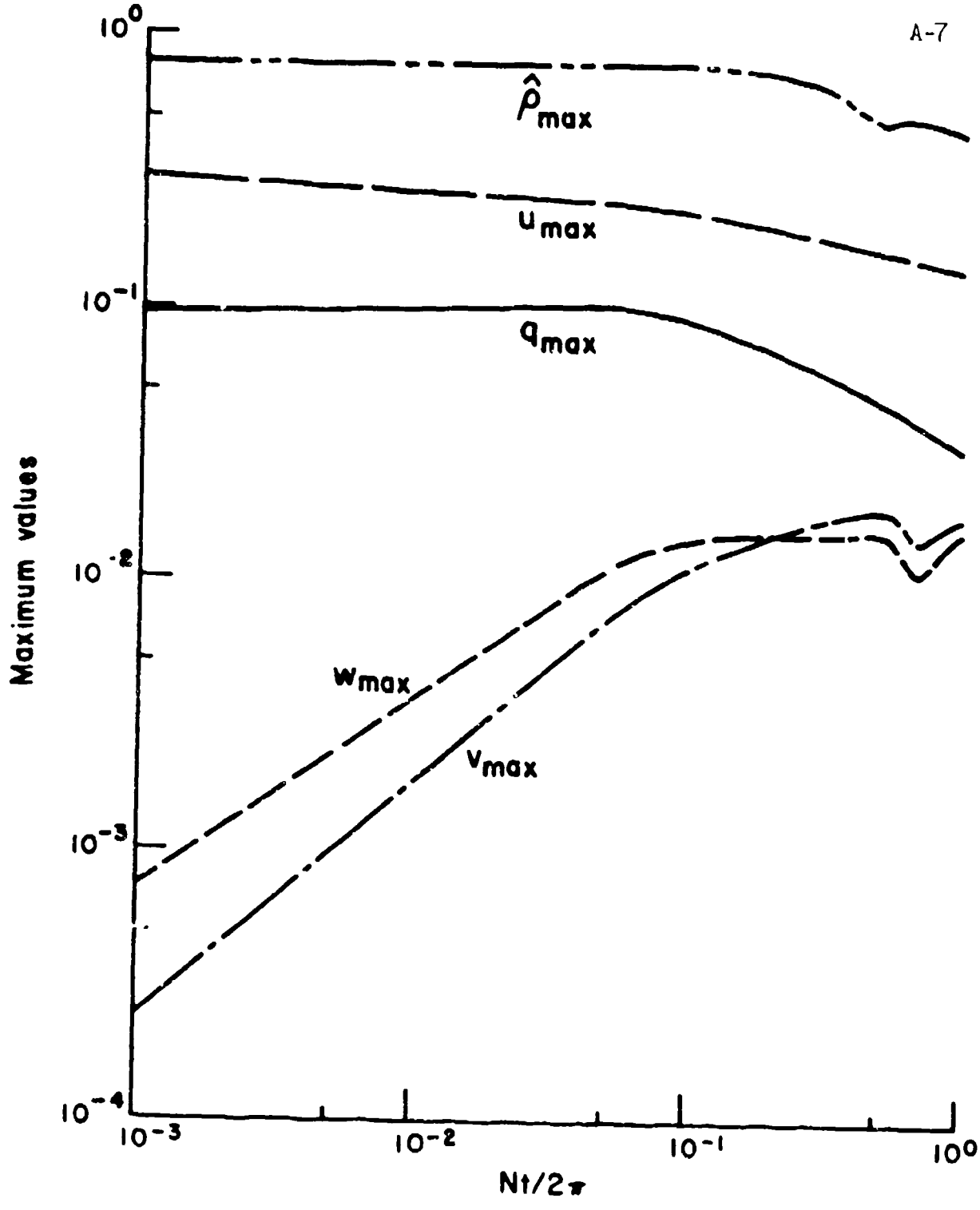

Figure A.6: Decay of maximum values of q , $\hat{\rho}$, u , v and w for the conditions of fig. A.1.

SECURITY CLASSIFICATION OF THIS PAGE (When Data Entered)

REPORT DOCUMENTATION PAGE

READ INSTRUCTIONS BEFORE COMPLETING FORM

1. REPORT NUMBER: A.R.A.P. Report No. 226	2. GOVT ACCESSION NO.
3. RECIPIENT'S CATALOG NUMBER	
4. TITLE (and Subtitle): Turbulent Wakes in a Stratified Fluid Part I: Model Development, Verification, and Sensitivity to Initial Conditions	5. TYPE OF REPORT & PERIOD COVERED: Final Report
	6. PERFORMING ORG. REPORT NUMBER
7. AUTHOR(s): W. Stephen Lewellen, Milton Teske, Coleman duP. Donaldson	8. CONTRACT OR GRANT NUMBER(s): N00014-72-C-0413
9. PERFORMING ORGANIZATION NAME AND ADDRESS: Aeronautical Research Associates of Princeton, Inc., 50 Washington Rd., Princeton, N. J. 08540	10. PROGRAM ELEMENT, PROJECT, TASK AREA & WORK UNIT NUMBERS: DARPA Order No. 1910
11. CONTROLLING OFFICE NAME AND ADDRESS: Office of Naval Research, Department of the Navy, Arlington, Va.	12. REPORT DATE: August 1974
	13. NUMBER OF PAGES: 132
14. MONITORING AGENCY NAME & ADDRESS(if different from Controlling Office)	15. SECURITY CLASS. (of this report)
	15a. DECLASSIFICATION/DOWNGRADING SCHEDULE

16. DISTRIBUTION STATEMENT (of this Report)

[illegible] STATEMENT A

Approved for public release; Distribution Unlimited

17. DISTRIBUTION STATEMENT (of the abstract entered in Block 20, if different from Report)

18. SUPPLEMENTARY NOTES

19. KEY WORDS (Continue on reverse side if necessary and identify by block number)

Submarine wakes
Turbulence modeling
Stratified flow
Swirling wakes
Numerical fluid dynamics

20. ABSTRACT (Continue on reverse side if necessary and identify by block number)

A computational model has been developed for the turbulent wake of a body moving through a stably stratified fluid. Details of the wake growth, collapse and generation of internal waves were examined by the application of a second-order closure approach to turbulent flow developed at A.R.A.P. over the past few years. Predictions of the model have been verified by comparison with a wide variety of wake flows including wakes with no momentum, wakes with axial momentum, wakes with angular momentum, and for wakes in

DD FORM 1 JAN 73 1473 EDITION OF 1 NOV 65 IS OBSOLETE

SECURITY CLASSIFICATION OF THIS PAGE (When Data Entered)

both stratified and unstratified fluids. A sensitivity investigation reveals that the primary variable affecting the strength of the generated internal waves is the initial Richardson number, with the first local maximum of the vertical height of the wake scaling inversely with the 1/8th power of the initial Richardson number.